Use of Instabilities in Electrostatic Micro-Electro-Mechanical Systems for Actuation and Sensing

by

Mahmoud Khater

A thesis
presented to the University of Waterloo
in fulfillment of the
thesis requirement for the degree of
Doctor of Philosophy
in
Systems Design Engineering

Waterloo, Ontario, Canada, 2011

Thesis Declaration

I hereby declare that I am the sole author of this thesis. This is a true copy of the thesis, including any required final revisions, as accepted by my examiners.
I understand that my thesis may be made electronically available to the public.

ABSTRACT

This thesis develops methods to exploit static and dynamic instabilities in electrostatic MEMS to develop new MEMS devices, namely dynamically actuated micro switches and binary micro gas sensors. Models are developed for the devices under consideration where the structures are treated as elastic continua. The electrostatic force is treated as a nonlinear function of displacement derived under the assumption of parallel-plate theorem. The Galerkin method is used to discretize the distributed-parameter models, thus reducing the governing partial differential equations into sets of nonlinear ordinary-differential equations. The shooting method is used to numerically solve those equations to obtain the frequency-response curves of those devices and the Floquet theory is used to investigate their stability.

To develop the dynamically actuated micro switches, we investigate the response of microswitches to a combination of DC and AC excitations. We find that dynamically actuated micro switches can realize significant energy savings, up to 60%, over comparable switches traditionally actuated by pure DC voltage. We devise two dynamic actuation methods: a fixed-frequency method and a shifted-frequency method. While the fixed-frequency method is simpler to implement, the shifted-frequency method can minimize the switching time to the same order as that realized using traditional DC actuation. We also introduce a parameter identification technique to estimate the switch geometrical and material properties, namely thickness, modulus of elasticity, and residual stress.

We also develop a new detection technique for micro mass sensors that does not require any readout electronics. We use this method to develop static and dynamic binary mass sensors. The sensors are composed of a cantilever beam connected to a rigid plate at its free end and electrostatically coupled to an electrode underneath it. Two versions of micro mass sensors are presented: static binary mass sensor and dynamic binary mass sensor.

Sensitivity analysis shows that the sensitivity of our static mass sensor represents an upper bound for the sensitivity of comparable statically detected inertial mass sensors. It also shows that the dynamic binary mass sensors is three orders of magnitude more sensitive than the static binary mass sensor. We equip our mass sensor with a polymer detector, doped Polyaniline, to realize a formaldehyde vapor sensor and demonstrate its functionality experimentally. We find that while the static binary gas sensor is simpler to realize than the dynamic binary gas sensor, it is more susceptible to external disturbances.

Acknowledgements

I would like to express my deep appreciation to my supervisor Prof. Eihab Abdel-Rahman for his guidance throughout the work on this thesis. I'm very grateful for his thorough review of the thesis and the publications out of this work. I'm also indebted to Prof. Ali Nayfeh for his ideas and comments which had a great influence on this work and to Prof. Samir Emam for his continuous support and encouragement.

I would like to thank my advisory committee, Prof. Glenn Heppler, Prof. Arsen Hajian, Prof. Karim Karim, and Prof. Luc Frechette for their insight, suggestions, and time in evaluating my work.

I'm extremely grateful to all the colleagues who helped me through my work. Special thanks go to Sangtak Park, So-Ra Chung, Mohammad Basha, Ahmad Kamal, Yanhui Bai, Andrew Logan, Krishna Vummidi, Sepehr Forouzanfar, Emmanuel Delande, Kate Stewart, Shruti Nambiar, Manu Venkataram, Neil Sarkar, Siamak Fouladi, and Tareq Naqvi.

I'm very grateful to my friends: Hazem Shehata, Ayman Sadoun, Noman Hai, Shakil Sharif, Ahmad Amin, Reda Gad, Mohamad Ibrahim, Mahmoud Hashem, Abd-Allah Qabil, Mohammad Attaher, Ahmad Ibrahim, and Alaa Abdul-Rahman for their support and encouragement.

I'm extremely indebted to my mother for her great sacrifices for me and our small family. My words can never give her the credit she deserves. I'm very grateful to my wife for her patience and continuous help. I'm also grateful to my brother and my caring sisters for their encouragement and continuous support. I'm also very thankful to my relatives and to the people whom I didn't mention their names but they were always there. Thank you very much.

Dedication

To my beloved mother

To my wife

To my brother, Mohammad

To my sisters

and

To my son, Omar

Contents

List of Figures

List of Tables

List of Symbols

The following notations are used throughout the text; other notations are used at their relevant positions:

Γ	An integral operator defined by Eq. (2.39)
$\pounds$	The Lagrangian defined by Eq. (2.28)
$\phi_i(x)$	The micro beam mode shapes
ω_n	Nondimensional micro beam natural frequency
ρ	Micro beam material density
σ	Axial residual stress in the micro beam
A	Micro beam cross-sectional area
b	Micro beam width
c_s	Nondimensional squeeze film damping coefficient
c_v	Nondimensional viscous damping coefficient
E	Micro beam modulus of elasticity
f	Nondimensional frequency
F_e	Electrostatic force applied to the beam
h	Micro beam thickness
I	Micro beam moment of inertia
J	Micro beam polar moment of inertia
L	Micro beam length
N	Axial force in the beam due to residual stress
m	Micro beam mass per unit beam length
S	Sensitivity of the sensor to added mass
T	Kinetic energy due to beam mass
V_a	Potential energy due to axial force N
V_b	Potential energy due to bending moment
V_E	Potential energy due to electrostatic force
V	Total potential energy
V_{AC}	AC voltage component of forcing
V_{DC}	DC voltage component of forcing
V_{DP}	Pull-in voltage under dynamic DC-AC actuation
V_{SP}	Pull-in voltage under static DC actuation
$w_s(x)$	Transverse static deflection of the beam due to DC forcing
$u(x,t)$	Transverse dynamic deflection of the beam due to AC forcing beyond static deflection $w_s(x)$
$w(x,t)$	Total transverse deflection of the beam due to DC-AC forcing
$q_i(t)$	Generalized coordinates describing the beam motion as a function of time

Chapter 1

Introduction

1.1 Electrostatic MEMS

1.1.1 MEMS

The acronym MEMS stands for Micro-Electro-Mechanical Systems. In these systems, mechanical elements, sensors, actuators, and electronics are integrated on a common silicon substrate through micro fabrication technology. MEMS technology has been adopted from the integrated circuit industry.

MEMS and micro system products have dominated many fields as the technology for micro fabrication continues to be developed. In the automotive industry, applications of MEMS include accelerometers for air-bag systems in automobiles. Other applications in car industry include position and pressure sensors for suspension systems; fuel pump pressure and fuel injection control; sensors used to control engine coolant temperature, engine oil pressure and level, tire pressure, brake oil pressure, and fuel pressure; rider comfort sensors for air quality, airflow, temperature and humidity control [1].

Applications in the aerospace industry include cockpit instrumentation; pressure sensors for oil, fuel, transmission, and hydraulic systems; airspeed measurement devices; safety devices; sensors for fuel efficiency; micro gyroscopes for navigation and stability control [1].

Applications in industrial products include sensors for hydraulic systems, refrigeration systems, heating and air conditioning systems, and water level control. In telecommunications, applications include optical switching, RF switches, and tunable filters [1, 2].

One of the promising areas for MEMS application is the biological and biomedical field. Applications in health care include lung capacity meters, respirators, kidney analysis equipment, and catheter tip pressure sensors. Micro pumps for insulin injection have been employed for years. Other application include micro systems for DNA identification and biochips for detection of hazardous chemical and biological agents [1, 2].

1.1.2 Electrostatic actuation

Different actuation methods are employed in MEMS. These methods include thermal, magnetic, piezoelectric, and electrostatic actuation. Among them, electrostatic actuation offers high energy density, high mechanical flexibility, and well-controlled force over several microns of displacement [3]. Electrostatic actuation requires higher actuation voltages compared to other actuation techniques, however, it usually requires very small current. This has an effect of reducing the overall power requirements of electrostatically actuated micro systems.

The force induced by electrostatic actuation is small compared to that induced under piezoelectric and thermal actuation. However, electrostatically actuated devices involve simple designs of a pair of electrodes compared to electromagnetic or piezoelectric actuators which usually require coils and mechanical elements of complicated topology [2, 4]. Moreover, the fabrication process of electrostatically-actuated micro systems is built on a well-established technology that has been employed for years in the fabrication of integrated circuits (ICs).

Electrostatic actuation relies on the attractive force induced between two conductive plates or elements carrying opposite charges [2]. This force depends on the applied potential between the two elements in addition to dielectric constant of medium in between and the distance separating them.

One complication in the use of electrostatically actuated MEMS is the appearance of the pull-in instability. In some applications such as micro switches, it is desirable to accurately predict the onset of such instability. In other applications such as resonators, it is required to extend the limit of such instability, thus extend the travel range of the resonator.

1.1.3 Pull-in instability

The pull-in instability occurs when the voltage drop across the capacitor reaches a critical value where the elastic restoring force of the flexible structure can no longer balance the electrostatic force. Beyond this point, the structure loses stability and snaps down to touch the fixed electrode. The pull-in instability is a saddle-node bifurcation where a stable and an unstable solution branches meet and annihilate each other [5].

A large displacement range can provide the structure with better tuning and a larger range of travel which is useful in a wide variety of tunable MEMS applications. In contrast, pull-in instability limits the structure stable displacement range. It also poses a major safety concern for the operation of electrostatic MEMS where it occurs as an unintended consequence [6]. In MEMS switches, it constitutes the border between on and off states of the switch.

To have more insight into the pull-in phenomenon, we introduce a one-dimensional lumped-mass model to represent an electrostatically actuated MEMS as shown in Fig. 1.1. The effective stiffness of the structure is modeled by a linear spring with a spring constant k and the effective mass is lumped into the mass m as shown in the figure. The initial capacitor gap between the moving flexible plate and the fixed plate is d and the displacement of the mass is w. The capacitive force between two identical parallel capacitor plates is given by [1, 7]

$$F_e = \frac{1}{2}\,\epsilon A\,\frac{V^2}{(d-w)^2} \tag{1.1}$$

where A is the surface area of the plate, ϵ is the electric permittivity of the medium

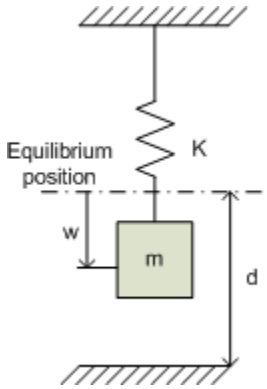

Figure 1.1: *A 1-D lumped-mass model.*

and V is the voltage drop across the plates. We note from this equation that an increase in the voltage V would increase the electrostatic force F_e which in turn increases the displacement w, thus increases the electrostatic force more. At some voltage, an instability occurs and the electrostatic force exceeds the mechanical restoring spring force and as a result, the beam snaps down to touch the bottom electrode. This instability is known as static pull-in [7]. The corresponding voltage is referred to as static pull-in voltage V_{SP}.

At lower voltage values, equilibrium occurs when the electrostatic force F_e is equal to the mechanical restoring force

$$k\,w = \frac{\epsilon A\,V^2}{2(d-w)^2} \tag{1.2}$$

We note that Eq. (1.2) is a third-order polynomial in the beam displacement w. This equation has three roots. One of the roots is always larger than the capacitor gap ($w > d$) which is unphysical, since it requires the upper electrode to penetrate into the lower electrode, and thus will be discarded. The other two roots correspond to two equilibrium positions of the mass. The smaller root corresponds to a stable equilibrium position (node), while the larger corresponds to an unstable equilibrium (saddle) [6]. Figure 1.2 depicts the force balance underlying these equilibria. A small displacement away from equilibrium will diminish over time at the lower equilibrium point since the mechanical restoring force of the bridge is larger than the electrostatic force at this point. This situation is reversed at the upper equilibrium

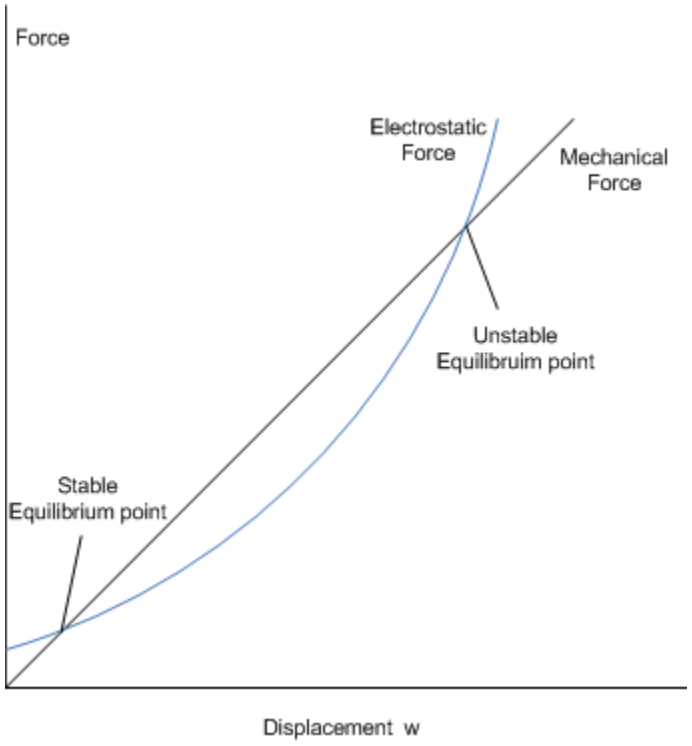

Figure 1.2: *Equilibrium points of the lumped-mass model.*

point where any small displacement from equilibrium will increase over time as the electrostatic force exceeds the mechanical restoring force beyond this point as shown in Fig. 1.2.

As the applied voltage increases, the two equilibrium points move closer to each other until they merge into one point at which the two force curves are tangent. Beyond this point, the movable plate snaps down and touches the fixed plate indicating pull-in. To show this behavior, we rearrange Eq. (1.2) in the form

$$w\,(d-w)^2 = \frac{\epsilon A V^2}{2k} \tag{1.3}$$

where its solution is basically the intersection of the graphs produced by plotting the two functions on both sides of the equation. We note from Fig. 1.2 that pull-in occurs when the intersection of the two force curves merge into one point; thus [4]

$$\frac{d}{dw}\Big[w\,(d-w)^2\Big] = \frac{d}{dw}\Big(\frac{\epsilon A V^2}{2k}\Big) = 0 \tag{1.4}$$

since the right hand side of the equation does not depend on w. This yields a travel range of one-third of the gap between the two plates, $w = d/3$. Upon substitution of this value of displacement into Eq. (1.2), we obtain a formula for pull-in voltage [4, 7]

$$V_{\mathrm{SP}} = \sqrt{\frac{8}{27}\frac{d^3 k}{\epsilon A}} \tag{1.5}$$

It is worth stressing that this value of the pull-in voltage corresponds to a linear mass-spring system.

Another version of the pull-in instability occurs in dynamic systems. Under this scenario, the transient motions or steady-state oscillatory motions of an electrostatic MEMS grow large enough to approach the stable manifold of the saddle, touch the manifold which results in the saddle propelling the system response into pull-in (initial conditions like B in Fig. 1.3. This version of the instability is called dynamic pull-in [8] and the voltage corresponding to it is dubbed dynamic pull-in voltage V_{DP}. We note from Fig. 1.3 that the solution trajectory depends on the initial conditions. For example, initial conditions like A inside the homoclinic orbit home onto the stable node C.

Nayfeh *et al.* [8] show that dynamic pull-in results from the addition of a resonant AC component to the forcing and that it can occur at much lower voltages than the static pull-in voltage where the excitation is purely a DC force. In particular, the dynamic amplification obtained by adding a resonant AC actuation force to the static DC component helps pull-in happen at lower voltages.

Extensive research has been carried on electrostatically actuated devices in order to enhance their functionality in different applications including MEMS switches and MEMS resonators. Many papers have been published on this topic in recent years. Some of them studied the static and dynamic behavior of these systems either analytically or experimentally [8–11].

Many researchers have presented various designs to improve the performance of electrostatic MEMS. Hung and Senturia [12] introduced a new structural design to

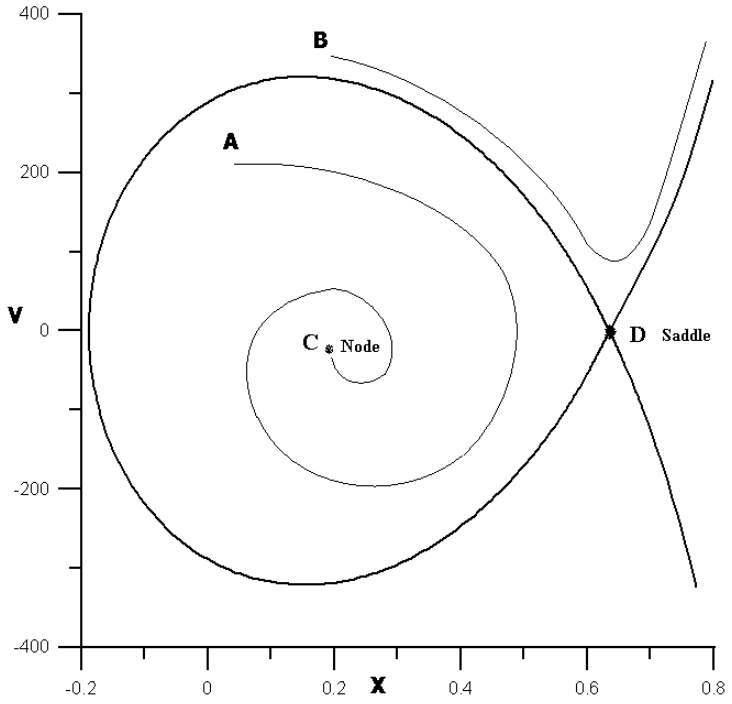

Figure 1.3: *Dynamic pull-in in a damped unforced electrostatic oscillator.*

increase the travel range of electrostatically actuated micro beams to about 60 % of the gap at the cost of increasing the actuation voltage. Their idea was to retard the pull-in instability by applying the electrostatic force to only the portions of doubly-clamped or cantilever beams close to the supports. Thus, while the electrostatically actuated portions of the structure deflect less than the pull-in limit, the other portions of the structure can move through the entire gap.

Busta *et al.* [13] introduced a design where a conductive shield with an opening is interposed between the movable beam and the ground electrode. The shield has the same voltage as the cantilever while it is isolated from the substrate except at the holes. This results in an electrostatic field that is only effective in the opening areas while other areas of the electrode are field-free. The design enabled the control of pull-in forces but also resulted in an increase of pull-in voltage requirements.

Rosa *et al.* [14] introduced a novel curved cantilever beam design where the electrodes are offset from the actuator rather than being positioned directly underneath it. This design provided increased range of motion of the cantilever beam. However, the actuation voltage has increased.

1.2 Motivation

Although electrostatic actuation suffers from the pull-in instability, it also offers one of the highest energy densities available today. In fact, the pull-in instability is not always a drawback. The basic idea of MEMS series and shunt switches is to drive the switch to the pull-in limit and thus obtain the on/off states of a switch. The challenge in this case is the high actuation voltage usually encountered in most MEMS switches.

In this work, we show analytically and experimentally that the actuation voltage can be significantly decreased if we change the waveform used to actuate the switch. Reducing the actuation voltage does not only reduce operational requirements, but also increases the switch lifetime and reduces the effects of dielectric charging.

On the other hand, the pull-in instability causes a perennial problem for MEMS sensors. In this case, one wants to avoid driving the sensor close to its pull-in threshold, otherwise it would lose its functionality. This work proposes a technique to exploit the pull-in instability as a detection mechanism in electrostatic MEMS sensors. The sensor in this case detects that the measurand has exceeded a threshold by going into pull-in. The outcome is a binary sensor that dispenses with readout electronics used in all MEMS sensors. The simplicity of such a sensor makes it a good competitor to other available MEMS sensors.

1.3 MEMS Switches

Because of its high isolation, small size and weight, and low insertion loss at microwave frequencies, MEMS switches can replace the GaAs switches in cellular phones resulting in much lower DC-power consumption and longer battery life. It is also superior to the conventional solid-state switches based on PIN diodes or GaAs field effect transistors (FETs) [15]. This is mainly because of the near-zero power consumption of MEMS switches due to the very small current it consumes. Moreover, because MEMS switches are fabricated using surface micro machining

techniques, they are candidates for low cost [16].

MEMS micro switches have many practical applications; RF-MEMS is one of them. "The term RF-MEMS refers to the design and fabrication of MEMS for RF integrated circuits and it should not be interpreted as the traditional MEMS devices operating at RF frequencies. The main uses of RF switches in the telecommunication industry are for signal routing, in impedance matching networks, and for changing the gain of amplifiers. The RF switch can be used to share an antenna between a transmitter and a receiver. In digital modulation in communication systems, the switch serves as a gate to pass and stop the signal so that the desired waveform can be generated" [17]. Moreover, it is also implemented in phase shifters which are used in telecommunication, automotive, and defense applications [18].

The common type of capacitive micro switches takes the form of capacitive (metal-insulator-metal) contact. This design consists of four main elements: "a high-resistivity silicon substrate, coplanar waveguide transmission lines (CPW) which exhibit low losses at high frequencies, a suspended bridge upon which motion supplies the on/off states for the switch, and a dielectric layer which serves to prevent stiction between the bridge and the underlying CPW center conductor, yet provides a low impedance path between the two metallic surfaces" [19].

The actuation methods of MEMS micro switches can be electrostatic, magnetic or electromagnetic. The advantage of electrostatic actuation is that there is very small current consumption. However, its drawback is that it requires a higher actuation voltage, typically 5-100 V. The advantage of electromagnetic actuation is the lower actuation voltage but with significantly higher current consumption [17].

There are two main switches used in RF circuit design: the shunt switch and the series switch. "The shunt switch is placed in shunt between the transmission line and ground. Thus it either leaves the transmission line undisturbed or connects it to ground. The ideal shunt switch results in zero insertion loss when no bias is applied (up-state position) and infinite isolation when bias is applied (down-state position). Series micro switch geometry follows the same definitions as for the shunt switch but a cantilever beam is used as an actuator instead of the clamped-clamped

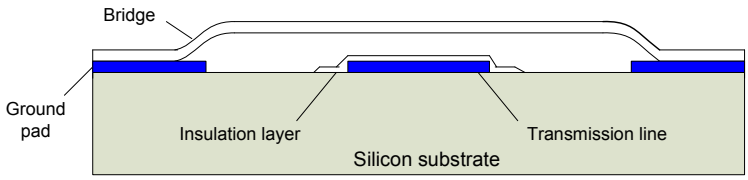

Figure 1.4: *Schematic of a shunt micro switch.*

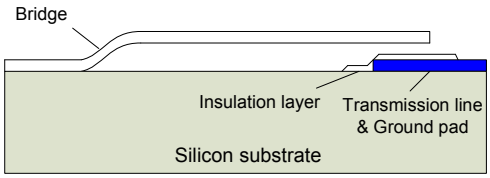

Figure 1.5: *Schematic of a series micro switch.*

beam used in shunt switches.

In shunt micro switches, a static DC voltage is applied between the MEMS bridge and the microwave line. If the DC bias exceeds the static pull-in limit of the switch, this results in an electrostatic force that causes the MEMS bridge to collapse on the dielectric layer, largely increasing the bridge capacitance by a factor of 30-100. This capacitance connects the transmission line to the ground and acts as a short circuit at microwave frequencies, resulting in a reflective switch. When the bias voltage is removed, the MEMS switch returns back to its original position due to the restoring spring forces of the bridge.

In series micro switches, a 40- to 100-μm gap (open circuit) is created in the microwave transmission line when the switch is in the up-state position resulting in high isolation. When the switch is activated, it falls down on the transmission line and creates a short circuit between the open ends. Series switches are DC-contact switches and can work at low frequencies (1000 MHz or lower). Since the MEMS switch creates a DC contact with the transmission line when activated, a separate electrode is needed to actuate the switch. When the bias voltage is removed, the switch returns back to its original position due to the internal restoring force of the cantilever" [18]. Schematics of a shunt switch and a series micro switch are shown in Figs. 1.4 and 1.5, respectively.

Some factors that negatively affect the performance of capacitive micro switches are creep, fatigue, stiction to the insulator, and charging and degradation of the insulator [20]. Moreover, the actuation voltages of RF MEMS switches are usually high. The high actuation voltages result in a reduction of the lifetime of RF MEMS switches [21] and often induces malfunction by charge trapping problems [22]. One of the problems that face electrostatically-actuated MEMS switches is its low mechanical stability. The small electrostatic force makes it difficult for the switches to be mechanically robust and to provide high isolation due to the restriction imposed on the maximum initial gap [22].

Reliability is the main challenge hindering the commercialization of MEMS switches. Most RF MEMS switches require high actuation voltages, which degrade their lifetime and induce malfunction by dielectric charging in capacitive switches [22, 23]. Dielectric charging leads to erratic behavior and limits the device lifetime [24]. In fact, Goldsmith *et al.* [25] showed that capacitive switches exhibit exponentially decreasing lifetime with actuation voltage.

There are three routes to dielectric charging [24]: charge distribution throughout the dielectric material, presence of charges at the interface between the dielectric and the RF line, and injection of charges from the suspended bridge to the dielectric material. Peng *et al.* [26] experimentally showed that dielectric charging is significant when the suspended electrode comes in contact with the dielectric material. Further, during switch operation, the electric field across the capacitor can be as high as 10^6 V/cm, causing electrons or holes to be injected into and trapped within the dielectric. Over time, charge builds up in the dielectric, resulting in actuation-voltage shifts [27, 28]. Charge injection in the dielectric layer also leads to stiction between the dielectric film and the suspended electrode.

Many designs have been proposed to reduce the actuation voltage of MEMS switches and hence enhance their reliability. To reduce the voltage requirements for switching while counteracting self-actuation caused by high RF power in the transmission line, Peroulis *et al.* [29] introduced a switch with a small capacitor gap and serpentine springs in addition to an extra electrode on top of the actuated

bridge. This design reduces the actuation voltage by 65 %, however, the springs consume more area and are also hard to model and fabricate.

Cho *et al.* [22] reported a MEMS switch actuated by a combination of electromagnetic (Lorentz) and electrostatic forces. Electromagnetic actuation is used for the initial gap closing and low-voltage electrostatic actuation is used to hold the switch in the down state. The DC voltage required is 3.3 V, but the switch uses a DC current of 49 mA to generate the Lorentz force.

Sadek *et al.* [30] introduced an electrostatically actuated corrugated bridge suspended over a CPW transmission line operating at $0.1 - 100$ GHz. The micro beam corrugations have the effect of reducing the switch actuation voltage. They also reported that the addition of holes to the corrugated switch results in a decrease in the overall stiffness, thus reducing the actuation voltage further. Other publications addressing different factors affecting RF switch performance can be found in [31–33]. It is worth noting that the aforementioned studies introduced new switch designs to enhance the power handling capabilities and voltage requirements of MEMS switches employing static DC voltage as the actuation method for the switch. This method is referred to as 'static actuation'.

In the context of micro switch actuation, we distinguish between two modes of actuation: static and dynamic actuation. In the static actuation, the structure is merely actuated by a DC voltage and pull-in is referred to as *static pull-in*, V_{SP}. In dynamic actuation, the structure is actuated by a biased AC voltage and pull-in in this case is referred to as *dynamic pull-in*, V_{DP}. In this work, we exploit dynamic pull-in to decrease the actuation voltage of MEMS shunt capacitive switches.

The literature lacks extensive experimental work to study the effect of dynamic actuation, in which an AC forcing component is added to the DC bias voltage, on the response of electrostatically actuated micro switches. In what follows, we summarize some of the published work addressing dynamic actuation.

Seeger and Boser [34] proved experimentally that the oscillation of electrostatic actuators driven near resonance can exceed one-third of the gap distance. They report measured actuator travel range greater than 56 % of the gap where the

excitation frequency has been tuned to drive the actuator to maximum oscillations.

Nielson and Barbastathis [35] proved theoretically using an energy-based technique that the pull-in voltage can be reduced to about 30 % compared to static actuation if the forcing frequency is modulated at the mechanical resonant frequency of a switch. Nielson *et al.* [36] further proved this voltage saving experimentally. They also reported a switching time of 500 ns.

Nayfeh *et al.* [8] showed numerically using a reduced-order model and the shooting method that dynamic pull-in occurs at much lower voltages than static pull-in.

Fargas-Marques and Shkel [37] used energy methods to prove that the travel range of electrostatic parallel-plate actuators can be extended beyond the one-third gap limit up to 50% of the gap under DC-AC forcing combination. They also derived a dynamic pull-in condition that defines a domain of non-resonant actuation voltages, V_{DC} and V_{AC}, at different values of the quality factor for stable parallel-plate actuator motion. Their model does not consider geometric nonlinearities in the system.

Fargas-Marques *et al.* [38] extended their previous work to study the pull-in instability under resonant excitation considering the nonlinear spring effect that appears with large amplitude oscillations. They used energy methods to derive analytical expressions for static and dynamic pull-in voltages. They also derived an analytical resonant pull-in condition for a combination of DC-AC actuation to achieve a maximum stable travel range. They validated these results experimentally using two doubly-clamped micro beams.

Vummidi *et al.* [39] implemented dynamic actuation in a lateral contact RF-MEMS series switch where a voltage saving of about 50 % was experimentally found.

In this study, we investigate the effect of dynamic actuation on the performance of MEMS shunt RF-switches. Dynamic actuation employs a harmonic AC voltage component added to the DC voltage used for biasing the switch. The effect of AC actuation voltage on the response of resonant micro switches is expected to result in high energy savings that help operate the switch at much lower DC bias voltages.

We prove our claim of voltage saving in MEMS shunt switches under DC and AC forcing conditions by conducting experimental work on doubly-clamped micro switches. We also present a theoretical model to model the dynamics of the switch in order to arrive at optimized working conditions for such devices. We show in Chapter 2 how much voltage saving is obtained when the switch is being operated under dynamic actuation which can make the switch operate at much lower DC bias voltages. Numerical and experimental results for MEMS sunt switches are presented in [40]. A voltage saving of about 60 % under dynamic actuation conditions was found.

1.4 MEMS Mass Sensors

Micro mass sensors can accurately detect mass variations on the order of nano- to atto-gram [41]. They are increasingly being used as chemical and biological sensors after equipping them with a functional material to selectively immobilize a particular gas, protein, or organism from a fluid pool or stream. The development of these sensors requires ways to overcome many challenges, including functional material stability and selectivity and overall sensor detection range, response time, hysteresis, and cost [42]. Developing better mass sensors will help address problems of sensitivity, reliability, and cost effectiveness in this new generation of chemical and biological micro sensors.

Two of the more widely used detection modes in micro mass sensors are static and dynamic detection. In the static detection mode, mass variation is detected by measuring the deflection of a micro structure as a result of the mass absorbed or adsorbed on the surface of the functional material. This deflection of the micro structure can be measured optically, piezoresistively, or piezoelectrically. However, most high-resolution systems rely on optical detection [43].

The dynamic detection mode measures the shift in the natural frequency of the sensor due to the absorbed/adsorbed mass. Resonance-based biosensors have exceeded the absolute mass detection capabilities of deflection-based devices, thereby

enabling single cell, virus, and double-stranded DNA molecule detection [44]. Sensors employing these detection modes can be found in many recent papers [42, 43, 45].

We first introduce some of the published work on static detection mode. Datskos and Sauers [46] investigated the sensitivity of gold-coated V-shaped silicon nitride micro cantilevers to 2-mercaptoethanol using optical readout. A sensitivity of 0.432 nm/ppb is achieved with a minimum measured deflection of 10 nm which translates to a sensitivity of 23 ppb.

Jensenius *et al.*[47] used an integrated piezoresistive readout made of a Wheatstone bridge attached to a cantilever beam coated with a polymer film to detect ethanol and other gases. A detection sensitivity of 10 ppm of ethanol was measured.

There has been a concomitant interest in increasing the sensitivity of the underlying mass sensors. In this regard, dynamic detection mode proves to provide better mass sensitivity compared to static mode. Zhang *et al.* [48, 49] showed that the sensitivity of electrostatically actuated MEMS sensors is highly increased if the sensor is parametrically excited. The sensor is composed of two sets of parallel interdigitated comb fingers. They report a mass sensitivity of 1 picogram.

Choi *et al.* [50] experimentally and numerically using FEM showed that the nonlinearities in resonant-based sensors have the effect of enhancing the sensitivity of such systems.

Cleland [51] theoretically investigated the effect of inherent nonlinearities in electrostatic MEMS on mass detection sensitivity. The case of parametrically excited cantilever-type resonator was studied.

Tseytlin [52] derived an analytical model for a micro cantilever-based mass sensor to prove that higher order modes are more sensitive to masses deposited along the beam length except at the nodal points. He found that the second bending mode is 40 times more sensitive to mass variation than the first bending mode and that the sensitivity increases further for higher order modes.

Dohn *et al.* [53] experimentally investigated the sensitivity of a cantilever beam mass sensor to the location of the added mass along the beam. They found that

the highest sensitivity occurs at the beam tip and that the added mass had no significant effect on the Q-factor of the sensor. They also found that the sensitivity of a fourth bending mode dynamic mass sensor is 300 times that of a sensor using the first bending mode. They concluded that sensitivity increases with mode number due to a decrease in the effective mass and an increase in the Q factor as the mode number increases.

Lobontiu *et al.* [54] developed a lumped-mass model for the dynamics of micro bridge mass sensors. They found that the frequency of the first bending mode is more sensitive to the position of the deposited mass along the beam than the first torsional mode. Lobontiu *et al.* [55] extended this work to cantilever beam mass sensors. They presented an analytical model to estimate the resonance frequencies of the first bending and torsion modes and their sensitivities to variations in the mass. Their results show that the first torsional mode is more sensitive than the first bending mode to variations in the mass and its position along the beam. These results were verified experimentally on micro- and nano-scale cantilevers.

Xie *et al.* [56] investigated sensitivity of dynamic mode cantilever beam micro mass sensors. They presented a model to predict the shift in the frequency of the first torsional mode as a function of the mass and attachment position of micro and nano objects. They also conducted an experiment to investigate the sensitivity of the frequencies of the first and second flexural and first torsional modes in air to a ragweed pollen located at different positions along the beam. Their experimental results showed that the sensitivity of the first torsional mode is an order of magnitude higher than that of the first bending mode.

Younis and Alsaleem [57] presented two devices using micro clamped-clamped and micro cantilever beams operating near dynamic pull-in: a switch triggered by mass detection (STMT) and a mass sensor amplified response (MSAR). The STMT utilizes the escape from a potential well phenomenon under primary resonance to drive the micro beam to pull-in. The MSAR uses the jump phenomenon of a pitchfork bifurcation to sense an added masses. They verified these results experimentally using a micro cantilever beam with proof mass.

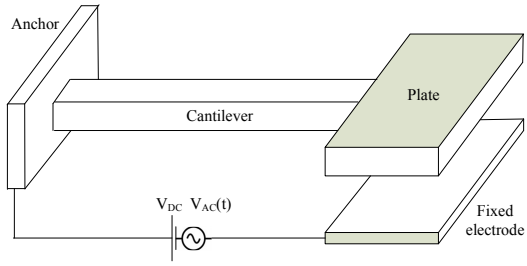

Figure 1.6: *Schematic of a cantilever-type micro sensor.*

To achieve even higher mass sensitivity, NEMS-based sensors have also been introduced. Ilic *et al.* [41] used a resonating mechanical nanocantilever for virus detection. A mass of 3×10^{-15} grams was detected.

Cantilever-based mass sensors show potential for very high mass resolution [43]. In this study, we investigate two versions of a cantilever-based binary gas sensor. The first version is a static sensor while the second is a dynamic sensor. The detection mechanism in both versions is built on measuring the change in a bifurcation point due to added mass. Numerical results show a minimum detectable mass of 3 nanograms for the static sensor and 1 picogram for the dynamic sensor. A schematic of a cantilever-type micro sensor is shown in Fig. 1.6.

1.5 Scope

The objective of this study is to exploit instabilities in electrostatically actuated MEMS to devise new switching and sensing mechanisms. Specifically, we investigate the use of the dynamic pull-in instability to design low-voltage micro switches and static and dynamic pull-in to design simple micro gas sensors.

- We propose a method to actuate MEMS switches using a combination of DC and AC excitation forces. Our hypothesis is that addition of a well-tuned AC component to the actuation signal has the effect of reducing the voltage requirements of the switch compared to pure DC excitation.

- We also propose a parameter identification routine to estimate experimentally

the micro switch model parameters.

- We develop a theory and practice for dynamic switching. Further, we introduce practical switching methods for such mode.

- We investigate the use of the pull-in instability to increase the sensitivity and simplify the configuration of MEMS mass sensors. The idea is rooted in two characteristics of the pull-in instability:

  - the sensitivity of electrostatic MEMS is at a maximum near pull-in,

  - pull-in is a binary detector that classifies disturbances into those that pass the threshold required to trigger pull-in and those that do not.

- Thus, we operate the sensor very close to pull-in and track the sensor response. Pull-in in this case indicates that accumulation of absorbed/adsorbed mass on the sensor are equal or larger than that required to trigger pull-in. This new detection methodology has the advantage of simplifying the sensor setup by eliminating the need for readout electronics since the detector is the mere fact of pull-in itself. This is valuable not only because of the savings in the electronics but also because the integration of MEMS and electronics requires either building MEMS in CMOS or wire bonding after the fabrication of each.

- We develop two versions of this binary mass sensor. The first version uses static pull-in as a detection mechanism, while the second version uses dynamic pull-in as a detection mechanism. This mass detection method is different from the commonly practiced methods of detecting the deflection or the shift in frequency of a structure due to an added mass.

1.6 Thesis Outline

This thesis is organized into four chapters. In Chapter 1, an introduction to MEMS and its actuation techniques is presented. The pull-in instability is discussed and

explained. Literature review of MEMS switches and MEMS sensors is then presented.

In Chapter 2, we present a mathematical model of a shunt MEMS micro switch. We discuss methods to identify the geometric and material parameters of the switch. We use the model predictions and experiments to design dynamic actuation techniques for MEMS switches. We also identify the damping mechanisms available in the switch and study dielectric charging during switching.

In Chapter 3, we present a mathematical model for a binary micro mass sensor composed of a plate suspended at the end of a cantilever beam. We design static and dynamic versions of the binary mass sensor and demonstrate the static version of the sensor. We investigate the factors affecting the sensor sensitivity including its geometric and material properties.

In Chapter 4, we draw conclusions from our findings in this work and provide recommendations for future work on the exploitation of electrostatic MEMS instabilities in actuation and sensing.

Chapter 2

Dynamic Switching

In this chapter, we investigate the effect of dynamic switching on the performance of electrostatically actuated capacitive micro switches. We derive the equation of motion and the associated boundary conditions governing the nonlinear response of a capacitive shunt micro switch to electrostatic actuation. The switch is composed of a fixed-fixed micro beam suspended over a fixed bottom electrode. We use Hamilton's principle as a variational approach to derive the equation of motion and give a brief introduction to reduced-order modeling. We base our reduced-order models on the Galerkin method. With the Galerkin method, the governing nonlinear partial-differential equation in space and time is discretized into a set of nonlinearly coupled ordinary-differential equations in time only. The linear undamped free vibration mode shapes, around the statically undeflected position of the beam, are used as basis functions in the Galerkin method. We also present the experimental results we obtained using a laser vibrometer and compare them with the numerical results achieved from the model. Our model as well as numerical and experimental results for the capacitive MEMS shunt switch are summarized in [40].

2.1 Switch Model

We model the MEMS shunt switch as a straight beam of uniform cross-section and homogeneous material with mass per unit length m, length L, thickness h, width b,

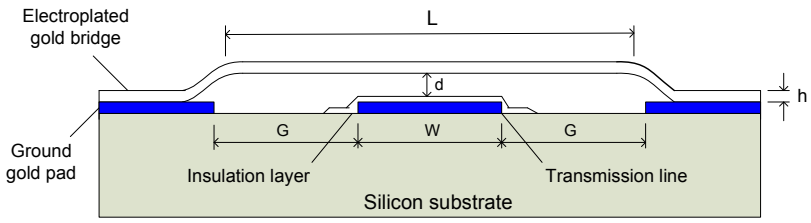

Figure 2.1: *Schematic of the shunt micro switch.*

cross-section area A, moment of inertia I, and modulus of elasticity E. The bridge is anchored to two ground lines on either side of a coplanar waveguide (CPW) transmission line of width W and held at a distance d above the CPW, as shown in Fig. 2.1. The distance between the signal line of the CPW and each of the ground lines is denoted as G.

Although MEMS dimensions are in the microscale, the theory of continuum mechanics is still applicable. According to Luan and Robbins [58], the applicability of continuum mechanics is valid even at a few atomic diameters which are of the nanoscale. The beam is modeled according to the Euler-Bernoulli beam theory. The main assumptions of this theory are [59]

- Planes remain plane after deformation, i.e., the in-plane strains are negligible.
- Straight lines normal to the midplane of the beam remain straight and normal after deformation, i.e., transverse shear strains are ignored and consequently the rotation of cross-sections is only due to bending.
- Straight lines in the transverse direction of the cross-section do not change length, i.e., the out-of-plane strains are ignored.

Moreover, the electrostatic force between the micro beam and the bottom electrode is modeled according to the parallel-plate theory. According to this theory, the micro beam shape is assumed to be always straight and parallel to the bottom electrode at any forcing level. This is a reasonable assumption since the ratio of beam deflection to its span is in the order of 1/100.

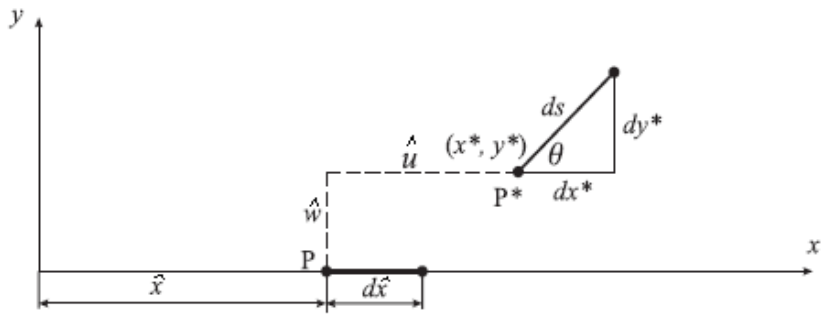

Figure 2.2: *A segment of the micro beam before and after deformation [59].*

We follow Emam [59] in the derivation of the equation of motion governing the transverse vibrations of the micro beam. We consider a differential element of length $d\hat{x}$, located at point P a distance $\hat{x}$ form the origin, in the undeformed configuration of the microbeam. After deformation, the point P moves to a new location P^* of coordinates

$$x^* = \hat{x} + \hat{u} \qquad \text{and} \qquad y^* = \hat{w} \tag{2.1}$$

where $\hat{u}$ and $\hat{w}$ are the displacements along the $\hat{x}$ and $\hat{y}$ directions, respectively, as shown in Fig. 2.2. The element has a length ds in the deformed configuration given by

$$ds = \sqrt{dx^{*2} + dy^{*2}} \tag{2.2}$$

Differentiating Eq. (2.1) with respect to $\hat{x}$, we obtain

$$dx^* = (1 + \hat{u}')d\hat{x} \qquad \text{and} \qquad dy^* = \hat{w}'d\hat{x} \tag{2.3}$$

where primes denote derivative with respect to $\hat{x}$. The length of the element in the deformed configuration can be expressed as

$$ds = \sqrt{(1 + \hat{u}')^2 + \hat{w}'^2}\, d\hat{x} \tag{2.4}$$

The elongation of the differential element is given by

$$e = d\hat{s} - d\hat{x} = \left(\sqrt{(1+\hat{u}')^2 + \hat{w}'^2} - 1\right)d\hat{x} \tag{2.5}$$

The angle of rotation θ is given by

$$\begin{aligned} \sin\theta &= \frac{dy^*}{ds} = \frac{dy^*}{d\hat{x}}\frac{d\hat{x}}{ds} = \frac{\hat{w}'}{\lambda} \\ \cos\theta &= \frac{dx^*}{ds} = \frac{dx^*}{d\hat{x}}\frac{d\hat{x}}{ds} = \frac{1+\hat{u}'}{\lambda} \end{aligned} \tag{2.6}$$

where λ is the stretch ratio defined as

$$\lambda = \frac{ds}{d\hat{x}} = \sqrt{(1+\hat{u}')^2 + \hat{w}'^2} \tag{2.7}$$

Differentiating Eqs. (2.6) with respect to $\hat{x}$ assuming small rotation yields

$$\begin{aligned} \sin\theta \approx \theta = \frac{\hat{w}'}{\lambda} \qquad &\Longrightarrow \qquad \theta' = \frac{\lambda\hat{w}'' - \lambda'\hat{w}'}{\lambda^2} \\ \cos\theta \approx 1 = \frac{1+\hat{u}'}{\lambda} \qquad &\Longrightarrow \qquad \lambda' = \hat{u}'' \end{aligned} \tag{2.8}$$

Thus the rotation gradient θ' takes the form

$$\theta' = \frac{(1+\hat{u}')\hat{w}'' - \hat{u}''\hat{w}'}{\lambda^2} \tag{2.9}$$

The curvature of the midplane is given by

$$\kappa = \frac{d\theta}{ds} = \frac{d\theta}{d\hat{x}}\frac{d\hat{x}}{ds} = \frac{\theta'}{\sqrt{1 + 2\hat{u}' + \hat{u}'^2 + \hat{w}'^2}} \tag{2.10}$$

Substituting Eq. (2.9) into Eq. (2.10), we obtain

$$\kappa = \frac{(1+\hat{u}')\hat{w}'' - \hat{u}''\hat{w}'}{[1 + 2\hat{u}' + \hat{u}'^2 + \hat{w}'^2]^{\frac{3}{2}}} \tag{2.11}$$

To obtain a formula representing the mid-plane stretching of the microbeam,

we expand Eq. (2.5) in a Taylor series as

$$e = \left[\frac{1}{2}\left(2\hat{u}' + \hat{u}'^2 + \hat{w}'^2\right) - \frac{1}{8}\left(2\hat{u}' + \hat{u}'^2 + \hat{w}'^2\right)^2 + \cdots\right] d\hat{x} \tag{2.12}$$

where the higher-order terms are neglected. Retaining up to quadratic terms in the displacement gradient, we obtain

$$e \approx \left(\hat{u}' + \frac{1}{2}\hat{w}'^2\right) d\hat{x} \tag{2.13}$$

which gives the elongation of the differential element assuming small-strain and moderate-rotation approximations. Integrating Eq. (2.13) over the domain, we obtain the micro beam midplane stretching

$$\Delta = \hat{u}(L) - \hat{u}(0) + \frac{1}{2}\int_0^L \left(\frac{\partial \hat{w}}{\partial \hat{x}}\right)^2 d\hat{x} \tag{2.14}$$

where $\hat{u}(0)$ and $\hat{u}(L)$ are the axial displacements at the beam ends. For a fixed-fixed micro beam configuration, there are no axial displacements at both ends. As a result, the total midplane stretching is given by

$$\Delta = \frac{1}{2}\int_0^L \left(\frac{\partial \hat{w}}{\partial \hat{x}}\right)^2 d\hat{x} \tag{2.15}$$

The induced axial force due to the mid-plane stretching can be expressed as

$$S = \frac{EA}{L}\Delta = \frac{EA}{2L}\int_0^L \left(\frac{\partial \hat{w}}{\partial \hat{x}}\right)^2 d\hat{x} \tag{2.16}$$

where EA/L is the axial stiffness of the beam. The total axial tensile force on the beam is given by

$$S_t = \hat{N} + \frac{EA}{2L}\int_0^L \left(\frac{\partial \hat{w}}{\partial \hat{x}}\right)^2 d\hat{x} \tag{2.17}$$

where $\hat{N}$ represents the axial force due to residual stresses that may be present in the beam which is negative if the residual stresses are compressive.

To obtain the bending moment at any location of the beam, we expand Eq. (2.11) in a Taylor series as follows:

$$\kappa = \hat{w}'' - \hat{u}''\hat{w}' - 2\hat{w}''\hat{u}' + \cdots \tag{2.18}$$

For small curvature approximation, the curvature of the midplane is given by

$$\kappa \approx \hat{w''} \tag{2.19}$$

The bending moment $M(\hat{x})$ at any location $\hat{x}$ of the beam is given by

$$M(\hat{x}) = EI\kappa = EI\hat{w}'' \tag{2.20}$$

where EI is the bending stiffness of the beam.

The potential energy due to bending is given by

$$\begin{aligned} V_b &= \frac{1}{2}\int_0^L M(\hat{x})\ \kappa\ d\hat{x} \\ &= \frac{EI}{2}\int_0^L \left(\frac{\partial^2 \hat{w}}{\partial \hat{x}^2}\right)^2 d\hat{x} \end{aligned} \tag{2.21}$$

The potential energy due to the axial force $\hat{N}$ is given by

$$V_a = \hat{N}\,\Delta = \frac{1}{2}\,\hat{N}\int_0^L \left(\frac{\partial \hat{w}}{\partial \hat{x}}\right)^2 d\hat{x} \tag{2.22}$$

The potential energy due to midplane stretching is given by

$$V_s = \frac{1}{2}\,S\,\Delta = \frac{EA}{8L}\left[\int_0^L \left(\frac{\partial \hat{w}}{\partial \hat{x}}\right)^2 d\hat{x}\right]^2 \tag{2.23}$$

Therefore, the total potential energy can be expressed as [59]

$$V = \frac{1}{2}EI\int_0^L \left(\frac{\partial^2 \hat{w}}{\partial \hat{x}^2}\right)^2 d\hat{x} + \frac{1}{2}\hat{N}\int_0^L \left(\frac{\partial \hat{w}}{\partial \hat{x}}\right)^2 d\hat{x} + \frac{EA}{8L}\left[\int_0^L \left(\frac{\partial \hat{w}}{\partial \hat{x}}\right)^2 d\hat{x}\right]^2 \tag{2.24}$$

The kinetic energy of a differential element of density ρ, cross-sectional area A, and length $d\hat{x}$ is

$$dT = \frac{1}{2}\,\rho\,A\,\left(\frac{\partial \hat{w}}{\partial \hat{t}}\right)^2 d\hat{x} \tag{2.25}$$

Integrating Eq. (2.25) over the length of the beam gives the total kinetic energy

$$T = \frac{1}{2}\,m\int_0^L \left(\frac{\partial \hat{w}}{\partial \hat{t}}\right)^2 d\hat{x} \tag{2.26}$$

where m is mass per unit length of the micro beam.

The electrostatic force per unit beam length between the beam and the bottom electrode is expressed as [1]

$$F_e = \frac{1}{2}\,\epsilon\,b\,\frac{V(\hat{t})^2}{(d-\hat{w})^2} \tag{2.27}$$

where ϵ is the dielectric constant of the medium between the bridge and the bottom electrode and $V(\hat{t})$ is the applied potential difference across them.

Hamilton's principle is a powerful variational technique for deriving the equations of motion and the associated boundary conditions of distributed-parameter systems. Hamilton's principle states that the variation of the Lagrangian of the system plus the line integral of the virtual work done by nonconservative forces during the time interval from t_0 to t_f must be equal to zero; that is

$$\int_{t_0}^{t_f} (\delta \pounds + \delta W_{nc})\,dt = 0 \tag{2.28}$$

where $\pounds$ is the Lagrangian defined by

$$\pounds = T - V \tag{2.29}$$

where T is the kinetic energy, V is the potential energy, W_{nc} is the work done by nonconservative forces, and δ is a differential operator denoting the first variation.

Using Hamilton's principle, the equation of motion governing the transverse

vibrations of a fixed-fixed micro beam subjected to transverse electric forces can be expressed as [59, 60]

$$m\frac{\partial^2 \hat{w}}{\partial \hat{t}^2} + (\hat{c} + \hat{c}_s)\frac{\partial \hat{w}}{\partial \hat{t}} + EI\frac{\partial^4 \hat{w}}{\partial \hat{x}^4} = \Big[\hat{N} + \frac{EA}{2L}\int_0^L \Big(\frac{\partial \hat{w}}{\partial \hat{x}}\Big)^2 d\hat{x}\Big]\frac{\partial^2 \hat{w}}{\partial \hat{x}^2} + \frac{1}{2}\frac{\epsilon\, b\, V(\hat{t})^2}{(d-\hat{w})^2}\, S \tag{2.30}$$

and the associated boundary conditions are

$$\hat{w}(\hat{x},\hat{t}) = 0 \quad \text{and} \quad \frac{\partial \hat{w}(\hat{x},\hat{t})}{\partial \hat{x}} = 0 \quad \text{at} \quad \hat{x} = 0 \ \text{ and } \ \hat{x} = L \tag{2.31}$$

where $\hat{w}(\hat{x},\hat{t})$ is the transverse deflection of the micro beam.

The voltage difference between the bridge and the CPW is defined as

$$V(\hat{t}) = V_{\text{DC}} + V_{\text{AC}}\cos(\hat{\Omega}\hat{t}) \tag{2.32}$$

where V_{DC} is the magnitude of DC voltage and V_{AC} and $\hat{\Omega}$ are the amplitude and frequency of AC voltage. To account for the electrostatic fringing field, we replace the width of the micro beam b with an effective width [61] in the electrostatic force term; that is

$$b_{\text{e}} = \left(1 + 0.65\,\frac{d-\hat{w}}{\hat{b}}\right)\hat{b} \tag{2.33}$$

The unit-step function S accounts for the incomplete overlap between the transmission line and the bridge

$$S = \begin{cases} 1 & \text{for} \quad \frac{1}{2}(L-W) \le \hat{x} \le \frac{1}{2}(L+W) \\ 0 & \text{elsewhere} \end{cases} \tag{2.34}$$

The sources of damping in the switch are (a) energy losses through the supports, (b) acoustic losses to air, (c) structural damping represented by the viscous damping coefficient $\hat{c}$, and (d) squeeze-film damping due to the air trapped under the bridge represented by the coefficient $\hat{c}_s$. The effect of squeeze-film damping is quantified

using the formula [62]

$$\hat{c}_s = \frac{\hat{\mu}\,\hat{b}^3}{(1+6K_n)(d-\hat{w})^3} \tag{2.35}$$

where $\hat{\mu}$ is the air viscosity, $K_n = \lambda/d$ is the Knudsen number, and $\lambda = 60$ nm is the mean free path of air molecules at ambient pressure.

Dimensional analysis gives a compact way of model representation and reduces the complexity of physical variables where these variables are lumped into a number of nondimensional groups. For convenience, we introduce the nondimensional variables

$$x = \frac{\hat{x}}{L}, \quad w = \frac{\hat{w}}{d}, \quad \text{and} \quad t = \frac{\hat{t}}{T} \tag{2.36}$$

where T is a time scale. Substituting Eq. (2.36) into Eqs. (2.30) and (2.31), we obtain the nondimensional equation governing the transverse vibrations of a micro beam subjected to internal axial forces and DC-AC voltage combination

$$\begin{aligned}\frac{\partial^2 w}{\partial t^2} + (c+c_s)\frac{\partial w}{\partial t} + \frac{\partial^4 w}{\partial x^4} &= \left[N + \alpha_1 \Gamma(w,w)\right]\frac{\partial^2 w}{\partial x^2} \\ &\quad + \alpha_2 \frac{(V_{\mathrm{DC}} + V_{\mathrm{AC}})^2}{(1-w)^2}\left(1 + 0.65\,\frac{1-w}{b/d}\right) S\end{aligned} \tag{2.37}$$

subject to the boundary conditions

$$w(x,t) = 0 \quad \text{and} \quad \frac{\partial w(x,t)}{\partial x} = 0 \quad \text{at} \quad x = 0 \quad \text{and} \quad x = 1 \tag{2.38}$$

The integral operator $\Gamma(f_1, f_2)$, for two functions $f_1(x,t)$ and $f_2(x,t)$, is defined as

$$\Gamma(f_1, f_2) = \int_0^1 \frac{\partial f_1}{\partial x}\frac{\partial f_2}{\partial x}\,dx \tag{2.39}$$

The parameters appearing in Eq. (2.37) are

$$N = \frac{\hat{N}L^2}{EI}, \quad T = \sqrt{\frac{mL^4}{EI}}, \quad c = \frac{\hat{c}L^4}{EIT}, \quad \mu = \hat{\mu}\left(\frac{b}{d}\right)^3\frac{T}{m},$$
$$c_s = \frac{\mu}{(1+6K_n)(1-w)^3}, \quad \alpha_1 = 6\left(\frac{d}{h}\right)^2, \quad \alpha_2 = \frac{6\,\epsilon\,L^4}{Eh^3d^3}, \quad \Omega = \hat{\Omega}\,T \tag{2.40}$$

We simplify the squeeze-film damping coefficient c_s by expanding one factor of $1/(1-w)^3$ in a Taylor series, dropping higher-order terms, and obtaining

$$c_s \approx (\mu_e + \mu_e\, w)\frac{1}{(1-w)^2} \tag{2.41}$$

where $\mu_e = \mu/(1+6K_n)$. The sources of nonlinearity in the system represented by Eq. (2.37) are the midplane stretching, the electrostatic force, and the squeeze film damping quantified by the parameters α_1, α_2, and c_s, respectively.

2.1.1 Reduced-order model

The solution of the free and forced vibration of continuous systems can be represented by an infinite series expressed in terms of the principal modes of vibration. In many applications, high-frequency modes of vibration may not have a significant effect on the solution of the vibration problem. As a result, the contribution of these high-frequency modes can be neglected and the solution may be represented in terms of a finite number of modes or in terms of assumed polynomials that describe the shape of deformation of the continuous systems [63].

We use the Galerkin method, which is one of the weighted residual methods, to discretize the governing equation of the micro beam. The weighting functions are chosen to be the same as the trial functions according to the Galerkin method [63]. In the present study, we use as trial functions in the Galerkin method the mode shapes of the linear undamped free vibration problem governing the vibrations of the micro beam about its statically undeflected position.

In order to obtain the discretized equations governing the static problem, we need first to solve for the linear undamped free vibration mode shapes of the micro

beam and use these modes as basis functions in the Galerkin discretization. In the discretization, we use as trial functions the mode shapes of the linear undamped free vibration problem governing the vibrations of the micro beam around its straight undeflected position. This is done by dropping the nonlinear, damping, and forcing terms from Eq. (2.37). Thus we obtain

$$\frac{\partial^2 w}{\partial t^2} + \frac{\partial^4 w}{\partial x^4} - N\frac{\partial^2 w}{\partial x^2} = 0 \tag{2.42}$$

We solve for the vibration mode shapes governed by Eq. (2.42). Assuming a solution of this equation in the form

$$w(x,t) = \phi_n(x)\, e^{i\omega_n t} \tag{2.43}$$

Thus Eq. (2.42) reduces to

$$\phi_n^{iv} - N\phi_n'' - {\omega_n}^2\phi_n = 0 \tag{2.44}$$

and

$$\phi_n = 0 \quad \text{and} \quad \phi_n' = 0 \quad \text{at} \quad x = 0 \quad \text{and} \quad x = 1 \tag{2.45}$$

Solving Eq. (2.44) gives the linear vibration mode shapes of the undeflected micro beam

$$\phi_n(x) = c_1 \cos k_1 x + c_2 \sin k_1 x + c_3 \cosh k_2 x + c_4 \sinh k_2 x \tag{2.46}$$

where the c_i are constants and

$$k_1 = \pm\sqrt{-\frac{N}{2} + \frac{1}{2}\sqrt{N^2 + 4{\omega_n}^2}} \quad \text{and} \quad k_2 = \pm\sqrt{\frac{N}{2} + \frac{1}{2}\sqrt{N^2 + 4{\omega_n}^2}} \tag{2.47}$$

Substituting the boundary conditions given by Eq. (2.45) into Eq. (2.46) yields four

algebraic equations in the c_i as follows:

$$c_1 + c_3 = 0 \tag{2.48a}$$

$$c_2 k_1 + c_4 k_2 = 0 \tag{2.48b}$$

$$c_1 \cos k_1 + c_2 \sin k_1 + c_3 \cosh k_2 + c_4 \sinh k_2 = 0 \tag{2.48c}$$

$$-c_1 k_1 \sin k_1 + c_2 k_1 \cos k_1 + c_3 k_2 \sinh k_2 + c_4 k_2 \cosh k_2 = 0 \tag{2.48d}$$

This system of equations represents an eigen-value problem for ω_n. Equating the determinant of the coefficient matrix of these equations to zero yields an equation for ω_n. With this value of ω_n and the c_i values, we obtain the linear vibration mode shapes $\phi_n(x)$ of the micro beam around the undeflected position.

To obtain the reduced-order model for the MEMS switch under the combination of DC and AC forcing, we use the linear undamped eigen-value problem of the beam in the undeflected position as a weighting function in the Galerkin discretization. Moreover, we multiply both sides of Eq. (2.37) by $(1 - w)^2$ to keep all the nonlinearities in the governing equation [60].

The solution of Eq. (2.37) is assumed in the following form:

$$w(x,t) = \sum_{i=1}^{N^*} \phi_i(x)\, q_i(t) \tag{2.49}$$

where $\phi_i(x)$ are the trial functions and $q_i(t)$ are generalized coordinates in time. Substituting Eq. (2.49) into Eq. (2.37), multiplying the result by ϕ_n and integrating the outcome from $x = 0$ to $x = 1$ then simplifying using Eq. (2.44), we obtain a

system of ordinary differential equations in time in the form

$$
\begin{aligned}
&\ddot{q_n} - 2\sum_{i,j=1}^{N} \ddot{q}_i q_j \int_0^1 \phi_i\phi_j\phi_n dx + \sum_{i,j,k=1}^{N} \ddot{q}_i q_j q_k \int_0^1 \phi_i\phi_j\phi_k\phi_n dx + (c+\mu_e)\,\dot{q}_n + \omega_n^2 q_n = \\
&\quad \alpha_2\, S\,(V_{\mathrm{DC}} + V_{\mathrm{AC}})^2\Big(1 + \frac{0.65}{b/d}\Big)\int_0^1 \phi_n dx - \frac{0.65}{b/d}\,\alpha_2\, S\, q_n \\
&\quad + 2\sum_{i,j=1}^{N} q_i q_j \omega_n^2 \int_0^1 \phi_i\phi_j\phi_n dx - \sum_{i,j,k=1}^{N} q_i q_j q_k \omega_n^2 \int_0^1 \phi_i\phi_j\phi_k\phi_n dx \\
&\quad + (\mu_e - 2c)\sum_{i,j=1}^{N} \dot{q}_i q_j \int_0^1 \phi_i\phi_j\phi_n dx - c\sum_{i,j,k=1}^{N} \dot{q}_i q_j q_k \int_0^1 \phi_i\phi_j\phi_k\phi_n dx \\
&\quad + \alpha_1 \sum_{i,j,k=1}^{N} q_i q_j q_k \Gamma(\phi_i,\phi_j)\int_0^1 \phi_k''\phi_n dx \\
&\quad - 2\alpha_1 \sum_{i,j,k,l=1}^{N} q_i q_j q_k q_l \Gamma(\phi_i,\phi_j)\int_0^1 \phi_k\phi_l''\phi_n dx \\
&\quad + \alpha_1 \sum_{i,j,k,l,m=1}^{N} q_i q_j q_k q_l q_m \Gamma(\phi_i,\phi_j)\int_0^1 \phi_k''\phi_l\phi_m\phi_n dx, \\
&\quad n = 1, 2, 3, \cdots, N^*
\end{aligned}
\tag{2.50}
$$

where N^* is the number of modes retained in the discretization.

2.2 Experiment

Ploytec MSV-400 laser vibrometer [64] was used to measure the bridge motions. The laser vibrometer system uses the Doppler effect to measure the velocity or displacement of a point of the bridge. A helium neon laser beam is pointed at the target point and the back-scattered laser beam is measured using a photodetector. The motion of the target point modulates the frequency or shifts the phase of the scattered laser beam. The frequency or phase shift is then measured and used to calculate the velocity or displacement of the target point. The vibrometer is mounted on a test station, Fig. 2.3. A vacuum port is used to fix the test specimen to the chuck of the test station. A probe is used to carry the actuation signal to

a pad at the end of the transmission line, while another probe is used to ground a pad connected to the two ground lines. It is worth noting that for the experimental results that follow, V_{DC} is the magnitude of DC voltage and V_{AC} is the amplitude of AC voltage of excitation.

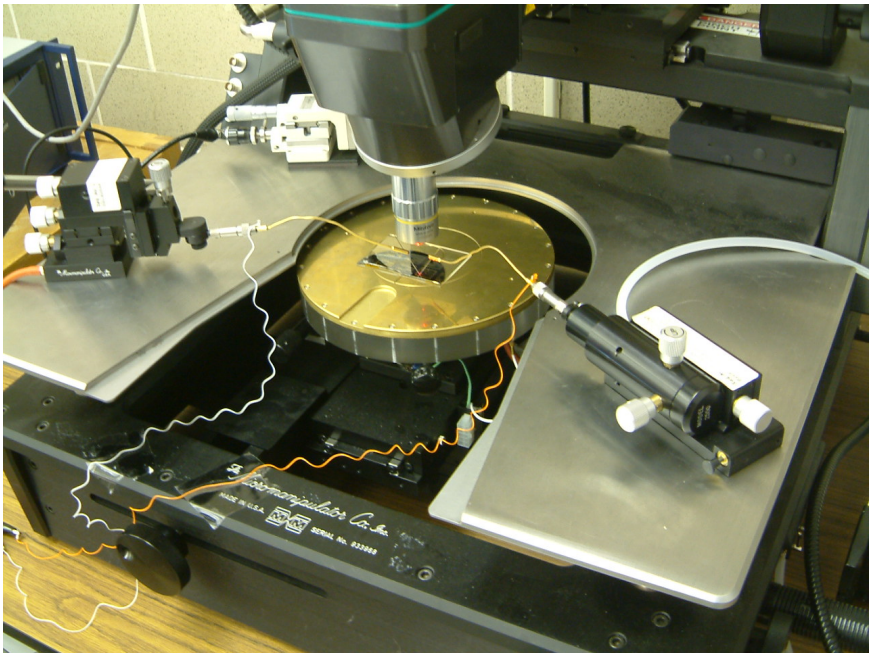

Figure 2.3: *Switch under testing.*

2.2.1 Switch fabrication

The switch, Fig. 2.1, is composed of an electroplated gold bridge fabricated on top of a 50-ohms CPW with dimensions G/W/G = 19/45/19 μm on a 500 μm Si substrate with a 2 μm LPCVD silicon nitride isolation layer. The CPW carries the actuation signal in addition to the RF signal. An SEM picture depicting the switch and CPW is shown in Fig. 2.4.

Figures 2.5(a)– 2.5(d) illustrate the procedure used to fabricate the MEMS switch. The CPW line was first defined using a lift-off process by evaporating a 500/2500 Å layer of Cr/Au. A 1500 Å SiN dielectric (PECVD) layer was then deposited and patterned. Then, a 1.5 μm thick sacrificial layer of photoresist (S1813) was deposited and patterned. This layer defines the gap between the bridge and

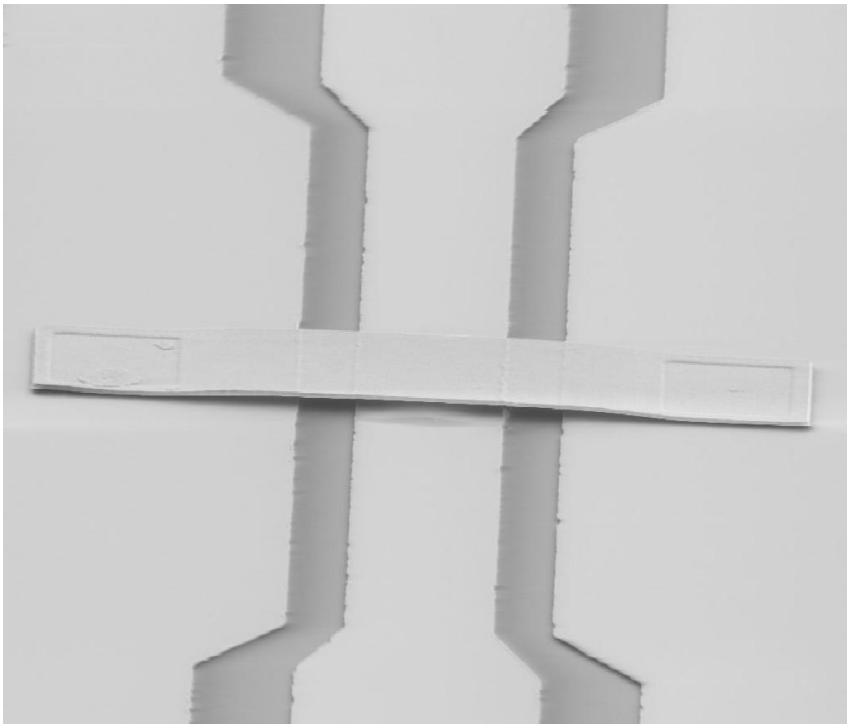

Figure 2.4: *SEM picture of the switch.*

the signal line and also defines the anchors, as shown in Fig. 2.5(c). A blanket of 450/750/300 Å Ti/Au/Ti seed layer was evaporated and later patterned with photoresist above to define the switch thickness and its width. The thickness of the electroplated Au layer is 1.7 μm. The sacrificial layer was removed using a photoresist stripper after the etch back of the seed layer stack (Ti/Au/Ti) and the switch was released. A critical point dryer was used to avoid stiction between the electroplated switch and the signal line below during removal of the sacrificial layer [65].

2.2.2 Parameter estimation

The model requires estimates of the beam dimensions and axial load to predict the switch behavior. A white light optical profilometer, Wyko-NT1100 [66], was used to obtain the beam surface topography shown in Fig. 2.6. The beam length and width listed in Table 2.1 were measured from this profile. The combined beam thickness and capacitor gap was also measured as $h_T = h + d = 3.4$ μm. Further, we

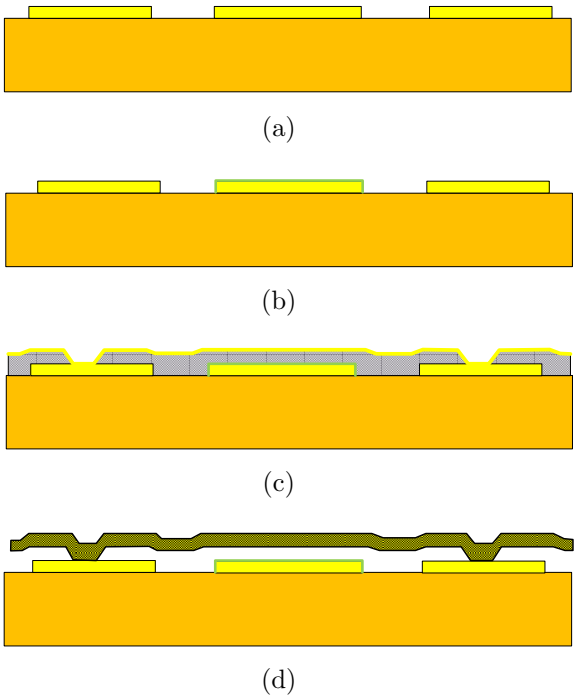

Figure 2.5: *Fabrication procedure of the capacitive shunt switch: (a) CPW patterning; (b) Dielectric layer, PECVD SiN, deposition and patterning; (c) Sacrificial layer deposition, anchors patterning, and seed layer (Ti/Au/Ti) deposition by evaporation; and (d) Au electroplating and sacrificial layer removal followed by Critical Point Dryer release [65].*

obtained initial estimates of the beam thickness $\tilde{h}$ and capacitor gap $\tilde{d}$ by measuring the height of the structural gold layer over the ground lines in the post area, Fig. 2.6. The curvature shown in the figure may be due to anti-clastic curvature induced by the Poisson's effect or possibly due to the thermal stresses within the structure.

The use of electroplating leads to surface roughness and uncertainties in the thickness h and gap distance d. Residual stresses σ may also occur during fabrication, resulting in axial forces in the bridge. A parameter identification routine was developed to estimate these parameters by matching the experimental results to model predictions of the natural frequency as a function of the DC voltage.

The eigenvalue problem describing the free vibrations of the beam around a

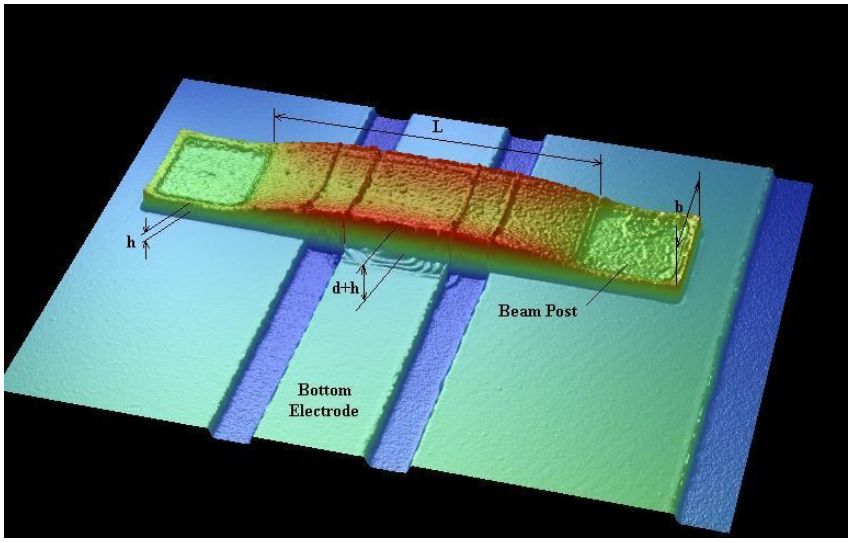

Figure 2.6: *Beam profile using a white light profilometer showing the measured parameters.*

statically deflected position $w_s(x)$ is given by [67]

$$\phi_n^{iv} - [N + \alpha_1 \Gamma(w_s, w_s)]\phi_n'' - 2\alpha_1 \Gamma(w_s, \phi_n) w_s'' = \left(\omega_n^2 + \frac{2\alpha_2 V_{\mathrm{DC}}^2}{(1 - w_s)^3}\right)\phi_n \qquad (2.51)$$

subject to the boundary conditions

$$\phi_n = 0 \quad \text{and} \quad \phi_n' = 0 \quad \text{at} \quad x = 0 \quad \text{and} \quad x = 1$$

where ϕ_n and ω_n are the mode shape and natural frequency of the nth bending mode around the equilibrium position $w_s(x)$. The second term on the right-hand side of Eq. (2.51) accounts for the drop in the natural frequency with increasing the DC voltage as seen in Fig. 2.7. For an unactuated bridge ($V_{\mathrm{DC}} = 0$), Eq. (2.51) reduces to

$$\phi_n^{iv} - N\phi_n'' - \omega_n^2 \phi_n = 0 \qquad (2.52)$$

Inspection of Eq. (2.52) shows that the natural frequency ω_n depends solely on the axial force N at $V_{\mathrm{DC}} = 0$. Therefore, N can be estimated by matching the natural frequency predicted numerically to that measured experimentally at the y-

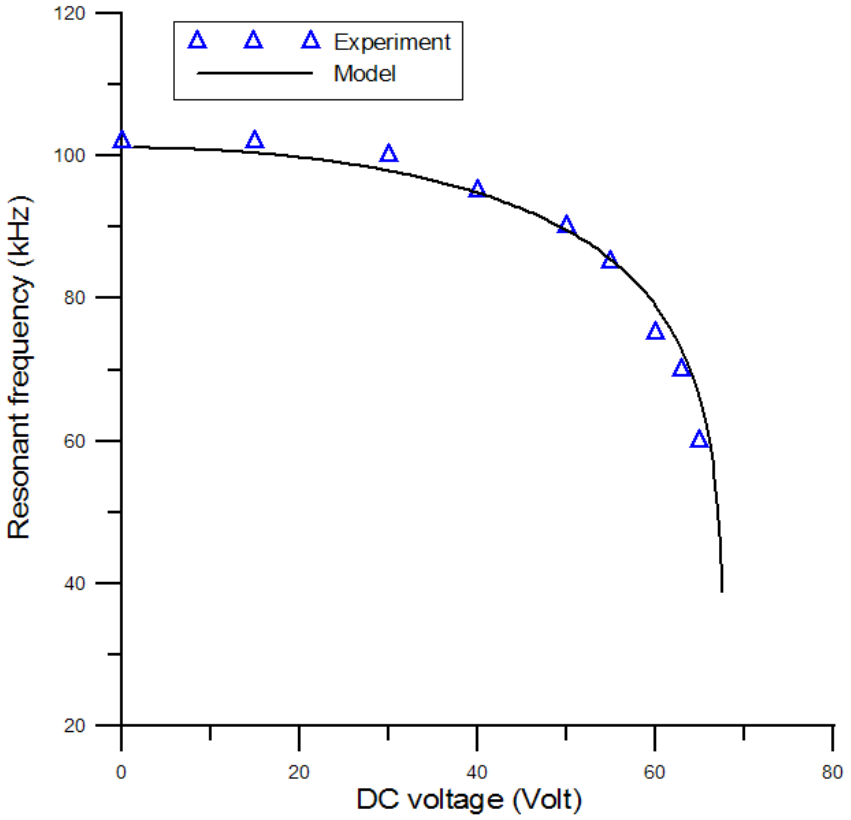

Figure 2.7: *Variation of the fundamental natural frequency with the DC voltage.*

intercept of the natural frequency-DC voltage curve, Fig. 2.7. Assuming an average gold density $\rho = 19320$ kg/m^3 and modulus of elasticity $E = 80$ GPa, we estimated the tensile stress $\sigma = 17$ MPa.

To obtain the natural frequency-DC voltage curve experimentally, we excited the switch with a small AC voltage and a fixed DC bias V_{DC_i}. As the beam oscillated around the corresponding static equilibrium $w_{s_i}(x)$, the laser vibrometer was used to measure the velocity of the bridge midpoint. To take advantage of the reduced noise floor in the frequency domain, we obtained the amplitude of the midpoint velocity from the peak in the FFT at the excitation frequency Ω. We increased the frequency of excitation in discrete steps and recorded the excitation frequency where the maximum velocity amplitude was obtained as the natural frequency ω_i at V_{DC_i}. The bias voltage was then increased and this process was repeated sequentially to obtain the curve shown in Fig. 2.7.

We used the initial estimates of the beam thickness $\tilde{h}$ and capacitor gap $\tilde{d}$ in the

model, Eq. (2.51), to calculate ω_n as a function of $V_{\rm DC}$. The curve representing this function was then compared to the experimentally obtained curve and the values of $\tilde{h}$ and $\tilde{d}$ were updated iteratively until the difference between the experimentally obtained and numerically predicted curves fell within a predefined tolerance, Fig. 2.7. At this point, the values of $\tilde{h}$ and $\tilde{d}$, shown in Table 2.1, were adopted as refined estimates of the beam thickness h and capacitor gap d.

To summarize the previous results, we list in Table 2.1 the dimensions of the beam and the underlying fixed electrode measured using the white light profilometer in addition to the other estimated parameters.

Table 2.1: *Switch properties and dimensions.*

L (μm)	b (μm)	h (μm)	d (μm)	E (GPa)	ρ (kg/m^3)	σ (MPa)
225	20	1.7	1.7	80	19320	17

2.2.3 Damping estimation

The quality factor Q of the switch is the ratio of the energy stored in the bridge to the energy lost in one cycle of oscillation. The quality factor can be estimated experimentally from the frequency-response curve as the ratio of the resonance frequency f_r to the bandwidth at half-power level [68]; that is

$$Q = \frac{f_r}{\Delta f} \tag{2.53}$$

Figure 2.8 shows the experimentally obtained frequency-response curve for the waveform ($V_{\rm DC}$ = 10, $V_{\rm AC}$ = 17) V. The curve was obtained by sweeping the excitation frequency from 75 to 130 kHz in small discrete steps. The velocity of the bridge midpoint was measured using the laser vibrometer after the transient part of the response due to frequency shift had decayed. The FFT was obtained with the midpoint velocity averaged over 30 periods of the excitation frequency. The root-mean square of the velocity $V_{\rm RMS}$ was obtained from the peak in the FFT at the excitation frequency Ω. We calculated the quality factor from this figure using

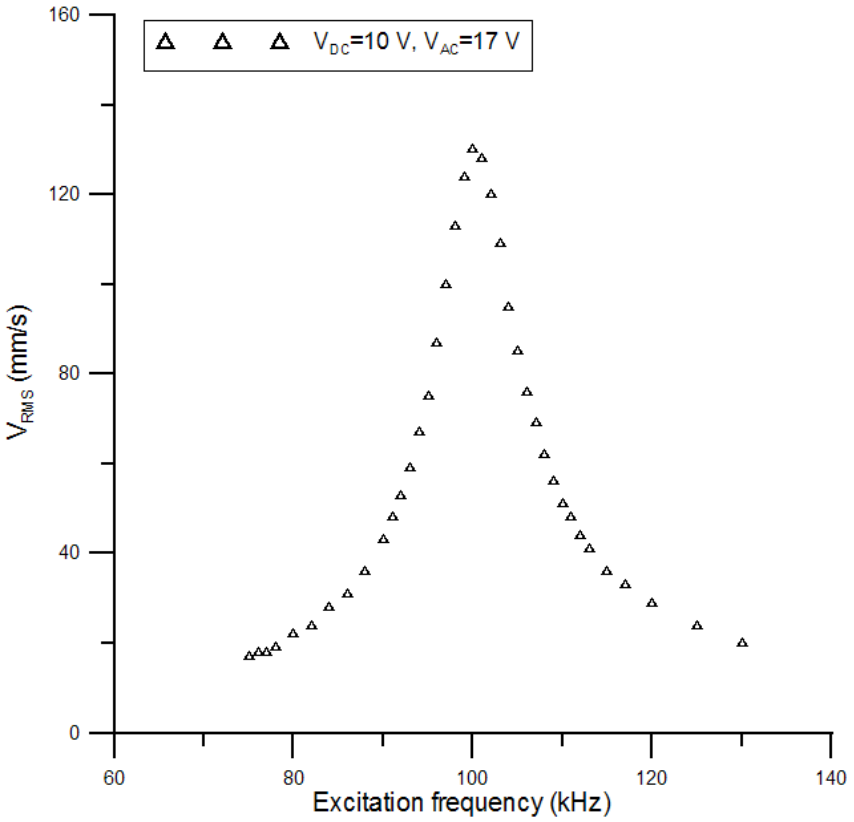

Figure 2.8: *Experimental frequency-response curve for the RMS velocity of the beam midpoint at ($V_{\mathrm{DC}} = 10$, $V_{\mathrm{AC}} = 17$) V.*

Eq. (2.53) as $Q = 12.5$ which quantifies the overall damping in the system.

We first assume the dominance of a linear dissipation mechanism lumping all dissipation mechanisms into an equivalent viscous damping. The predicted response under this assumption matches well the experimentally measured frequency-response curve for the waveform ($V_{\mathrm{DC}} = 50$, $V_{\mathrm{AC}} = 6.5$) V for small motions (around $V_{\mathrm{RMS}} = 100$ mm/s), Fig. 2.9, however it overestimates the response as its amplitude grows near resonance. This is the domain of large motions where the nonlinear dissipation mechanism of squeeze-film damping becomes significant.

We used the model in Eqs. (2.37) and (2.38) to account for the linear and nonlinear dissipation mechanisms. The frequency-response curve of the midpoint velocity was obtained numerically by applying the shooting method [5] to a three-mode reduced-order model of the switch [8]. We iteratively estimated the viscous damping coefficient c by matching the numerically obtained frequency-response

curve to the experimental curve shown in Fig. 2.9; they are in good agreement for all motions. The quality factor due to the linear dissipation mechanisms was calculated from the converged value of c and the formula [68]

$$Q_v = \frac{\omega_n}{c} \tag{2.54}$$

as $Q_v = 250$.

We can also obtain an estimate of the quality factor due to squeeze-film damping valid only for the excitation waveform ($V_{\mathrm{DC}} = 10$, $V_{\mathrm{AC}} = 17$) V by observing that the overall quality factor Q derived from the frequency-response curve in Fig. 2.8 combines the effects of the viscous Q_v and squeeze-film Q_s quality factors according to

$$\frac{1}{Q} = \frac{1}{Q_v} + \frac{1}{Q_s} \tag{2.55}$$

Therefore, the quality factor due to squeeze-film damping at this excitation level can be calculated using the formula

$$Q_s = \frac{Q_v\, Q}{Q_v - Q} \tag{2.56}$$

as $Q_s = 13$. Comparing the values of Q_v and Q_s to the overall quality factor $Q = 12.5$, we conclude that for moderate and large motions, squeeze-film damping is dominant for the switch under study. It is worth noting that packaging the switch in vacuum would eliminate the effects of squeeze-film damping.

2.3 Experimental Results

The switch was actuated by a biased AC voltage. To trigger dynamic pull-in [8, 69], we set the bias voltage to a fixed value V_{DC} and restrict the frequency of excitation to the neighborhood of the fundamental natural frequency ω_n of the switch measured in Section 3. Two procedures were used to induce dynamic pull-in:

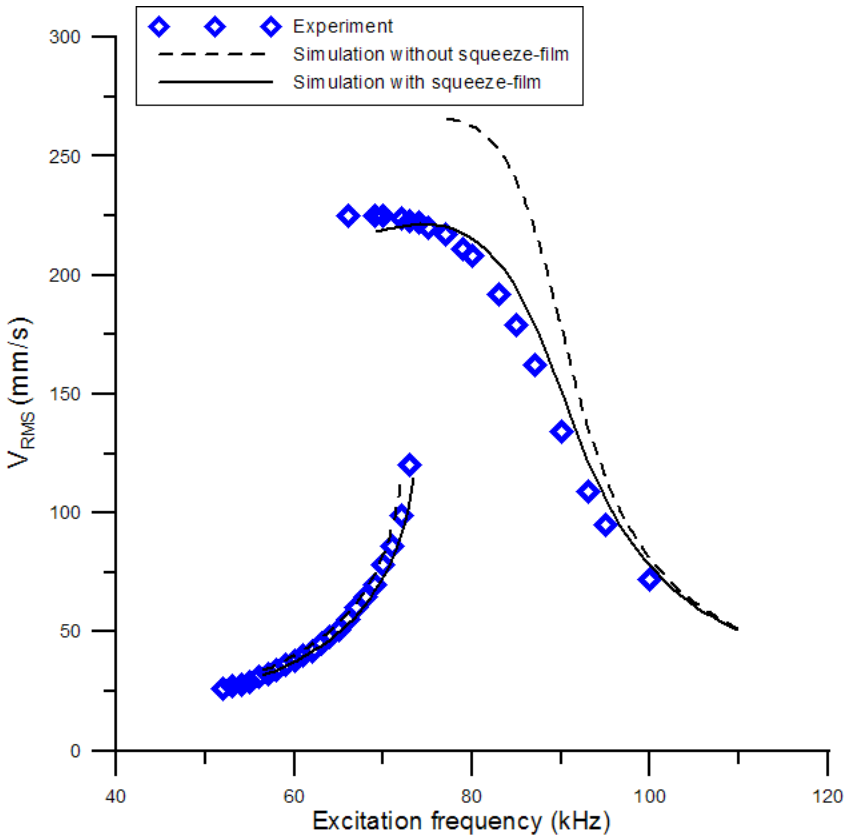

Figure 2.9: *The frequency-response curve of the bridge midpoint RMS velocity at* $V_{\mathrm{DC}} = 50$ *V and* $V_{\mathrm{AC}} = 6.5$ *V obtained experimentally (diamonds) and analytically with (solid lines) and without squeeze-film damping (dashed lines).*

(1) *A force sweep* in which the frequency of excitation was held at $\Omega = \omega_n$, while the amplitude V_{AC} was increased until dynamic pull-in occurred. This method is similar to that used by Fargas-Marques *et al.* [38].

(2) *A frequency sweep* in which V_{AC} was held constant, while the excitation frequency was swept up and down in the neighborhood of ω_n using the experimental procedure described in Section 2.2.2. The value of V_{AC} was then increased in small steps and the frequency sweeps were repeated until pull-in occurred.

Pull-in was detected as a sudden drop in the measured RMS velocity to the noise floor.

The effective nonlinearity of the switch is composed of a hardening component due to midplane stretching in the bridge and a softening component due to the electrostatic field. The effective nonlinearity changes character from a positive (hardening) nonlinearity at low DC voltage to a negative and increasingly softening nonlinearity as the DC voltage increases. As the effective nonlinearity increases, regions of multivaluedness appear and expand in the frequency-response curves, as shown in Fig. 2.10. As a result, the experimentally realizable part of the frequency-response curve is broken into left and right branches. A forward frequency sweep was used to obtain the left branch of the curve, while a backward frequency sweep was used to obtain the right branch of the curve.

Figure 2.10(a) shows the frequency-response curves obtained experimentally (diamonds) for ($V_{\mathrm{DC}} = 20, V_{\mathrm{AC}} = 27.5$) V and numerically (solid lines) for ($V_{\mathrm{DC}} = 24.5, V_{\mathrm{AC}} = 26.5$) V. Figure 2.10(b) shows the experimental frequency-response curve (diamonds) for ($V_{\mathrm{DC}} = 50, V_{\mathrm{AC}} = 6.5$) V and the corresponding numerical curve obtained for ($V_{\mathrm{DC}} = 56, V_{\mathrm{AC}} = 5.8$) V. The discrepancy between the experiment and simulation excitation levels is due to dielectric charging and divergence of the electrostatic field due to the doubly-curved configuration of the bridge under study, Fig. 2.6, from the parallel-plate assumptions. Dielectric charging, due to charge trapping in the silicon nitride insulation layer, increases the effective bias voltage across the bridge [26].

All of the frequency-response curves shown in Fig. 2.10 are bent to the left, indicating an effective softening nonlinearity. In each case, we found that dynamic pull-in occurred in backward sweeps beyond the peak point of the curve.

Two excitation conditions are examined in Fig. 2.10:

(1) low bias voltage and high AC voltage, Fig. 2.10(a)

(2) high bias voltage and low AC voltage, Fig. 2.10(b)

The velocity of beam oscillations is significantly larger under condition (1) than it is under condition (2) for the same excitation frequency. At low DC voltage, the stable equilibrium is away from the equilibrium saddle, resulting in a larger basin of

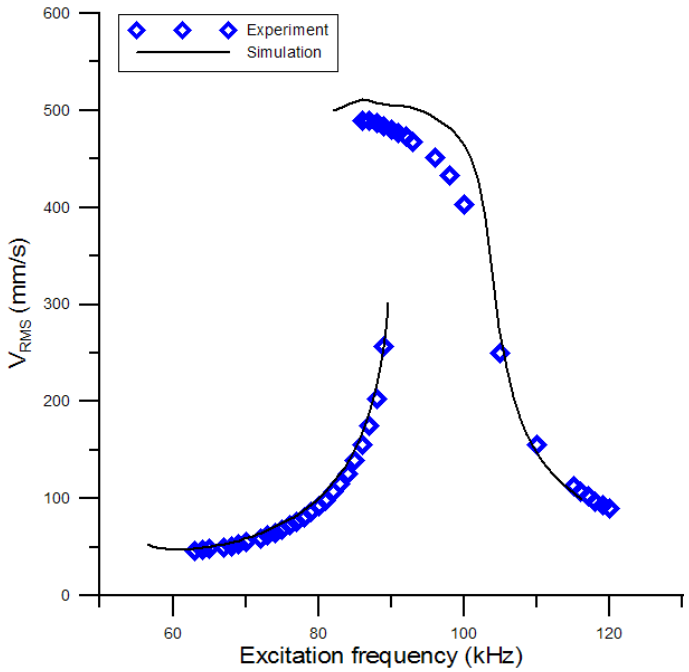

(a)

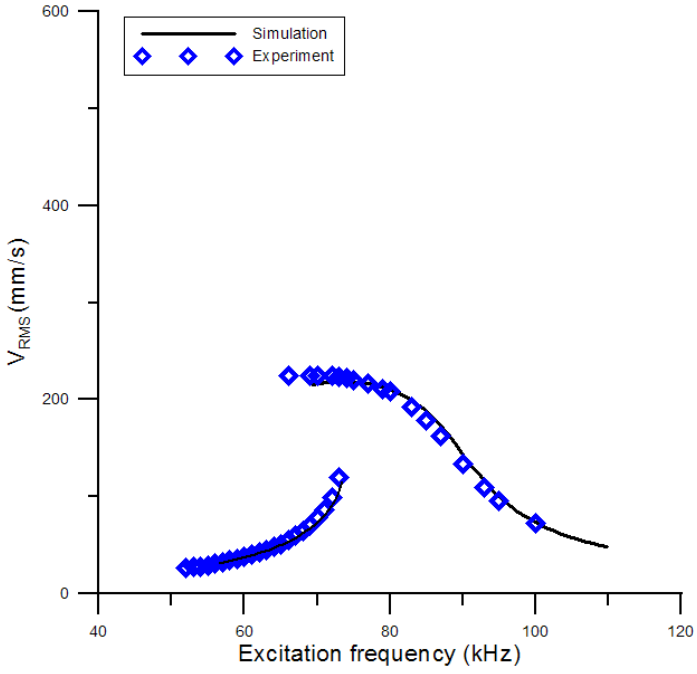

(b)

Figure 2.10: *The frequency-response curves of the midpoint RMS velocity for (a) low bias voltage and high AC voltage ($V_{DC} = 20$, $V_{AC} = 26.5$) V and (b) high bias voltage and low AC voltage ($V_{DC} = 50$, $V_{AC} = 6.5$) V.*

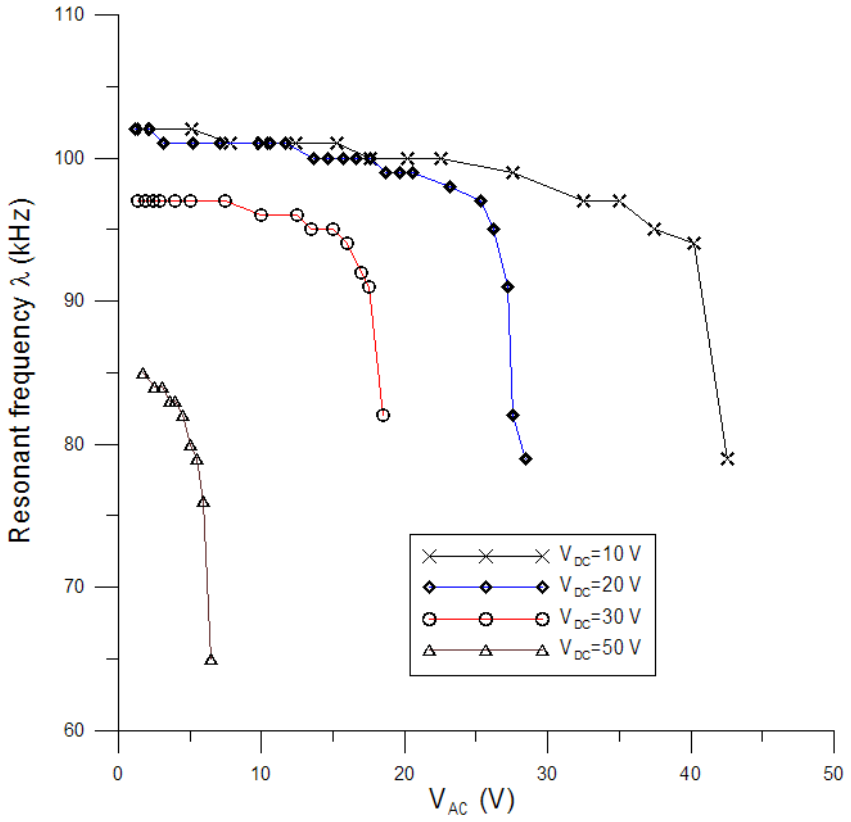

Figure 2.11: *The nonlinear resonance frequency ω_{nr} as a function of the amplitude of AC voltage V_{AC} for different bias voltages V_{DC}.*

attraction, and thereby larger orbits and higher velocities, than those available at high DC voltage [69]. As a result, the orbits of beam oscillation have more room to grow with AC voltage under condition (1) than they do under condition (2) before touching the stable manifold of the saddle which precipitates pull-in.

Holding the bias voltage V_{DC}, and therefore the effective nonlinearity, constant while increasing the AC voltage V_{AC} extends the softening frequency-response curves further to the left. Therefore, the peak of the frequency-response curve, the nonlinear resonance frequency ω_{nr}, is a function of V_{AC}. Figure 2.11 shows the $\omega_{nr} - V_{\mathrm{AC}}$ curves for different bias voltages V_{DC}. The lowest point in each curve indicates the largest experimentally realizable frequency-response curve before dynamic pull-in interrupts the backward sweep.

It can be seen from Fig. 2.11 that the AC voltage at which the backward sweep was interrupted is counter proportional to the magnitude of the bias voltage V_{DC}.

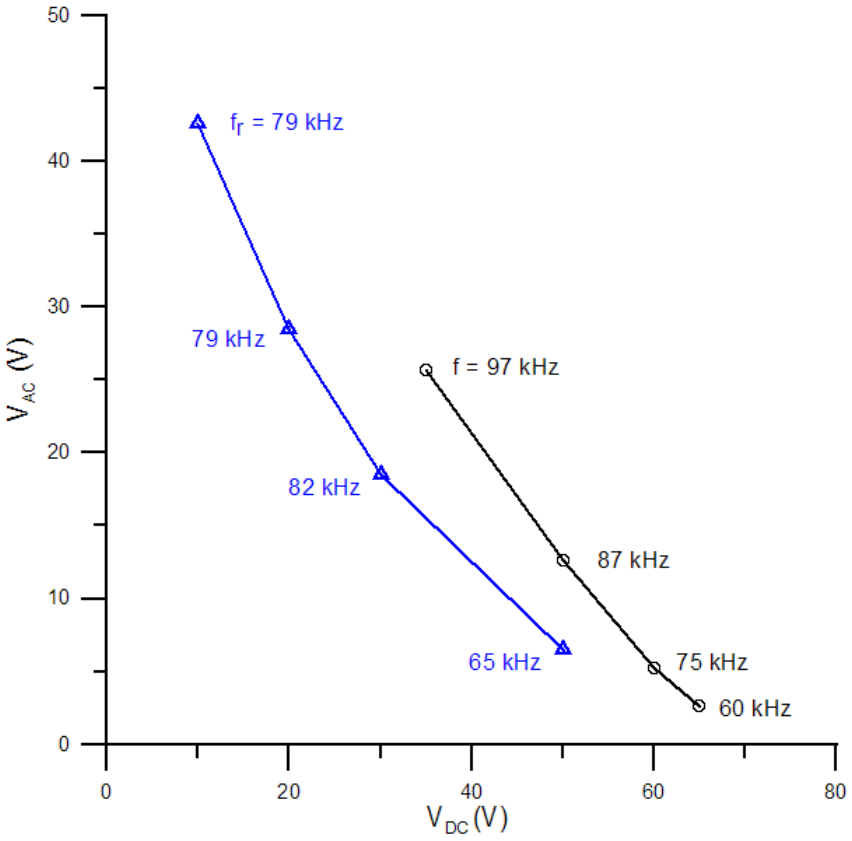

Figure 2.12: *Combinations of V_{DC} and V_{AC} required for dynamic pull-in for procedure 1 (circles) and procedure 2 (triangles).*

In fact, various combinations of V_{AC} and V_{DC} can be used to induce dynamic pull-in in a backward frequency sweep (procedure 2) and in a force sweep (procedure 1). Figure 2.12 shows the combinations of V_{DC} and V_{AC} at the onset of dynamic pull-in under procedures 1 and 2. The figure shows that a smaller AC amplitude can induce dynamic pull-in at the nonlinear resonance frequency, procedure 2, than is required at the fundamental natural frequency, procedure 1.

We define a figure of merit FoM to quantify the efficiency of various actuation methods used to induce pull-in compared to static actuation as

$$FoM = \frac{V_{\mathrm{SP}} - V_{\mathrm{DP}}}{V_{\mathrm{SP}}} \times 100 \tag{2.57}$$

where $V_{\mathrm{DP}} = \sqrt{V_{\mathrm{DC}}^2 + \frac{1}{2}V_{\mathrm{AC}}^2}$. Figure 2.13 compares the efficiency of dynamic actuation procedures 1 (circles) and 2 (triangles). The static pull-in of the switch under

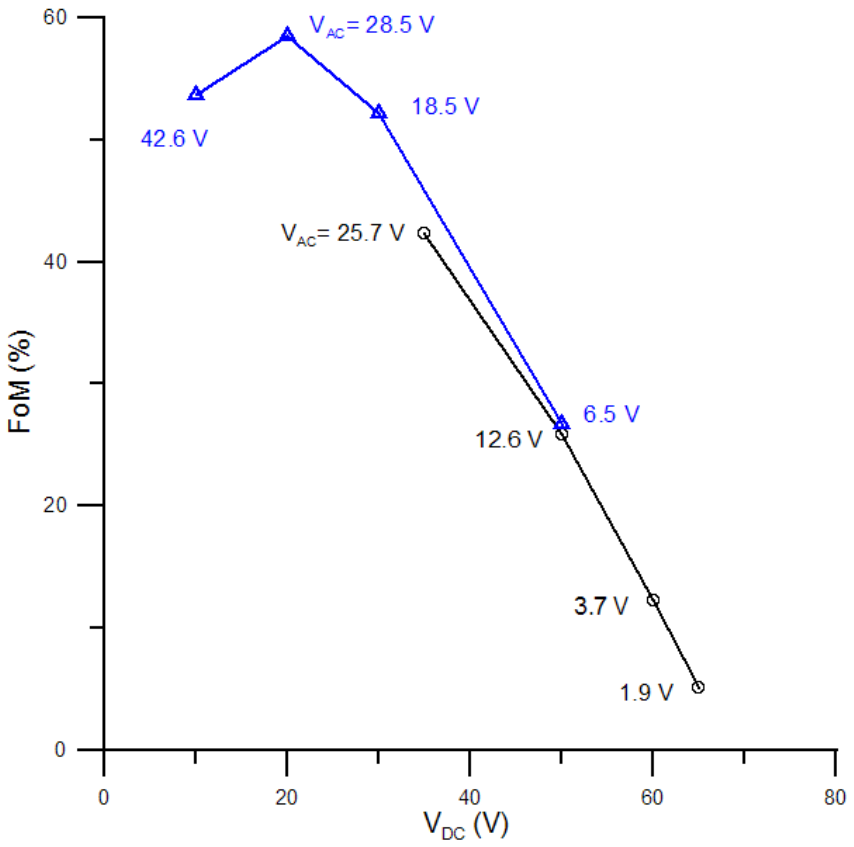

Figure 2.13: *The figure of merit FoM representing the efficiency of dynamic actuation procedures 1 (circles) and 2 (triangles) compared to static actuation.*

study is $V_{\mathrm{SP}} = 68.5$ V. Both procedures are superior to static actuation. This advantage increases as the bias voltage V_{DC} decreases, thereby opening more space for dynamic actuation procedures to take advantage of the dynamic amplification available at resonance. Further, procedure 2 outperforms procedure 1 for low bias voltages V_{DC} and yields 58.5 % voltage savings at $V_{\mathrm{DC}} = 20$ V compared to static actuation.

2.4 Switching Methods

In this section, we propose two methods to realize dynamic actuation. These methods are designed to avoid the requirements imposed by using a force sweep or a frequency sweep as a dynamic switching method. Instead, these methods use either a fixed excitation frequency or a single shift of the excitation frequency.

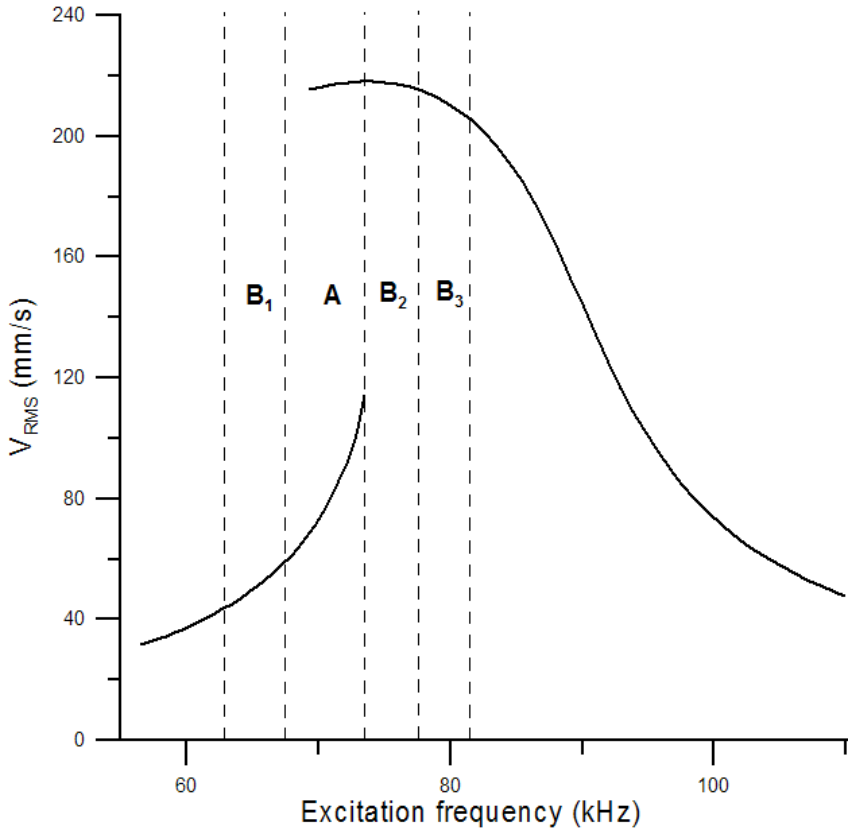

Figure 2.14: *Frequency-response curve for (V_{DC} = 56, V_{AC} = 5.8) V, showing touch-down regions for different switching methods. Region A represents the fixed-frequency switching while regions $B_1, B_2,$ andB_3 represent the shifted-frequency switching.*

We also calculate the switching time of the fixed-frequency and shifted-frequency actuation methods in order to compare their performance. We define the switching time as the time the bridge takes to move from an elevated steady-state position (ON-state) until the midpoint touches the transmission line (OFF-state). A shunt switch is normally ON; that is, the RF signal can be transmitted through the signal line when the bridge lies unactuated at rest. When the actuation waveform is applied, the beam closes the air gap and provides a low impedance path for the RF signal to be shunted to ground. This is considered the OFF-state of the switch. The switching time is a critical performance parameter for RF switches.

In the fixed-frequency switching method, we excite the bridge with a fixed frequency starting from rest. In a narrow frequency range in the neighborhood of the

resonance frequency, this method triggers touch-down. We found numerically that, for a waveform defined by ($V_{\mathrm{DC}} = 56$, $V_{\mathrm{AC}} = 5.8$) V, switching can be achieved using this method in the frequency interval $A = [68.75, 75.97]$ kHz in Fig. 2.14. The switching time decreases as the excitation frequency approaches the cyclic-fold bifurcation point. A phase portrait of the bridge response at an excitation frequency of $\Omega = 70.6$ kHz is shown in Fig. 2.15. The figure shows in blue dashed lines the homoclinic orbit of the saddle in the absence of the forcing and damping. It represents the stable and unstable manifolds of the saddle intersecting non-transversally away from the saddle [5]. In the presence of the forcing and damping, the homoclinic orbit is destroyed. Starting at rest, the midpoint describes larger orbits as it oscillates under the influence of the waveform. Although small and large stable periodic orbits are available for most of this frequency interval, as shown in Fig. 2.14, the transient response of the bridge is interrupted before it settles on either orbit when it intersects the stable manifold of the saddle. The orbit, then, follows the stable manifold to approach the saddle and is propelled to pull-in. The switching time in this case was calculated to be 62 μs. This relatively high switching time is due to the high damping in the switch ($Q = 12.5$). It results in the bridge spending significant time as the response amplitude grows slowly over multiple excitation periods until it intersects the stable manifold of the saddle. The maximal switching times for this switching method, found at the edges of the frequency interval A, were calculated as 114 μs at $\Omega = 68.75$ kHz and 91 μs at $\Omega = 75.97$ kHz. This is comparatively larger than the pull-in time calculated under pure static actuation, 7.7 μs at the static pull-in voltage $V_{\mathrm{DC}} = 68.5$ V.

The switching times throughout this subinterval are too long for RF applications. It can be reduced by redesigning the switch to decrease the overall damping. One method to achieve this goal is to reduce the effect of squeeze-film damping, the dominant damping source, by reducing the bridge width or the ambient pressure through encapsulation and partial air evacuation. It is also possible to minimize the effect of squeeze-film damping by adding holes to the structure of the bridge [70]. Therefore, it is feasible to manage the overall damping of the bridge in order to

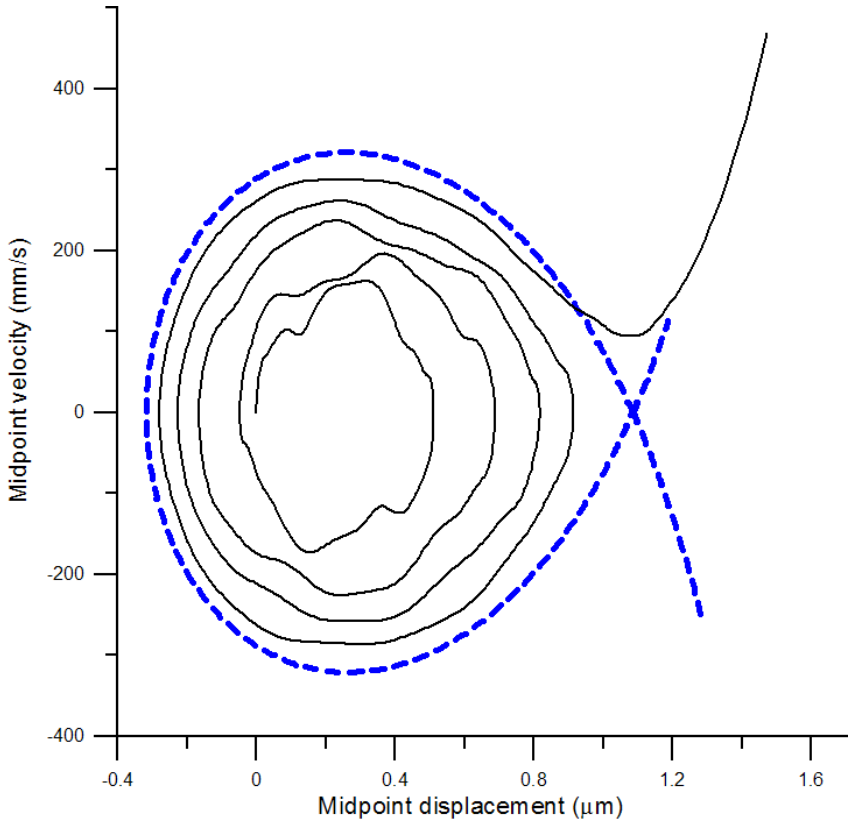

Figure 2.15: *The phase portrait of fixed-frequency switching for* ($V_{\mathrm{DC}} = 56$, $V_{\mathrm{AC}} = 5.8$) *V and* $\Omega = 70.6$ *kHz. The blue dashed lines depict the homoclinic orbit.*

minimize the switching time.

We calculated the switching time as the damping coefficient was reduced from μ_e to $R\mu_e$ for a common excitation frequency of $\Omega = 69$ kHz and the waveform ($V_{\mathrm{DC}} = 56$, $V_{\mathrm{AC}} = 5.8$) V. Table 2.2 shows that the switching time is reduced from 91 μs down to 31 μ as the damping coefficient μ_e is reduced by 30 %. It should be noted that the switching time decreases in discrete steps as the damping reduction decreases the number of excitation periods required for the peak bridge response to reach a size similar to that of the homoclinc orbit. Moreover, reducing the damping coefficient would have an extra advantage of reducing the dynamic pull-in voltage.

Table 2.2: *Switching time for the waveform* ($V_{\mathrm{DC}} = 56$, $V_{\mathrm{AC}} = 5.8$) *V and* $\Omega = 69$ *kHz as a function of the squeeze-film damping reduction ratio R.*

R	1	0.9	0.8	0.7
Switching time (μs)	91	61.5	46.7	30.8

In the shifted-frequency switching method, an excitation signal is introduced at a frequency in the neighborhood of the natural frequency and held for a set period of time $t_\circ$. This signal is not intended to cause pull-in and the only requirements placed on the voltage waveform ($V_{\rm DC}$, $V_{\rm AC}$) are that

- the corresponding frequency-response curve exhibits multivaluedness
- the initial and shifted frequencies belong to an interval B of the frequency spectrum.

The frequency of excitation is then shifted by $\delta\Omega$.

To demonstrate this switching method, we use the same waveform used for fixed-frequency switching ($V_{\rm DC} = 56$, $V_{\rm AC} = 5.8$) V and a frequency shift of $\delta\Omega = 0.1\Omega_\circ$. We found numerically that the interval B can be subdivided into three subintervals B_1, B_2, and B_3, Fig. 2.14, depending on the frequency shift direction. In the first subinterval, $B_1 = [63.7, 68.75]$ kHz, the only available stable responses lie on the lower branch of the frequency-response curve. An excitation frequency shift from $\Omega_\circ \in B_1$ to $\Omega_\circ + \delta\Omega$ triggers pull-in due to the fact that the frequency shift leads the system response to seek the larger stable orbits on the upper branch, thus approaching and intersecting the stable manifold of the saddle under the influence of the transient response. The phase portrait and time history for shifted-frequency switching starting from an initial excitation frequency $\Omega_\circ = 67.5$ kHz in the subinterval B_1 are shown in Fig. 2.16. The hold time was $t_\circ = 203$ μs and the switching time was calculated to be 59 μs. We note that the phase portrait depicts the relation between the nondimensional switch midpoint displacement w and the dimensional midpoint velocity $\dot{w}$ in mm/s; the velocity units are chosen in accordance with the experimental data.

In the second and third subintervals, $B_2 = [76, 79.7]$ kHz and $B_3 = [79.7, 84.1]$ kHz, the only available stable responses lie on the upper branch of the frequency-response curve. A shift-down from an initial excitation frequency in the subinterval B_3, $\Omega_\circ \in B_3$, triggers pull-in as the response wanders around its initial large orbit and ends up intersecting the stable manifold of the saddle under the influence

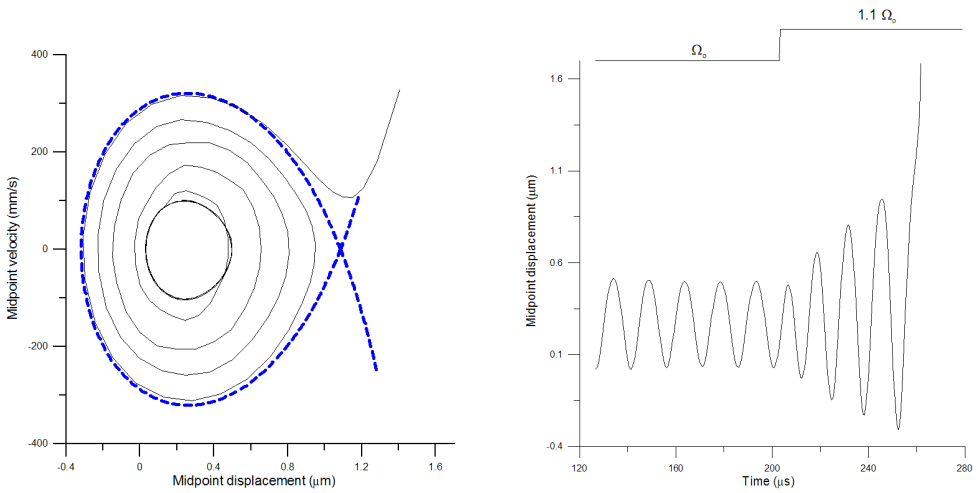

(a) (b)

Figure 2.16: *(a) The phase portrait and (b) time history of shifted-frequency switching for the waveform ($V_{DC} = 56$, $V_{AC} = 5.8$) V starting from an initial excitation frequency $\Omega_\circ = 67.5$ kHz in the subinterval B_1.*

of this transient behavior. The phase portrait and time history for the shifted-frequency switching starting from an initial excitation frequency $\Omega_\circ = 83.2$ kHz in the subinterval B_3 are shown in Fig. 2.17. The hold time was $t_\circ = 203$ μs and the switching time was calculated to be equal to 72 μs.

It follows from Figs. 2.16 and 2.17 that a significant fraction of the switching time is consumed as the response orbit wanders prior to intersecting the stable manifold of the saddle. This process is strongly influenced by the switch damping as was the case for fixed-frequency switching. Therefore, the switching time of shifted-frequency switching can also be reduced by reducing the damping.

For initial excitation frequencies in the subinterval B_2, $\Omega_\circ \in B_2$, we found that the frequency can be shifted up or down $\Omega_\circ \pm \delta\Omega$ to trigger pull-in. For example, using an initial excitation frequency $\Omega_\circ = 76.92$ kHz and a hold time of $t_\circ = 228$ μs, we obtained a switching time of 12.5 μs, as shown in Fig. 2.18. The switching time throughout this subinterval is the smallest compared to those obtained in the subintervals B_1 and B_3 and the interval A because the hold orbit in this case is the closest to the homoclinic orbit, which minimizes the time required for the transients

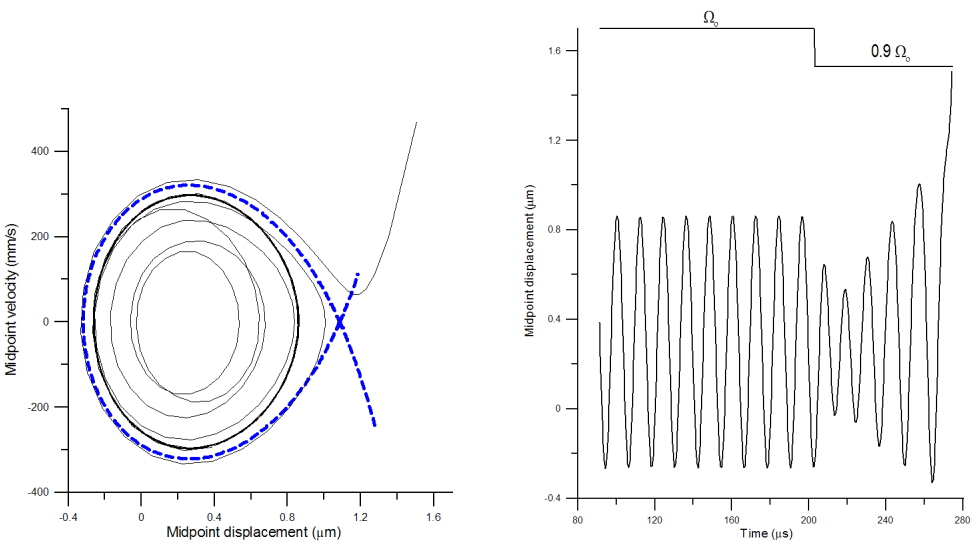

(a) (b)

Figure 2.17: *(a) The phase portrait and (b) time history of shifted-frequency switching for a waveform of ($V_{DC} = 56$, $V_{AC} = 5.8$) V starting from an initial excitation frequency $\Omega_\circ = 83.2$ kHz in subinterval B_3.*

to cause an intersection with the stable manifold of the saddle.

2.5 Dielectric Charging

We observed dielectric charging during our experiments. The high potential difference ($\sim$ 70 V) applied to the switch pads led to a buildup of trapped charges on the silicon nitride insulation layer protecting the CPW. The charge build up was particularly high subsequent to pull-in, in agreement with the finding of Yuan *et al.* [27]. We found that the voltage drop across the insulation layer was in the range of $1-2$ V before pull-in and increased to $5-10$ V after pull-in. The recombination time of these charges was very long extending to several days, in agreement with the experimental results reported by Goldsmith *et al.* [25].

We devised a method to measure the change in the potential difference across the switch due to dielectric charging. To this end, we note that the electrostatic

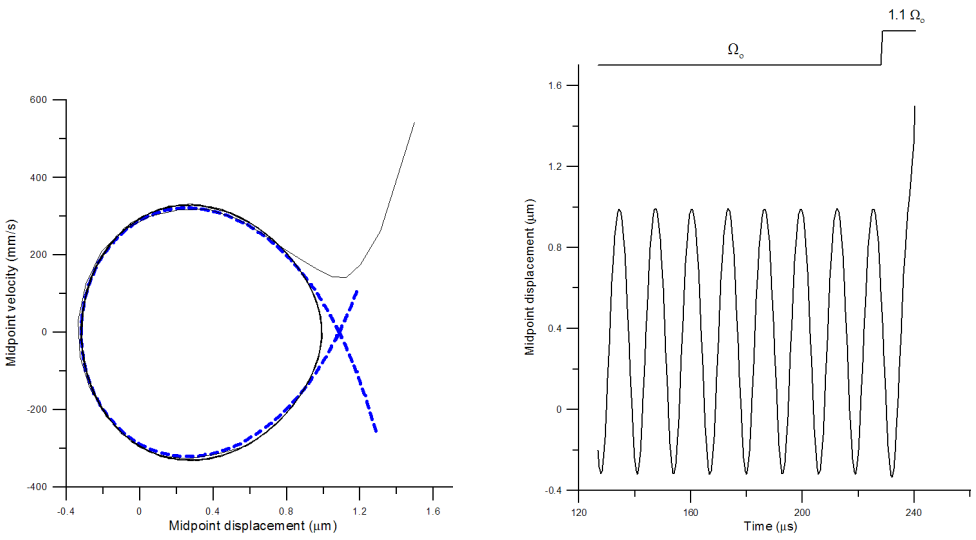

(a) (b)

Figure 2.18: *(a) Phase portrait at $V_{DC} = 56$ V and $V_{AC} = 5.8$ V starting from an orbit at $\Omega = 76.92$ kHz and (b) time history with the frequency step function shown.*

force F_e is proportional to the square of the applied voltage; that is,

$$\begin{aligned} F_e &\propto (V_{\mathrm{DC}} + V_{\mathrm{AC}} \cos(\Omega t))^2 \\ &\propto (V_{\mathrm{DC}}^2 + \frac{1}{2} V_{\mathrm{AC}}^2) + 2 V_{\mathrm{DC}} V_{\mathrm{AC}} \cos(\Omega t) - \frac{1}{2} V_{\mathrm{AC}}^2 \cos(2\Omega t) \end{aligned} \tag{2.58}$$

Therefore, the spectrum of the forced response of the bridge to a DC-AC waveform will exhibit peaks at Ω and 2Ω. On the other hand, the spectrum of the forced response to an AC signal will have a peak at 2Ω and no peak at Ω. In the presence of trapped charges on the insulator, an AC signal will produce a peak at Ω, proportional to the DC potential drop due to those charges, in addition to the peak at 2Ω.

We used this observation to measure the potential difference due to insulator charging across the bridge. We add an opposite polarity DC voltage to the AC signal and gradually increase the DC voltage until the peak at Ω disappears from the frequency spectrum, leaving only the peak at 2Ω. At this point, we take the opposite polarity DC voltage as an estimate of the voltage drop across the capacitor

due to the trapped charges on the insulation layer. This estimate is taken into account in matching the experimental results to the simulations.

Chapter 3

Binary Micro Gas Sensors

We propose two micro-mass sensing mechanisms based on the pull-in instability, namely static sensing and dynamic sensing. We use these mechanisms to design threshold mass sensors that operate by triggering pull-in once the mass absorbed by or adsorbed to a functional material exceeds a threshold value. These sensors are of particular value as safety sensors that can detect, for example, noxious gases in air or pollutants in water. We use these sense mechanisms to develop two classes of gas sensors: static and dynamic. We realize and validate a static threshold formaldehyde sensor. We discuss the sensor design considerations in addition to sensor model and introduce some preliminary experimental results. The mathematical model and numerical results for the sensor are summarized in [71].

3.1 Pull-in as a Sensing Mechanism

Most commercially available gas sensors provide continuous measurement of the concentration of a target analyte. The quantification of the analyte concentration is not relevant to most safety sensors, since the only information of interest here is whether the analyte, for example carbon monoxide, concentration is above or below the safety threshold. In a sense, these sensors are over-engineered for their purpose. Threshold sensors that seek merely to produce a binary output of 'true' or 'false' are more appropriate for this application. The fact that they do not

attempt to quantify the measured concentration reduces the requirements on the sensor electronics which can be translated into advantages in cost and robustness.

Pull-in is a binary process where the system response can only fall into a 'true' or 'false' category. We, therefore, seek to use pull-in to develop and realize threshold type gas sensors. The main concept of the proposed sensor is based on making use of the high sensitivity nature of electrostatically actuated sensors near pull-in. Tiny masses of gas molecules can drive the sensor under this state of actuation to pull-in. The sensor now operates in a binary on-state and off-state which is a discrete process.

For electrostatic actuation, there are two distinct regions of operation. Under low voltages, the resistance between the plate and the bottom electrode is infinite and the capacitance is finite. The displacement is also small at low voltages, 30 % of the gap in linear operation. At higher voltages exceeding the pull-in limit, the situation is reversed. Resistance decreases and capacitance increases significantly. The plate snaps down to the bottom electrode and the displacement is much larger than in the first case. This defines two distinct regions of operation for the sensor around the pull-in critical limit. The large difference in systems characteristics between the two regions allows for sensitive mass detection.

We are proposing two modes of sensing: static and dynamic. In static sensing, a cantilever is actuated under pure DC voltage near the static pull-in limit where the sensor sensitivity is high. Tiny masses of the target gas stick to the surface of the sensor driving it to pull-in. In the dynamic sensing mode, the sensor is actuated under a biased AC voltage near the dynamic pull-in limit. The frequency of the harmonic component of excitation due to AC voltage is tuned close to the resonant frequency of the switch for maximum sensitivity. Tiny masses of the target gas adsorbed to the surface of the sensor modify the natural frequency of the switch to lower values, thus driving the sensor to pull-in.

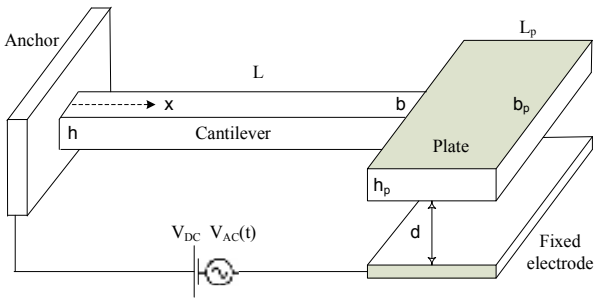

Figure 3.1: *Schematic of the gas sensor.*

3.2 Sensor Model

The gas sensor is composed of a micro cantilever beam attached to a micro plate at its free end, as shown in Fig. 3.1. To actuate the plate, an electrode is set under the plate at a distance d. We adopt the mathematical model developed by Nayfeh *et al.* [45] to study the sensor. The model treats the micro beam as an elastic continuum and the plate as a rigid body. The micro beam is modeled according to Euler-Bernoulli beam theory. The beam has the following characteristics: width b, thickness h, cross-sectional area A, and a moment of area I. The micro plate mass is $\hat{m}_p$ and its mass moment of inertia around the center of mass is $J_c = \frac{1}{3}\hat{m}_p\hat{L}_c^2$, where $\hat{L}_c$ is the distance from the beam end to the plate center.

The equation of motion of the micro beam-micro plate system is derived using Hamilton's principle which states that

$$\int_{t_1}^{t_2} (\delta T - \delta V + \delta W_{nc})\,\mathrm{dt} = 0 \tag{3.1}$$

The rotation angle of the plate is assumed to be equal to that of the micro beam tip $\hat{w}_{\hat{x}}(L,\hat{t})$. Hence, the total kinetic energy of the beam and the plate is given by

$$T = \frac{1}{2}\int_0^L \rho A\hat{w}_{\hat{t}}^2(\hat{x},\hat{t})d\hat{x} + \frac{1}{2}M\left[\hat{w}_{\hat{t}}(L,\hat{t}) + \hat{L}_c\hat{w}_{\hat{x}\hat{t}}(L,\hat{t})\right]^2 + \frac{1}{2}J\hat{w}_{\hat{x}\hat{t}}^2(L,\hat{t}) \tag{3.2}$$

where $\hat{w}(\hat{x},\hat{t})$ is the beam displacement at location $\hat{x}$ and time $\hat{t}$ and the subscripts $\hat{x}$ and $\hat{t}$ denote, respectively, the partial derivatives with respect to $\hat{x}$ and $\hat{t}$.

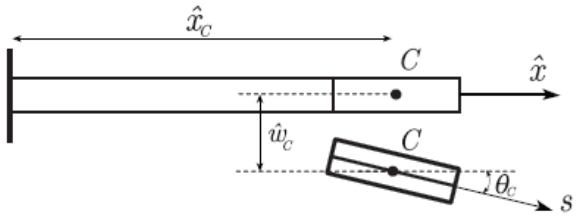

Figure 3.2: *Local coordinate system attached to the micro plate [45].*

The total potential energy V is the sum of the potential energy due to the micro beam elastic deformation

$$V_D = \frac{1}{2}\int_0^L EI\hat{w}_{\hat{x}\hat{x}}^2(\hat{x},\hat{t})d\hat{x}$$

and the potential energy due to the electrostatic field between the micro plate and electrode

$$\begin{aligned} V_E &= -\frac{\varepsilon b_p}{2}(V_{\rm DC}+V_{\rm AC})^2\int_0^{2\hat{L}_c}\frac{ds}{d-\hat{w}(L,\hat{t})-\hat{w}_{\hat{x}}(L,\hat{t})s} \\ &= \frac{\varepsilon b_p}{2\hat{w}_{\hat{x}}(L,\hat{t})}(V_{\rm DC}+V_{\rm AC})^2\ln\frac{d-\hat{w}(L,\hat{t})-2\hat{L}_c\hat{w}_{\hat{x}}(L,\hat{t})}{d-\hat{w}(L,\hat{t})} \end{aligned}$$

where ε is the permittivity of air, $V_{\rm DC}$ and $V_{\rm AC}$ are the DC and the AC voltage components applied between the electrode and the micro plate, and s is a local coordinate originated at the cantilever free end and attached to the micro plate as shown in Fig. 3.2. Applying Hamilton's principle and taking the plate weight into account, we obtain the equation of motion of the sensor in the form [45]

$$EI\hat{w}_{\hat{x}\hat{x}\hat{x}\hat{x}} + \hat{c}\,\hat{w}_{\hat{t}} + \rho A\hat{w}_{\hat{t}\hat{t}} = 0 \tag{3.3}$$

subject to the following boundary conditions:

$$\hat{w}(0,\hat{t}) = 0 \tag{3.4a}$$

$$\hat{w}_{\hat{x}}(0,\hat{t}) = 0 \tag{3.4b}$$

$$\begin{aligned} EI\hat{w}_{\hat{x}\hat{x}}(L,\hat{t}) &= \hat{m}_p g\hat{L}_c - \hat{m}_p\hat{L}_c\hat{w}_{\hat{t}\hat{t}}\left(L,\hat{t}\right) \\ &\quad - (\hat{m}_p\hat{L}_c^2 + J)\hat{w}_{\hat{x}\hat{t}\hat{t}}(L,\hat{t}) + \frac{\varepsilon b_p}{2(\hat{w}_{\hat{x}}(L,\hat{t}))^2}(V_{\mathrm{DC}} + V_{\mathrm{AC}})^2\times \\ &\quad \Big[\frac{2\hat{L}_c\hat{w}_{\hat{x}}(L,\hat{t})}{d - \hat{w}(L,\hat{t}) - 2\hat{L}_c\hat{w}_{\hat{x}}(L,\hat{t})} - \ln\Big(\frac{d - \hat{w}(L,\hat{t})}{d - \hat{w}(L,\hat{t}) - 2\hat{L}_c\hat{w}_{\hat{x}}(L,\hat{t})}\Big)\Big] \end{aligned} \tag{3.4c}$$

$$\begin{aligned} EI\hat{w}_{\hat{x}\hat{x}\hat{x}\hat{x}}(L,\hat{t}) &= \hat{m}_p\hat{w}_{\hat{t}\hat{t}}(L,\hat{t}) + \hat{m}_p\hat{L}_c\hat{w}_{\hat{x}\hat{t}\hat{t}}(L,\hat{t}) - \hat{m}_p g \\ &\quad - \frac{\varepsilon b_p}{2\hat{w}_{\hat{x}}(L,\hat{t})}\left(V_{\mathrm{DC}} + V_{\mathrm{AC}}\right)^2 \times \\ &\quad \Big[\frac{2\hat{L}_c\hat{w}_{\hat{x}}}{(d - \hat{w}(L,\hat{t}))(d - \hat{w}(L,\hat{t}) - 2\hat{L}_c\hat{w}_{\hat{x}}(L,\hat{t}))}\Big] \end{aligned} \tag{3.4d}$$

where $\hat{w}_{\hat{x}}$ is the displacement of the plate midpoint, $\hat{c}$ is the damping coefficient, and $\hat{m}_p$ is the plate mass.

For convenience, we introduce the nondimensional variables

$$w = \frac{\hat{w}}{d}, \qquad x = \frac{\hat{x}}{L}, \qquad t = \frac{\hat{t}}{T} \tag{3.5}$$

where T is a time scale. Substituting Eq. (3.5) into Eq. (3.3) and Eqs. (3.4a)–(3.4d), we obtain the nodimensional equation of motion in the form

$$w_{tt}(x,t) + c\, w_t(x,t) + w_{xxxx}(x,t) = 0 \tag{3.6}$$

subject to the boundary conditions

$$w(0,t) = 0 \tag{3.7a}$$

$$w_x(0,t) = 0 \tag{3.7b}$$

$$\begin{aligned} w_{xx}(1,t) = {} & M_p L_c - M L_c w_{tt}(1,t) - \frac{4}{3} M L_c^2 w_{xtt}(1,t) \\ & + \frac{\alpha (V_{\mathrm{DC}} + V_{\mathrm{AC}})^2}{w_x^2(1,t)} \times \\ & \Big[\frac{2 L_c w_x(1,t)}{1 - w(1,t) - 2 L_c w_x(1,t)} - \ln \frac{1 - w(1,t)}{1 - w(1,t) - 2 L_c w_x(1,t)} \Big] \end{aligned} \tag{3.7c}$$

$$\begin{aligned} w_{xxx}(1,t) = {} & -M_p + M w_{tt}(1,t) + M L_c w_{xtt}(1,t) \\ & - \frac{2\alpha (V_{\mathrm{DC}} + V_{\mathrm{AC}}(t))^2}{w_x(1,t)} \, \frac{L_c w_x(1,t)}{(1 - w(1,t))(1 - w(1,t) - 2 L_c w_x(1,t))} \end{aligned} \tag{3.7d}$$

where

$$\begin{gathered} \alpha = \frac{\varepsilon b_p L^4}{2 E I d^3}, \quad T = \sqrt{\frac{\rho A L^4}{E I}}, \quad c = \frac{\hat{c} L^4}{E I T}, \\ L_c = \frac{\hat{L}_c}{L}, \quad M = \frac{\hat{m}_p}{\rho A L}, \quad \text{and} \quad M_p = \frac{\hat{m}_p g L^3}{E I d} \end{gathered} \tag{3.8}$$

and M_p accounts for the effect of the sense-plate weight.

3.3 Static Sensor

The sensor concept is built around the distinction between two sensor states: before and after pull-in. When the sensor is actuated using a DC voltage close to but less than the pull-in voltage, a small mass added to the sense-plate would drive the sensor into pull-in. This mass sensor can then be configured as a gas sensor by depositing a functional material on top of the sense-plate. As the concentration of the target gas in air increases, the number of gas molecules captured by the functional material will increase. The captured gas molecules serve as 'added mass' and the DC voltage is set so that a gas concentration above the safety level will result in an added mass that will trigger pull-in. The difference between the sensor

resistance, capacitance, and/or impedance before and after pull-in can then be used as a metric to detect a gas concentration below or above the safety threshold.

3.3.1 Model

We develop a closed-form expression for the static deflection, denoted by $w_s(x)$, of the system under DC voltage excitation and estimate the maximum range of travel. The static problem can be formulated by setting the time derivatives and the AC forcing term in Eqs. (3.7a)-(3.7d) equal to zero which yields

$$w_s^{iv}(x) = 0 \tag{3.9}$$

subject to the boundary conditions

$$w_s(0) = 0 \tag{3.10a}$$

$$w_s'(0) = 0 \tag{3.10b}$$

$$w_s''(1) = M_p L_c + \frac{\alpha V_{\mathrm{DC}}^2}{w_s'(1)^2}\left[\frac{2L_c w_s'(1)}{1 - w_s(1) - 2L_c w_s'(1)} - \ln\Big(\frac{1 - w_s(1)}{1 - w_s(1) - 2L_c w_s'(1)}\Big)\right] \tag{3.10c}$$

$$w_s'''(1) = -M_p - \frac{2\alpha V_{\mathrm{DC}}^2}{w_s'(1)}\left[\frac{L_c w_s'(1)}{(1 - w_s(1))(1 - w_s(1) - 2L_c w_s'(1))}\right] \tag{3.10d}$$

where the primes denote derivatives with respect to x.

The general solution of Eq. (3.9) can be expressed as

$$w_s(x) = A\,x^3 + B\,x^2 + C\,x + D \tag{3.11}$$

Using the two boundary conditions in Eqs. (3.10a) and (3.10b) yields $C = D = 0$. The remaining boundary conditions result in the following nonlinear algebraic

equations:

$$\begin{aligned} 6A + 2B &= M_p L_c + \frac{\alpha V_{\mathrm{DC}}^2}{(3A+2B)^2} \\ &\quad \times \left[\frac{2L_c(3A+2B)}{1-A-B-2L_c(3A+2B)} - \ln \frac{1-A-B}{1-A-B-2L_c(3A+2B)} \right] \\ 6A &= -M_p - \frac{2\alpha V_{\mathrm{DC}}^2}{3A+2B} \left[\frac{L_c(3A+2B)}{(1-A-B)(1-A-B-2L_c(3A+2B))} \right] \end{aligned} \tag{3.12}$$

which can be numerically solved for A and B.

As a case study, we consider a micro sensor with the following geometric and material properties [45]:

- beam length $L = 250\,\mu$m, width $b = 5\,\mu$m, and thickness $h = 1.5\,\mu$m,
- plate length $L_p = 50\,\mu$m, width $b_p = 20\,\mu$m, and thickness $h_p = 1.5\,\mu$m,
- capacitor gap distance $d = 4\,\mu$m and air permittivity $\varepsilon = 8.854 \times 10^{-12}$ F/m, and
- the sensor structural material is polysilicon with $\rho = 2300$ Kg/m^3 and $E = 160$ GPa.

Figure 3.3 shows variation of the static deflection $w_s + L_c w_s'$ of the micro plate center of mass with the DC voltage drop across the capacitor. The lower branch of solutions (solid line) is stable, whereas the upper branch of solutions (dashed line) is unstable. The figure also shows the pull-in limit V_{pi} beyond which there is no equilibrium position for the system. This critical point occurs at $V_{\mathrm{pi}} = 8.3$ V and $w_s + L_c w_s' = 0.328$ of the initial capacitor gap.

The static sensor operates by setting the voltage across the capacitor to a DC value $V_\circ$ close to but below V_{pi}. The threshold added mass is the smallest mass required to load the sense-plate enough to trigger pull-in. The closer the set voltage $V_\circ$ is to V_{pi}, the smaller is the required added mass resulting in a higher sensitivity sensor.

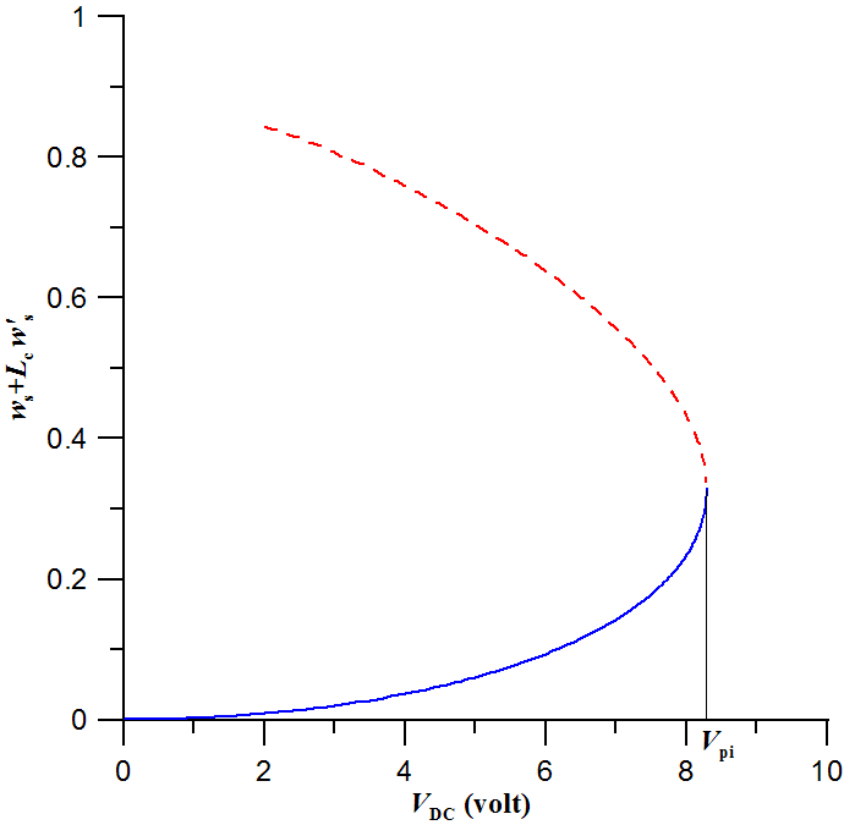

Figure 3.3: *Deflection of the plate center versus* V_{DC}.

3.3.2 Sensitivity analysis

In this section, we investigate sensitivity of static detection in an inertial electrostatic MEMS sensor to changes in the plate mass due to an absorbed/adsorbed mass. The sensitivity of the mass sensor is the ratio of the change in the static deflection of the plate δw to the change in mass δm

$$S_m = \frac{\delta w}{\delta m} \tag{3.13}$$

Therefore, the sensitivity of the static mass sensor is obtained by perturbing the plate mass to $M_p+\delta m$, evaluating the perturbed deflection $w_s+\delta w$, and substituting the result in Eq. (3.13). We note that w and M_p are normalized.

The static deflection of the center of mass of the plate takes the form

$$w = w_s(1) + L_c\, w_s'(1) \tag{3.14}$$

where

$$w_s(x) = Ax^3 + Bx^2 \tag{3.15}$$

Substituting Eq. (3.15) into Eq. (3.14), it simplifies to

$$w = (1 + 3L_c)\, A + (1 + 2L_c)\, B$$

Small changes in plate mass δm would result in changes in parameters A and B

$$\delta w = (1 + 3L_c)\, \delta A + (1 + 2L_c)\, \delta B \tag{3.16}$$

Substituting Eq. (3.16) into Eq. (3.13), we obtain

$$S_m = (1 + 3L_c)\, \frac{\delta A}{\delta m} + (1 + 2L_c)\, \frac{\delta B}{\delta m} \tag{3.17}$$

The perturbed terms in Eq. (3.17) are determined analytically in Appendix A. Using Eqs. (A.13) and (A.14) to substitute for the perturbed terms in Eq. (3.17), we obtain

$$\begin{aligned} S_m &= \frac{-2 - 12A\alpha V_{\mathrm{DC}}^2 \mathrm{L_c}^2 - 12\mathrm{B}\alpha \mathrm{V}_{\mathrm{DC}}^2 \mathrm{L_c}^2}{|C|} + \frac{12 + 12A\alpha V_{\mathrm{DC}}^2 \mathrm{L_c} + 12\mathrm{B}\alpha \mathrm{V}_{\mathrm{DC}}^2 \mathrm{L_c}}{|C|} \\ &\quad + 3L_c \frac{-2}{|C|} + 2L_c \frac{12 + 12A\alpha V_{\mathrm{DC}}^2 \mathrm{L_c} + 12\mathrm{B}\alpha \mathrm{V}_{\mathrm{DC}}^2 \mathrm{L_c}}{|C|} \\ &= \frac{10 + 18L_c + 12\alpha V_{\mathrm{DC}}^2 \mathrm{L_c}(\mathrm{A} + \mathrm{B}) + 12\alpha \mathrm{V}_{\mathrm{DC}}^2 \mathrm{L_c}^2(\mathrm{A} + \mathrm{B})}{|C|} \end{aligned} \tag{3.18}$$

where terms of order higher than $O(10^{-2})$ have been neglected and $|C|$ is defined in Eq. (A.7).

Equation (3.18) describes the sensitivity of cantilever beam-based deflection-

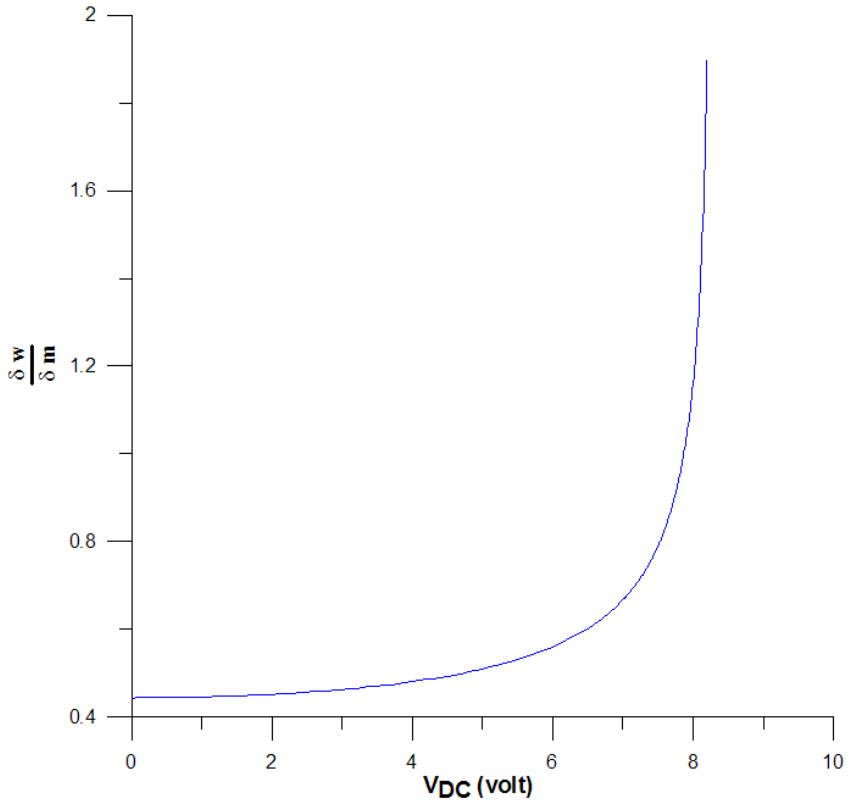

Figure 3.4: *Sensitivity versus static voltage* V_{DC}.

detected inertial mass sensors. This analytical formula indicates that increasing the ratio L_c of the sense-plate length L_p to the cantilever beam length L increases sensitivity, since it increases the moment arm of the sense-plate mass with respect to the cantilever beam end. Further, the equation indicates that the sensitivity is proportional to the strength of the electrostatic field as represented by the nondimensional potential difference αV_{DC}^2 and the effective capacitor gap $(1-w)$.

We used Eq. (3.17) to calculate the sensitivity of the case study sensor shown in Fig. 3.4 as a function the operating voltage V_{DC}. Our results show that sensitivity increases noticeably near the pull-in limit. This means that a small mass added to the plate is more detectable near pull-in than away from it. Therefore, it is advantageous to operate the sensor as close as possible to the pull-in limit. In fact, the sensitivity of the static version of the binary mass sensor represents the upper bound on the sensitivity of deflection-detected electrostatic MEMS mass sensors.

Figures 3.3 and 3.4 can be used to create a calibration table for the binary mass sensor. A threshold mass, minimum detectable mass, can be calculated by setting the DC voltage $V_\circ$ to a value near the pull-in limit. On the vertical axis of Fig. 3.3, we calculate δw_s as the difference between the deflection at pull-in and the deflection at $V_\circ$. Next, we find the sensitivity $S_{\rm m}$ of the sensor at the operating voltage $V_\circ$ from Fig. 3.4. Finally, we use Eq. (3.13) to find the threshold mass as δm.

The calibration table for the test case mass sensor is given in Table 3.1. Clearly, the sensor becomes more sensitive as the operating voltage $V_\circ$ approaches the pull-in limit, $V_{\rm pi} = 8.2935$ V. The minimum detectable mass is reduced more than 150 folds as the operating voltage is increased from $V_\circ = 8.0$ to 8.292 V. A minimum detectable mass of 3 nanograms, Table 3.1, can be sensed under a static voltage $V_{\rm DC} = 8.292$ V. It is worth noting here that 3 nanograms correspond to a sphere of radius equal to 9 μm. The sensor resolution depends on the regulator used to stabilize the voltage supply $V_\circ$ and external disturbances available in the environment.

Table 3.1: *The static binary mass sensor calibration table.*

Set voltage $V_\circ$ (V)	Threshold mass δm (ng)
6.000	2460
7.000	1637
8.000	481
8.100	331
8.200	170
8.250	82
8.270	46
8.290	7
8.292	3

3.3.3 Sensor design

The sensor is composed of a polysilicon cantilever with a plate at its free end. A polysilicon electrode is set under the plate to act as ground for the electrostatic field as shown in Fig. 3.5. The following design considerations were taken into account in building the sensor:

- A plate is added to the end of the cantilever to increase the surface area used to deposit the functional material and decrease the actuation voltage.

- The electrostatic field is applied only under the plate to reduce leakage current and simplify the analysis.

- The cantilever dimensions are small compared to the plate dimensions to reduce the sensor stiffness which would reduce the actuation voltage.

The prototypes were fabricated using the PolyMUMPs fabrication process. Figure 3.6 shows all the layers available in PolyMUMPs. The silicon nitride layer serves as insulation between the carrier wafer and the first polysilicon layer, Poly 0 used as a ground plane. The first silicon oxide layer is the first sacrificial layer between

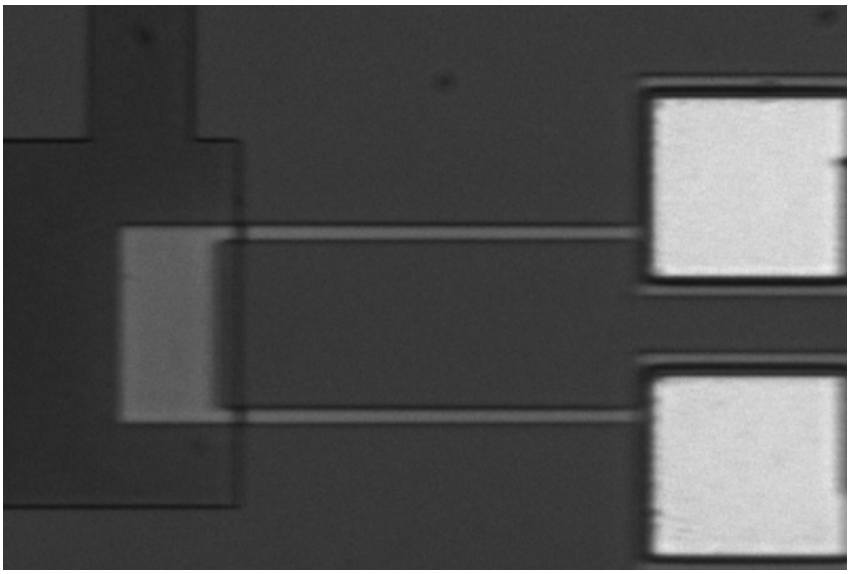

Figure 3.5: *Picture of the sensor under microscope.*

the substrate and second polysilicon layer, Poly 1. The second oxide layer is the second sacrificial layer between the second and third polysilicon layers, Poly 1 and Poly 2, respectively. The metal layer deposited on top of Poly 2 is 50 nm gold metalization layer [72].

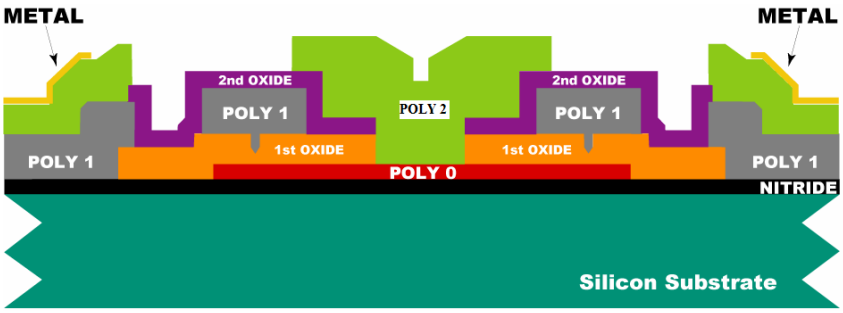

Figure 3.6: *Schematic of PolyMUMPs layers [72].*

A functional material with affinity to a target gas has to be deposited on top of the sense-plate to transform our mass sensing platform into a gas sensor. The gas then adheres to the functional material which increases the sense-plate mass. In this work, we develop a formaldehyde vapor sensor. Formaldehyde is a toxic volatile organic compound that pollutes indoor air. It can be inhaled or absorbed through the skin and eyes which has the potential to cause health problems [73].

The functional material used to realize the gas sensor is a specially doped polymer developed in a companion project to this effort [73]. In that work, it was experimentally found that Polyaniline (PANI) doped with nickel oxide (NiO) and aluminum oxide (Al_2O_3) provided the highest sensitivity and selectivity for formaldehyde at concentrations above 1 ppm [73].

PANI is a solid-state polymer. It is dissolved in an alcoholic base (ethylene glycol) to facilitate deposition of the polymer solution on top of the sense-plate surface. The concentration of PANI in the solution was increased, 0.0138 g of PANI was suspended in 15 mL of ethylene glycol, in order to increase its viscosity and reduce the number of drops required to deposit PANI on the sense-plate. Once the solution is exposed to air, ethylene glycol evaporates and polymer residue is left on the sense-plate.

Several techniques were devised to deposit the polymer solution to the sense-plate. Initially, we tried to inject drops of the solution on top of the sense-plate using a syringe and a micro tip needle. The minimum tip needle available commercially had an inner diameter of approximately 160 μm (30 gauge needle). This diameter is larger than the sense-plate dimensions. As a result, the injected droplets were large and overflowed the sense-plate surface resulting in stiction of the plate to the substrate once the solution dried out.

Another technique was to dip a micro probe inside the polymer solution and withdraw it with a micro drop that would attach to it as a result of contact forces between the solution and the probe. A specially designed probe was developed to obtain a probe tip smaller than the size of the sense-plate with surface properties that will promote adherence of the solution to the probe. The probe was made using a 500 μm fiber glass rod dry etched with hydrogen fluoride gas (HF) to reduce its diameter to about 30 μm. HF etching also roughened the probe surface enhancing the stiction forces between the solution and the probe glass surface. The probe was attached to a flexible copper probe fixed to a probe holder. This method proved successful in acquiring 30-40 μm diameter drops from the solution beaker. The probe holder was used to deposit the drops above the sense-plate, then approach and touch the sense-plate with the fiber glass probe. The probe was then withdrawn leaving the solution on top of the sense-plate.

3.3.3.1 First generation sensor

A schematic of the first generation prototypes is shown in Fig. 3.7. The sensors were made out of 10 μm wide cantilever beams with lengths of 100 μm and 125 μm. The sense-plate dimensions were set to 100×100 μm and 100×120 μm for all prototypes. The beams and plates were made out of the second polysilicon structural layer, Poly 2, with a thickness of 1.5 μm. Prototypes were fabricated with capacitor gaps of 0.75 μm and 2.75 μm using the second sacrificial layer and the first and second sacrificial layers, respectively.

Gold metalization lines were deposited on top of the sense-plate in order to

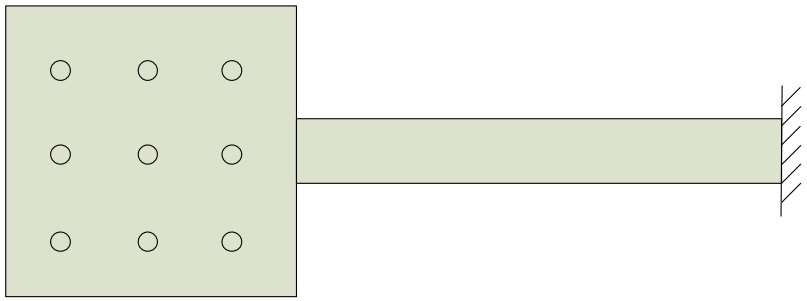

Figure 3.7: *Schematic of the first generation sensor.*

reset the sensor to 0-state after detection of formaldehyde. Application of a voltage difference between the two anchor pads at the end of the gold line loop pass a current through the line that heats the sense-plate through Joule heating. PANI is deposited on top of the gold lines and is known to release absorbed/adsorbed formaldehyde molecules upon heating to 100°C [73]. The gold lines were fabricated in zig-zag shape in order to increase heat generation and obtain a more uniform heat distribution over the sense-plate.

The fabrication yield of this generation was low because of design flaws. Many of the sensors showed evidence of sense-plate warping and stiction. Fabrication imperfections, which are always present, apply torsional moments to the support cantilever beam. The torsional stiffness of the support beam was low due to its small cross-sectional area compared to that of the plate. The large width of the plate amplify the torsional moment due to imbalance and means that even a small rotation angle will result in stiction of the plate to the substrate. Figure 3.8 shows a white light profilometer picture of a sensor failed due to warping and stiction of the plate to the substrate. This problem was so widespread that none of the 0.75 μm capacitor gap prototypes was functional.

Another drawback of this design was that residual stresses due to the difference in thermal conductivity between polysilicon and gold meant that sensors that did not fail due to stiction were bent-up as shown in Fig. 3.9. While these prototypes did not suffer functional failure, they demonstrated parametric degradation. Specifically, the elevated position of the sense-plate increased the pull-in voltage of

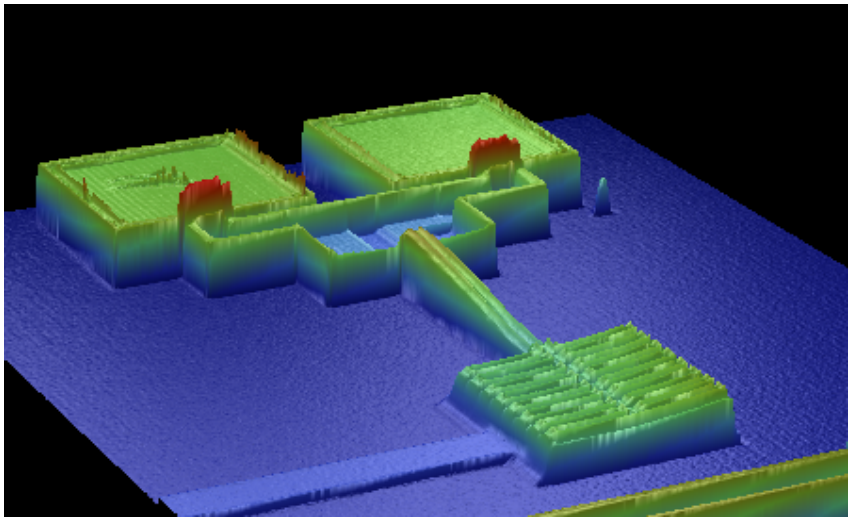

Figure 3.8: *White light profilometer picture showing warping and stiction of the sense-plate.*

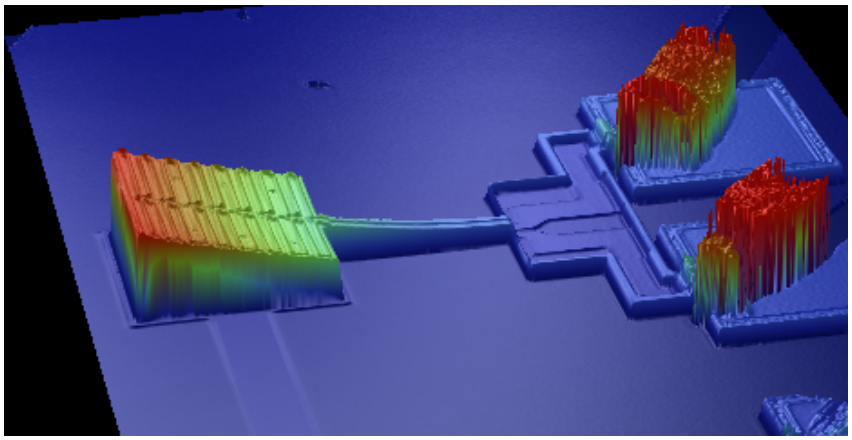

Figure 3.9: *White light profilometer picture showing a bent-up sensor.*

the prototypes from the a range 5-10 V to 15-30 V.

3.3.3.2 Second generation sensor

To overcome these problems, the design of the sensors were re-designed to maximize the torsional stiffness of the support beams. Second generation prototypes featured two cantilever beams instead of one. To maintain the same bending stiffness, the thickness of the beams was kept constant while their width (5 μm) was set equal to half of the first generation beam width. To increase the torsional stiffness, the beams were set as far apart from each other as possible in the width direction, thereby

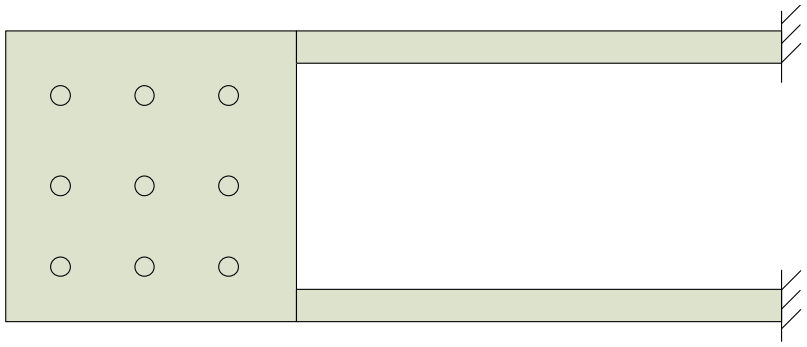

Figure 3.10: *A schematic of a second generation sensor.*

located at the edges of the sense-plate as shown in Fig. 3.10. The plate dimensions and capacitor gap were kept the same as those of the first generation sensors. The sensor redesign was successful in increasing the fabrication yield eliminating warping and stiction of the sensors. Figure 3.11 shows a successfully released second generation sensor.

However, upon polymer deposition the sense-plate invariably stuck to the bottom electrode once ethylene glycol evaporated. It appears that the reason for that was solution leakage through the etch hole and onto the substrate. We postulate that as ethylene glycol evaporated, the meniscus of fluid between the lower surface of the sense-plate and the substrate shrunk to bring the two surfaces into contact with the polymer acting as an adhesive between the two surfaces.

3.3.3.3 Third generation sensor

The third generation sensors kept the same design as that of the second generation but removed release holes. Since etch holes are necessary, per design rules, for successful release of structures with lateral dimensions larger than 30 μm, it was necessary to reduce the size of the sense-plate in order to eliminate etch holes. Therefore, the sense-plate dimensions were decreased to 30×30 μm and 30×60 μm.

We found that third generation sensors did not suffer stiction to the substrate during fabrication or after polymer deposition except in cases where the solution drops rolled over the side of the plate and onto the substrate. Figure 3.12 shows a picture of the sensor under microscope after polymer deposition. The polymer

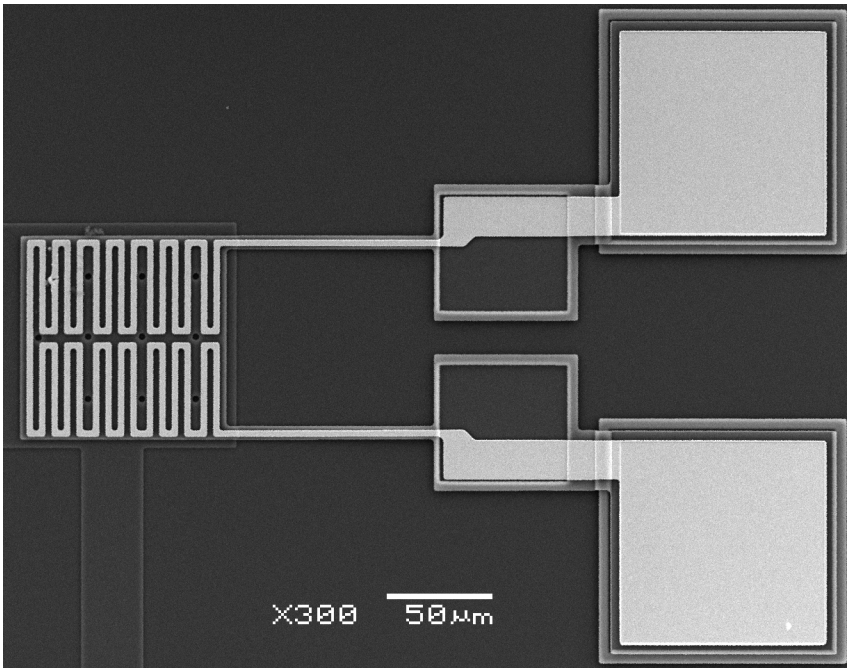

Figure 3.11: *SEM picture of a second generation sensor.*

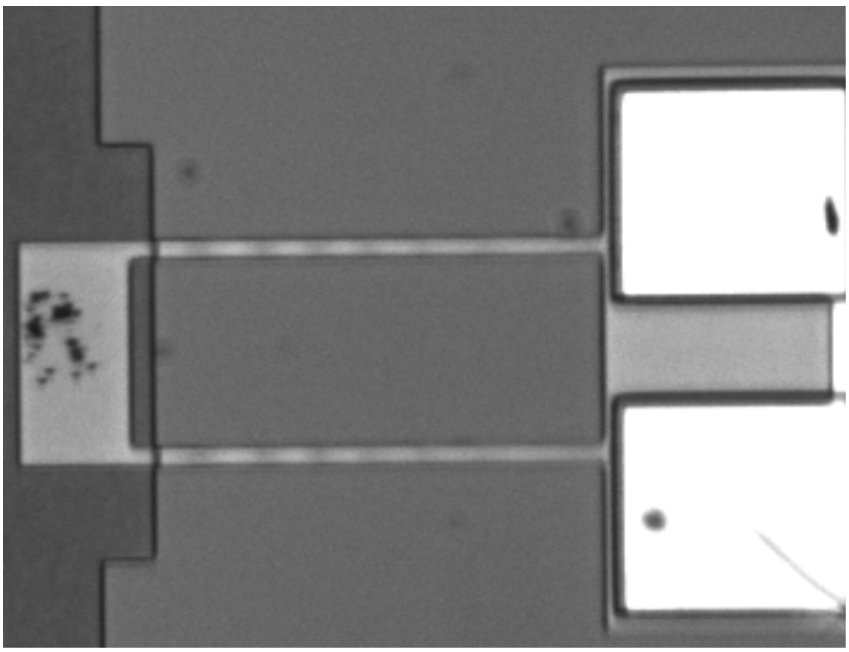

Figure 3.12: *Picture of a third-generation sensor after polymer deposition.*

seen as scattered black spots on the sense-plate is the residue of the deposition of one solution drop.

We also eliminated the gold metalization lines to avoid bending of the sensors

upward and achieve the targeted low actuation voltage. However, we maintained the gold pads at the roots of the two support beams so as to apply a voltage between them to drive a current through the semi-conductive polysilicon layer and heat the sense-plate through Joule heating to reset the sensor. It is worth noting that yield for this generation was more than 90 % of the released sensors.

3.3.4 Sensor realization

3.3.4.1 Driving circuit

Stabilizing the actuation voltage is necessary to reduce the noise floor of the sensor and approach the higher sensitivity zone of a few nano-grams indicated in Table 3.1. A low noise driving circuit was designed [74] in order to regulate the actuation voltage.

The low noise driving circuit consists of a USB-serial converter, a micro controller, a DAC (Digital-to-Analog Converter), a buffer, a non-inverting amplifier, a voltage reference, a negative bias generator, and a charge pump providing an actuation from 0 V to 10 V with a voltage error tolerance of 1 mV/V [75].

- The USB-to-Serial Converter provides a serial interface between PC and a micro controller through an USB interface and supplies 5 V unregulated power to the circuit board.

- The micro controller controls a DAC through SPI (Serial Peripheral Interface) based on user commands from PC.

- The DAC defines its output voltage from 0 V to 4.096 V with the resolution of 62.5 μV according to the command sent by a micro controller.

- The buffer provides a low impedance input to a non-inverting amplifier in order to minimize a loading effect.

- The non-inverting amplifier amplifies a input voltage with a gain of 3 to provide its output voltage from 0 V to 10 V.

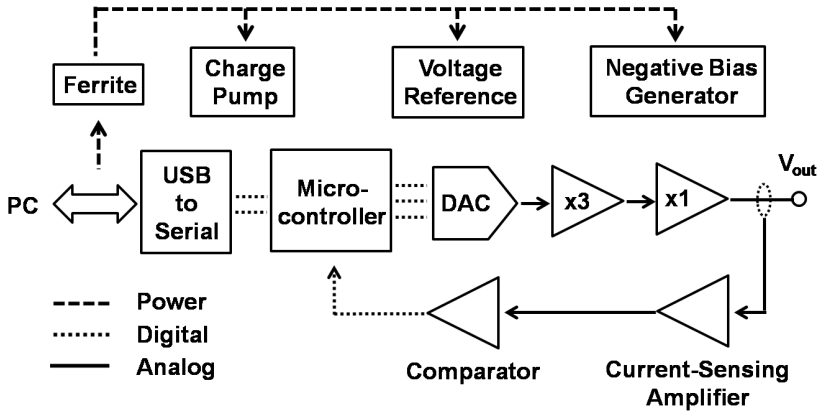

Figure 3.13: *Schematic of the sensor driving circuit and the contact detection circuit [74].*

- The voltage reference provides a low noise reference voltage of 4.096 V with low temperature drift.

- The negative bias generator supplies a negative power rail of -0.23 V so that a non-inverting amplifier can drive its output down to 0 V.

- The charge pump generates 12 V from 5 V unregulated voltage from the PC.

The contact detection circuit is composed of a current-sensing amplifier, and a comparator. When a gas sensor touches the underlying bottom electrode, this contact can be modeled as a resistance in a electrical circuit and sinks higher current than that before the contact. This increase in the current is measured by a current-sensing amplifier and is compared to the threshold value by a comparator with hysteresis. If the current is higher than the predetermined threshold value, a comparator drives its output to logic high, indicating that contact occurs [74]. A schematic of the low noise precision actuation circuit and the contact detection circuit is presented in Fig. 3.13.

3.3.4.2 Experimental technique

The laser vibrometer is used to measure the sensor response to the actuation signal supplied by the driving circuit. In order to determine the pull-in voltage, a triangular waveform was applied to the sensor. The low-frequency actuation ensures a

quasi-static response. The maximum voltage of the waveform was increased until pull-in was achieved. A screen capture of the laser vibrometer software interface is shown in Fig. 3.14. The figure shows the laser spot positioned over the sense-plate and the measured plate displacement as function of time.

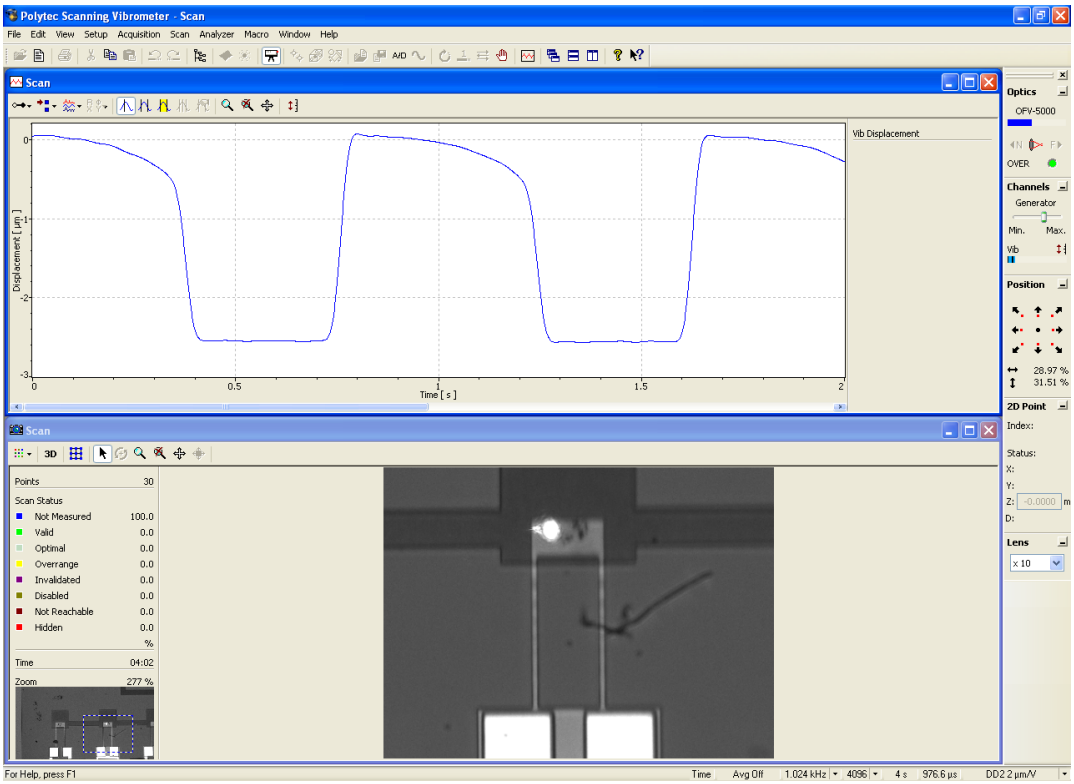

Figure 3.14: *A screen shot of the laser vibrometer interface showing pull-in and pull-out cycles.*

The figure shows the response to a triangular waveform with a maximum of 8.8 V and a period of 1 s. The sense-plate moves down towards the substrate as the voltage increases linearly. It pulls in at the maximum point of the waveform and continues to touch the substrate as the voltage drops until it approaches 0 V.

After several pull-in and pull-out cycles, we found that the waveform was no longer enough to trigger pull-in. The screen shot of the laser vibrometer interface software in Fig. 3.15 shows this process. While the sense-plate goes through pull-in and pull-out during the first cycle, it merely deflects downward and upward without pull-in during the second cycle. Upon increasing the amplitude of the waveform, we regained the same cyclic pattern of pull-in and pull-out. However, the same

drift process continues to occur after several cycles and disappears upon increasing the waveform amplitude again.

We postulate that this drift is a result of charge leakage into a dielectric layer on top of the substrate electrode. The exposure of polysilicon to air creates a thin film of dielectric silicon oxide over time [76]. Leaked charges captured in this layer reduce the effective voltage drop seen by the sensor capacitor. This effect is counteracted by increasing the amplitude of the actuation waveform.

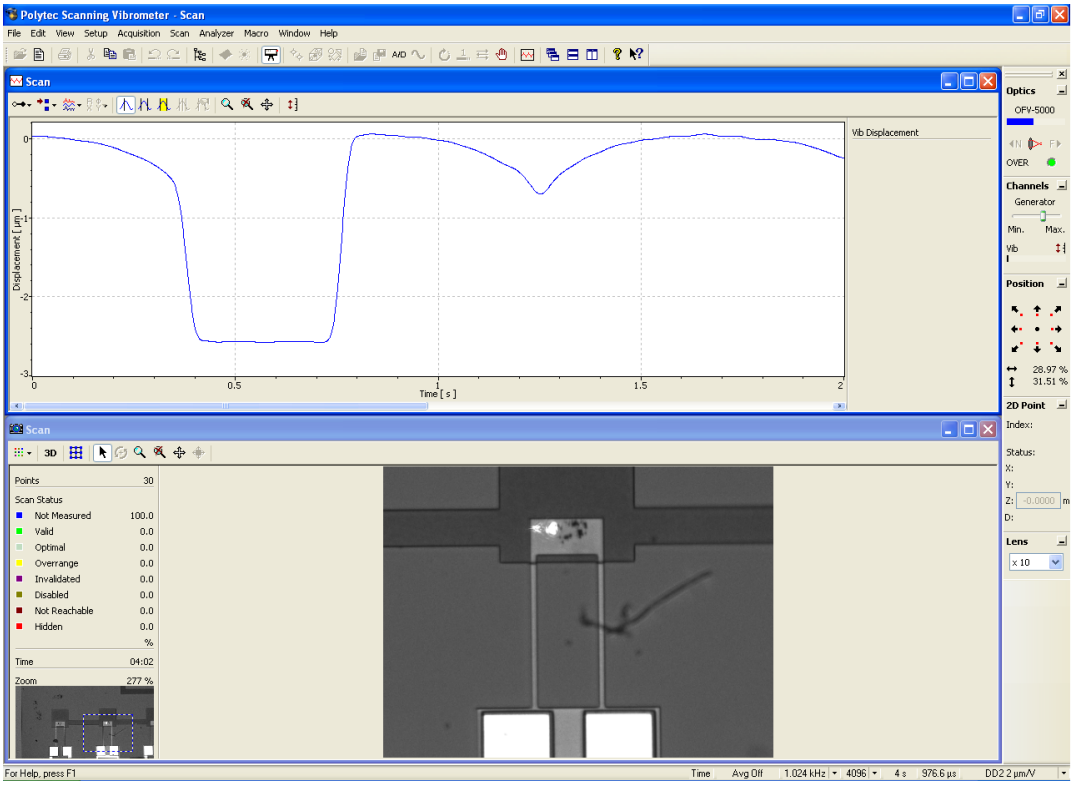

Figure 3.15: *A screen shot of the laser vibrometer interface showing drift during cylcing.*

3.3.4.3 Parameter identification

There is uncertainty in the sensor dimensions due to fabrication tolerances. Since the third generation sensor prototypes use cantilever beam supports, they do not suffer from residual stress effects as was the case with the micro switch. Further, as discussed in Chapter 2, uncertainties in the in-plane dimensions of the beams and plates are insignificant compared to uncertainties in the thickness and gap distance.

The laser vibrometer measurements of the sense-plate displacement provide a good estimate of the gap distance as the difference between the plate height at 0 V and its height during pull-in. As seen in Fig. 3.16, the gap distance was found to be equal to 2.74 μm which is close to the design value of 2.75 μm.

To estimate of the beam thickness we matched the voltage-displacement curve predicted by our model to that measured experimentally as shown in Fig. 3.16. The beam thickness required to obtain matching between the experimental and model predicted curves was $h = 1.44$ μm. Our estimate of the beam thickness compares well with the design value $h = 1.5$ μm and is in agreement with the standard fabrication tolerance of 0.05 μm for the polyMUMPs process [72].

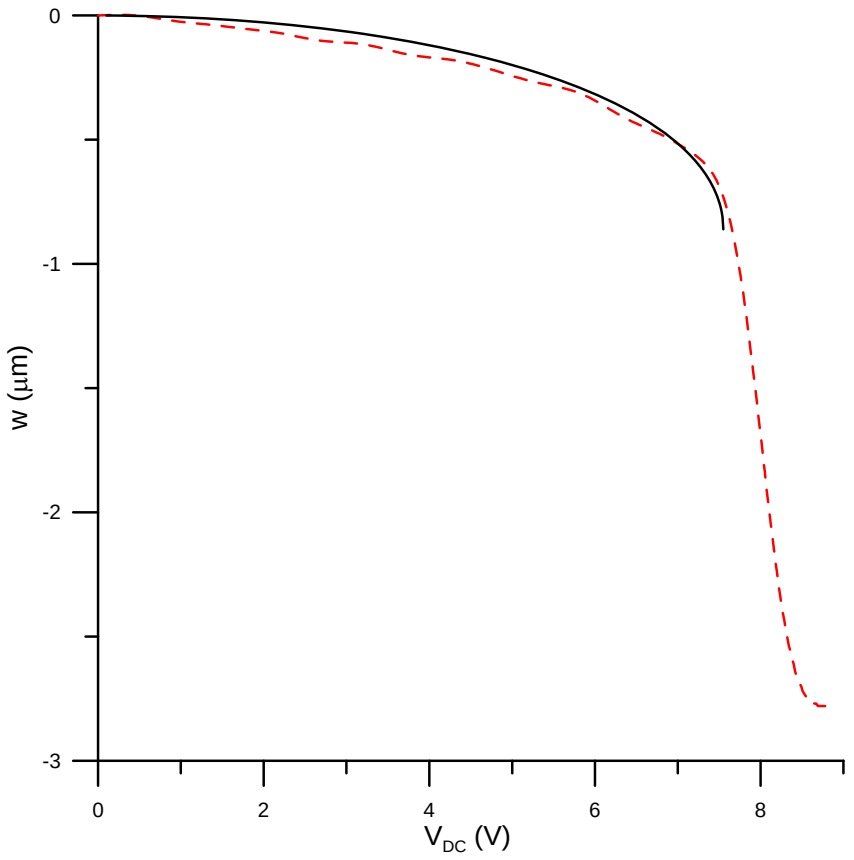

Figure 3.16: *The experimentally measured (dashed line) and model predicted (solid line) sense-plate displacement as a function of voltage.*

3.4 Dynamic Sensor

Like the static sensor, the dynamic sensor concept is built around the distinction between two sensor states: before and after pull-in. However, the difference is how pull-in is reached in both cases. The dynamic sensor is actuated using a DC-AC waveform and is allowed to reach a sustained periodic orbit at a certain excitation frequency. The frequency of excitation is chosen to be close to the cyclic-fold bifurcation point of the sensor. A small mass added to the sense-plate would drive the sensor into pull-in. A requirement for stable operation of the dynamic sensor is to have a frequency-stabilizing circuit. In this regard, Karkkainen *et al.* [77, 78] introduced a MEMS-based AC voltage reference that has an AC error tolerance of about 1.7 μV/V.

3.4.1 Model

The Galerkin method is used to discretize the distributed-parameter model Eq. (3.6), thereby transforming it from a partial-differential equation into a set of nonlinear ordinary-differential equations. Following Nayfeh *et al.* [45], we implemented the discretization in the Lagrangian of the system. Taking into account the inertia of the beam and plate, we express the Lagrangian in the following nondimensional form:

$$\begin{aligned}\pounds = &\int_0^1 w_t^2 dx + M\big[w_t(1,t) + L_c w_{xt}(1,t)\big]^2 \\ &+ \frac{1}{3} M L_C^2 w_{xt}^2(1,t) - \int_0^1 w_{xx}^2 dx + 2M_b \int_0^1 w(x,t)dx \\ &+ 2MM_b\big(L_c w_x(1,t) + w(1,t)\big) \\ &- 2\alpha \frac{(V_{\mathrm{DC}} + V_{\mathrm{AC}}(t))^2}{w_x(1,t)} \ln\Big(\frac{1 - w(1,t) - 2L_c w_x(1,t)}{1 - w(1,t)}\Big)\end{aligned} \tag{3.19}$$

where $M_b = \rho g A L^3/(EId)$ accounts for the beam weight effect which turns out to be negligible compared to the plate weight.

The response of the system is composed of a static $w_s(x)$ and a dynamic component $u(x,t)$. We assume that the displacement can be expressed as

$$w(x,t) = w_s(x) + \sum_{i=1}^{N} \phi_i(x)\, q_i(t) \tag{3.20}$$

where the $\phi_i(x)$ are the mode shapes of the beam-plate system and the $q_i(t)$ are generalized coordinates. The mode shapes for the undamped free vibration problem take the form [45]

$$\phi_i(x) = b_1 \cos\beta_i x + b_2 \sin\beta_i x + b_3 \cosh\beta_i x + b_4 \sinh\beta_i x \tag{3.21}$$

where $\beta_i = \sqrt{\omega_i}$ and the coefficients b_i depend on the applied voltage and can be determined from the boundary conditions.

Substituting Eq. (3.20) into Eq. (3.19) and writing the Lagrange equations, we obtain the following n-dimensional reduced-order model:

$$\begin{aligned}
&\sum_{j=1}^{n} (M_{ij}\ddot{q}_j + C_{ij}\dot{q}_j + K_{ij}q_j) = -\int_0^1 w_s''(x)\phi_i''(x)dx \\
&+ \frac{\alpha}{\Gamma}\big(V_{\mathrm{DC}} + V_{\mathrm{AC}}\big)^2 \ln\Big[\kappa - \sum_{j=1}^{n}\big(\phi_j(1) - 2L_c\phi_j'(1)\big)q_j\Big] \\
&- \frac{\alpha}{\Gamma}\big(V_{\mathrm{DC}} + V_{\mathrm{AC}}\big)^2 \ln\Big(\chi - \sum_{j=1}^{n}\phi_j(1)q_j\Big) \\
&+ \frac{2\alpha L_c}{\Lambda}(V_{\mathrm{DC}} + V_{\mathrm{AC}})^2\Big[\chi\phi_i'(1) + w_s'(1)\phi_i(1) \\
&+ \sum_{j=1}^{n}\big(\phi_j'(1)\phi_i(1) - \phi_j(1)\phi_i'(1)\big)q_j\Big], \quad i = 1,2,\ldots,n
\end{aligned} \tag{3.22}$$

where $\chi = 1 - w_s(x)$, $\kappa = 1 - w_s(x) - 2L_c w_s'(x)$, and

$$
\begin{aligned}
M_{ij} &= \int_0^1 \phi_i(x)\phi_j(x)dx + \tfrac{1}{3}ML_c^2\phi_i'(1)\phi_j'(1) \\
&\quad + \tfrac{1}{4}M\big[2\phi_i(1) + 2L_c\phi_i'(1)\big]\big[2\phi_j(1) + 2L_c\phi_j'(1)\big] \\
K_{ij} &= \int_0^1 \phi_i''(x)\phi_j''(x)dx + M_b\int_0^1 \phi_i(x)dx \\
&\quad + MM_b\Big[\sum_{i=1}^{n}\phi_i(1) + L_c\sum_{i=1}^{n}\phi_i'(1)\Big] \\
C_{ij} &= c\int_0^1 \phi_i(x)\,\phi_j(x)dx \\
\Gamma &= \big[\sum_{j=1}^{n}\phi_j'(1)q_j + w_s'(1)\big]^2 \\
\Lambda &= \Big[\chi - \sum_{j=1}^{n}\phi_j(1)q_j\Big]^2\Big[\sum_{j=1}^{n}\phi_j'(1)q_j + w_s'(1)\Big] \\
&\quad \times\Big\{\kappa - \sum_{j=1}^{n}\big[\phi_j(1) - 2L_c\phi_j'(1)\big]q_j\Big\}
\end{aligned}
$$

3.4.2 Numerical results

We perform a convergence study to determine the number of modes sufficient to capture the full dynamics of the system. We use the systems parameters of the case study in Section 3.3.1. We plot in Fig. 3.17 the limit cycles obtained from one- and two-mode approximations for $V_{\mathrm{DC}} = 5$ V and $V_{\mathrm{AC}} = 0.9\cos(\omega_1 t)$ V, where the excitation frequency is set equal to the natural frequency $\omega_1 = 1.41$ of the first bending mode. The two limit cycles are indistinguishable and hence were presented in two subfigures. Since this oscillatory motion describes a fairly large response, we conclude that a one-mode approximation is sufficient to capture the system dynamics. Therefore, the reduced-order model described in Eq. (3.22) can

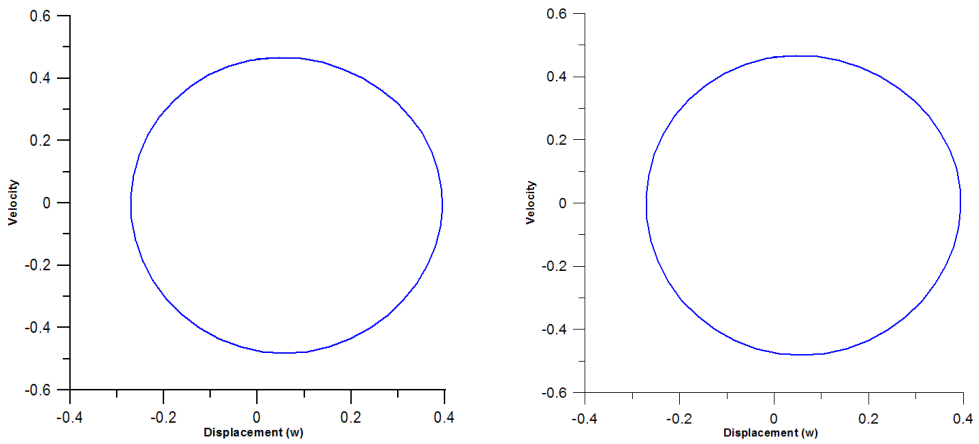

Figure 3.17: *The limit cycles described by the plate center at* $V_{\rm DC} = 5$ *V and* $V_{\rm AC} = 0.9\cos(1.41t)$ *V obtained using (a) 1-mode and (b) 2-mode approximations.*

be simplified to

$$
\begin{aligned}
M_{11}\ddot{q}_j + C_{11}\dot{q}_j + K_{11}q_j = &-\int_0^1 w_s''(x)\phi_1''(x)dx \\
&+ \frac{\alpha\big(V_{\rm DC}+V_{\rm AC}\big)^2}{\big(\phi_1'(1)q_1 + w_s'(1)\big)^2}\ln\left(\frac{\kappa-(\phi_1(1)+2L_c\phi_1'(1))q_1}{\chi-\phi_1(1)q_1}\right) \\
&+ \frac{2\alpha L_c\big(V_{\rm DC}+V_{\rm AC}\big)^2\big[\chi\phi_1'(1)+w_s'(1)\phi_1(1)\big]}{(\chi-\phi_1(1)q_1)\,(\phi_1'(1)q_1+w_s'(1))\,[\kappa-(\phi_1(1)+2L_c\phi_1'(1))q_1]}
\end{aligned}
\tag{3.23}
$$

We use the shooting method [5] to numerically calculate limit cycles of the ordinary-differential equations governing the dynamic response and use Floquet theory [79] to investigate their stability. The frequency-response curves are generated by calculating the limit cycles of the reduced-order model using the shooting method and ascertaining their stability by using Floquet theory. The quality factor of the sensor was taken to be $Q = 300$ in all the cases discussed henceforth [45]. In Fig. 3.18, we show the maximum steady-state displacement of the plate center $(w_s + L_c w_s')_{\rm max}$ for $V_{\rm DC} = 7$ V and $V_{\rm AC} = 0.1\cos(\Omega t)$ V.

The left-side of the curve consists of two branches: a stable branch and an unstable branch meeting at a cyclic-fold bifurcation. Both the stable and unstable

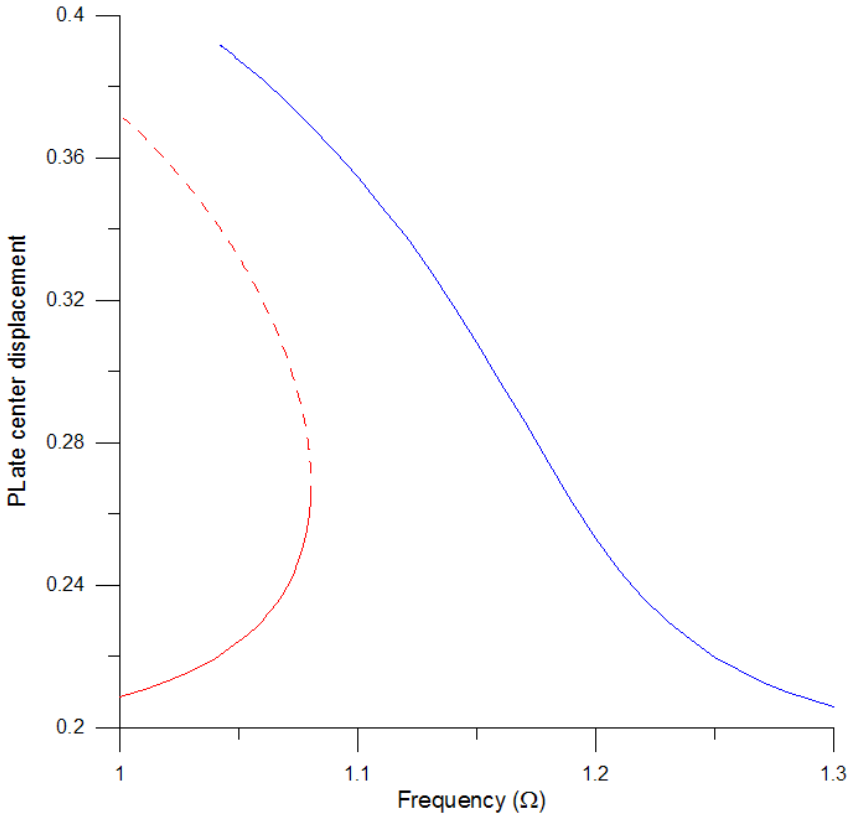

Figure 3.18: *The frequency-response curve for* $V_{\mathrm{DC}} = 7$ *V and* $V_{\mathrm{AC}} = 0.1\cos(\Omega t)$ *V.*

branches correspond to orbits in the phase plane. The cyclic-fold bifurcation is indicated by a slope approaching infinity in the frequency-response curve and a Floquet multiplier exiting the unit circle in the complex plane along the positive real axis. The cyclic-fold bifurcation point is tracked as mass is added to the system (where it moves to the left) and is used as a means of mass sensing.

We note that a cyclic-fold bifurcation occurs at $\Omega = 1.08$ where stable and unstable branches of solutions meet. We also note that the natural frequency of the sensor decreases as the plate mass increases. We use this fact to devise a threshold mass sensor. We let the sensor operate at a point just to the left of the cyclic-fold bifurcation point. As mass is absorbed by or adsorbed to the functional material, the cyclic-fold bifurcation frequency is gradually shifted to the left until enough mass is added to move the bifurcation frequency to the left of the sensor operating point. As a result, the sensor will go into dynamic pull-in, thereby creating a binary

mass sensing mechanism.

3.4.3 Sensitivity analysis

We investigate the sensitivity of the dynamic version of the binary mass sensor to changes in the sense-plate mass. In this regard, we find the normal form of the cyclic-fold bifurcation. Towards that end, we expand the equation of motion of the sense-plate for small oscillations $q_d(t)$ around its static equilibrium position q_s to obtain (see Appendix B)

$$M_e\,\ddot{q}_d + C\,\dot{q}_d - k_1\,q_d - k_2\,q_d^2 - k_3\,q_d^3 = \lambda\,V_{\mathrm{AC}}\cos(\Omega t) \tag{3.24}$$

where M_e and C are the lumped mass and damping coefficients, k_1, k_2, and k_3, are the linear, quadratic, and cubic stiffness coefficients, and λ is the electro-mechanical coupling coefficient.

Under primary resonance excitation, the frequency-response equation of the Generalized Duffing Oscillator described by Eq. (3.24) takes the form [79]

$$\left(\frac{\lambda}{2\omega}\right)^2 = 4\mu^2\,a^2 + A^2\,a^6 - 2A\,a^4\,\sigma + a^2\,\sigma^2 \tag{3.25}$$

where $\omega = \sqrt{k_1/M_e}$ is the natural frequency, $\mu = C/M_e$, $\sigma = \Omega - \omega$ is a detuning parameter which expresses the nearness of the excitation frequency to the natural frequency, and a is the response amplitude defined by [79]

$$q_d(t) = a\,\cos(\Omega t - \epsilon^2\sigma t) + \cdots \tag{3.26}$$

Higher order terms in the response have been neglected and the term $\epsilon^2\sigma t$ represents nonlinear drift in the response phase angle over long time $\epsilon^2 t$.

The coefficient of effective nonlinearity A is defined as [79]

$$A = \frac{9\left(\frac{k_1}{M_e}\right)\left(\frac{k_3}{M_e}\right) - 10\left(\frac{k_2}{M_e}\right)^2}{24\left(\frac{k_1}{M_e}\right)^{3/2}} \tag{3.27}$$

A cyclic-fold bifurcation occurs at points in the frequency-response curves where an infinite slope occurs. This condition corresponds to [5]

$$\frac{\partial \sigma}{\partial a} = 0 \tag{3.28}$$

Applying the condition to the frequency-response equation, Eq. (3.25), yields

$$\sigma_\circ = A\, a_\circ^2 \tag{3.29}$$

where $(a_\circ, \sigma_\circ)$ are the amplitude and frequency of the cyclic-fold bifurcation.

Sensitivity of the dynamic mass sensor is the ratio of change in the location of the cyclic-fold bifurcation $\delta\sigma_\circ$ to change in the sense-plate mass δM

$$S_m = \frac{\delta \sigma_\circ}{\delta M} \tag{3.30}$$

Perturbations in mass M would result in perturbations in the sensor natural frequency and response amplitude a, thus from Eq. (3.29) and Eq. (3.36)

$$\frac{\delta \sigma_\circ}{\delta M} = a_\circ^2 \frac{\delta A}{\delta M} + 2 a_\circ A \frac{\delta a_\circ}{\delta M} \tag{3.31}$$

We note from Appendix B that

$$M_e \propto M \tag{3.32}$$

$$\frac{k_1}{M_e} \propto \frac{1}{M} \tag{3.33}$$

$$\frac{k_2}{M_e} \propto \frac{\alpha L_c}{M} V_{\mathrm{DC}}^2 \tag{3.34}$$

$$\frac{k_3}{M_e} \propto \frac{\alpha L_c}{M} V_{\mathrm{DC}}^2 \tag{3.35}$$

For weakly nonlinear systems, the term $(k_2/M_e)^2$ is small compared to $(k_1/M_e)(k_2/M_e)$,

thus, we can infer from Eq. (3.27) that

$$A \propto \frac{\alpha\, L_c}{\sqrt{M}} V_{\mathrm{DC}}^2 \tag{3.36}$$

therefore

$$\frac{\delta A}{\delta M} \propto \frac{\alpha L_c}{M\sqrt{M}} V_{\mathrm{DC}}^2 \tag{3.37}$$

Substituting Eq (3.29) into the frequency-response equation, Eq. (3.25), we obtain

$$\left(\frac{\lambda}{2\omega}\right)^2 = 4\mu^2\, a_\circ^2 \tag{3.38}$$

Thus, we can write

$$a_\circ = \frac{\lambda}{4\,\omega\,\mu} \tag{3.39}$$

We note from Appendix B that

$$C \propto \frac{1}{Q} \tag{3.40}$$

$$\lambda \propto \alpha L_c V_{\mathrm{DC}} \tag{3.41}$$

therefore

$$a_\circ \propto \alpha L_c V_{\mathrm{DC}} Q M \sqrt{M} \tag{3.42}$$

and

$$\frac{\delta a_\circ}{\delta M} \propto \alpha L_c V_{\mathrm{DC}} Q \sqrt{M} \tag{3.43}$$

Substituting Eqs. (3.36), (3.37), (3.42), and (3.43) into Eq. (3.31), we obtain an expression for the sensor sensitivity in terms of the nondimensional system

parameters

$$S_m = \frac{\delta\sigma_\circ}{\delta M} \propto \alpha V_{\rm DC}^2\,(\alpha V_{\rm DC})^2 L_c^3\, M^{\frac{3}{2}}\, Q^2 \tag{3.44}$$

Equation (3.44) indicates that the dynamic sensor is more sensitive to the strength of the electrostatic field and the length of the moment arm of the sense-plate mass than the static sensor. Specifically, the term $\alpha V_{\rm DC}^2$ represents the contribution to sensitivity by the static component of the waveform, while the term $(\alpha V_{\rm DC})^2$ represents the contribution to the sensitivity by the dynamic component of the waveform. It is also sensitive to increase in the mass ratio of the sense-plate to the cantilever beam. Finally, it is quadratically sensitive to the quality factor. In contrast, frequency-shift mass sensors use the sensor displacement as a detector and, therefore, their sensitivity is linearly proportional to the quality factor.

Further, using Eqs. (3.8), we can rewrite the sensor sensitivity in terms of the sensor dimensional parameters as

$$S_m \propto \frac{V_{\rm DC}^2}{d^3}\Big(\frac{V_{\rm DC}}{d^3}\Big)^2\Big(\frac{L^3}{EI}\Big)^3\Big(\frac{\hat{m}_p}{m}\Big)^{\frac{3}{2}}\, A_p^3\, Q^2 \tag{3.45}$$

where $\hat{m}_p$ and m are the sense-plate mass and the cantilever beam mass, respectively, and $A_p = L_p\, b_p$ is the surface area of the sense-plate. In addition to the observations above, this equation reveals that that the sensitivity of the sensor is proportional to the cube of the surface area of the sense-plate. Moreover, the equation shows that the sensor sensitivity is counter proportional to the cube of the stiffness of the cantilever beam. We contrast this result with the conclusion of Thundat *et al.* [80] that sensitivity is inversely proportional to the thickness for cantilever beam frequency-shift sensors.

As a quantitative example, we track the location of the cyclic-fold bifurcation frequency as mass is added to the plate. We add a small mass $\delta m = 35$ picogram to the plate and plot the frequency-response curve for $V_{\rm DC} = 7$ V and $V_{\rm AC} = 0.1\cos(\Omega t)$ V. We found that the bifurcation point is shifted by 4 Hz.

We then study the effect of decreasing the beam thickness h on the sensitivity of

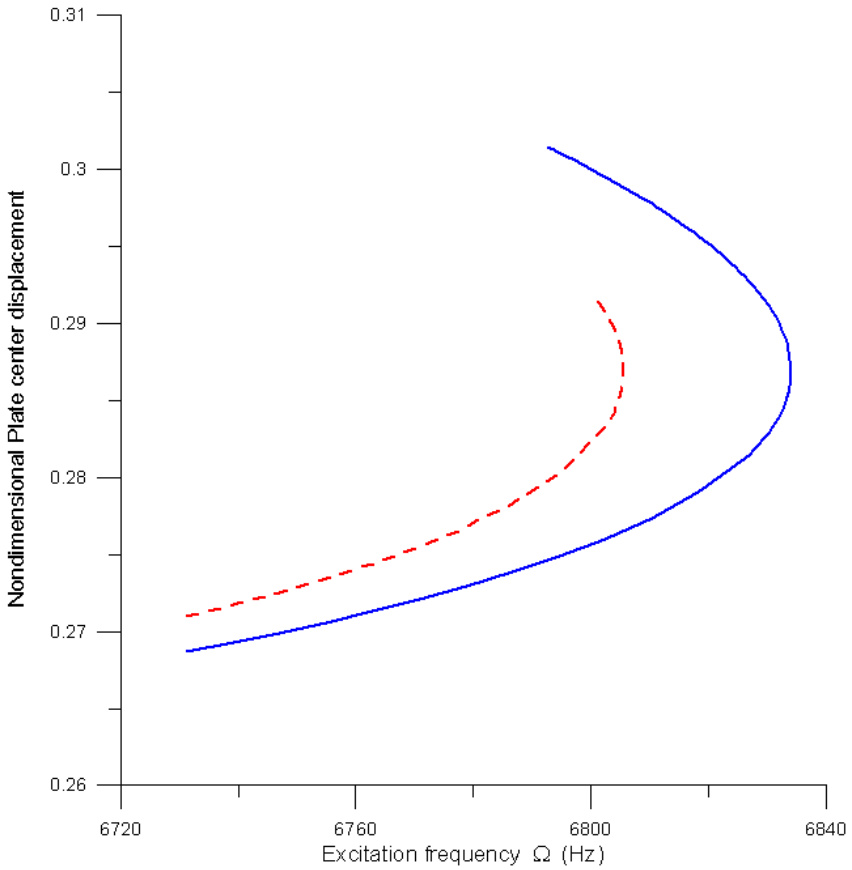

Figure 3.19: *The cyclic-fold bifurcation point of the modified sensor ($h = 1.3\,\mu m$) operating with $V_{\rm DC} = 6$ V and $V_{\rm AC} = 0.03$ V with (dashed line) and without (solid line) an added mass of $\delta m = 30$ picogram.*

the sensor. Equation (3.45) shows that the sensitivity of the micro cantilever mass sensors is inversely proportional to h^9. We decrease the structural thickness of the beam from $h = 1.5\,\mu$m to $h = 1.3\,\mu$m, thereby decreasing the static pull-in voltage to $V_{\rm pi} = 6.7$ V. We excite the sensor using $V_{\rm DC} = 6$ V and $V_{\rm AC} = 0.03\cos(\Omega t)$ V. In Fig. 3.19, we plot the frequency-response curves with and without an added mass of $\delta m = 30$ picogram. The shift in the location of the bifurcation point is 29 Hz, one-order of magnitude larger than that for the thicker beam. In fact, an added mass of $\delta m = 1$ picogram produces a shift of 3 Hz in the location of the bifurcation point, Fig. 3.20, for the thinner beam. It is worth noting here that 1 picogram corresponds to a sphere of diameter equal to 1 μm.

It is practical to measure frequency shifts on this order. However, the overall

resolution of the threshold mass sensor will depend on the stability of the waveform provided by the reference excitation source. The dynamic sensor does not suffer from external disturbances since the environment noise has low frequency (usually a few Hertz) that is attenuated by the sensor being driven at much higher frequencies.

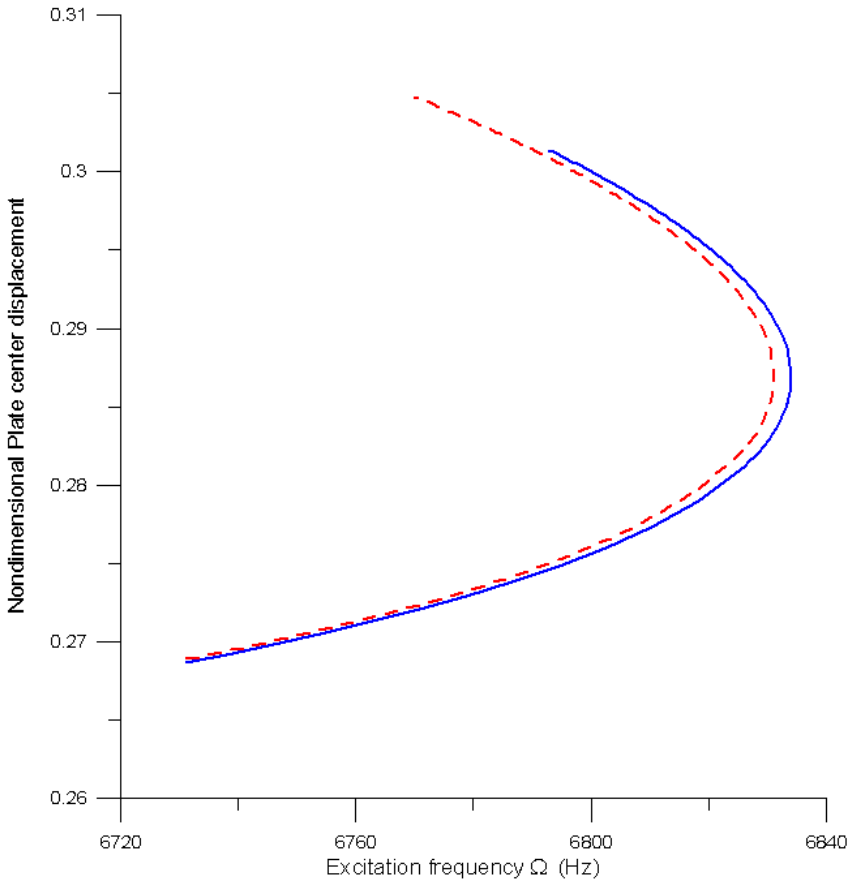

Figure 3.20: *The cyclic-fold bifurcation point of the modified sensor ($h = 1.3\,\mu m$) operating with $V_{\mathrm{DC}} = 6$ V and $V_{\mathrm{AC}} = 0.03$ V with (dashed line) and without (solid line) an added mass of $\delta m = 1$ picogram.*

Chapter 4

Conclusions and Future Work

4.1 Concluding Remarks

We summarize and discuss here the most important findings in this work focused on the use of the pull-in instability in electrostatic MEMS for actuation and sensing.

4.1.1 MEMS micro switch

We developed methods to dynamically actuate capacitive shunt CPW switches. The switches were made of electroplated gold bridges on CPWs fabricated on silicon substrates. The lower bound on static actuation, static pull-in voltage V_{SP}, was found to be 68.5 V. Dynamic actuation was investigated using force and frequency sweeps in the vicinity of the switch natural frequency. We quantified the voltage savings of dynamic actuation V_{DP} over static actuation using a Figure of Merit defined as

$$FoM = \frac{V_{\mathrm{SP}} - V_{\mathrm{DP}}}{V_{\mathrm{SP}}}$$

Greater voltage savings were obtained using a frequency sweep, $FoM = 60$ %, than those obtained using a force sweep, $FoM = 40$ %. Dynamic switching using a force sweep requires increasing the voltage amplitude at a constant frequency until dynamic pull-in occurs. On the other hand, dynamic switching using a frequency sweep requires, in addition, a down-sweep past the nonlinear resonance frequency

to trigger pull-in.

It is obvious that as the FoM increases, the switching time will also increase since higher FoM occurs at lower DC voltages. To address this shortcoming, we are proposing to implement dynamic switching using transient switching methods in order to obtain a shorter switching time of the same order as that obtained using static switching. We developed two switching methods to facilitate the use of the lower actuation voltage realized by the frequency-sweep technique. A fixed-frequency method simply sends a sudden waveform of the same order as those shown in Fig. 2.11 in the CPW at an excitation frequency within a narrow band around the cyclic-fold bifurcation. A shifted-frequency method maintains a waveform of the same order as those shown in Fig. 2.11 in the CPW for a few excitation periods before shifting the excitation frequency up or down by a discrete amount $\delta\Omega$. The fixed-frequency method is simpler to implement. The shifted-frequency method requires an additional step while providing a wider actuation frequency band and the minimum realizable switching time for actuation frequencies within subinterval B_2.

The switching time obtained using dynamic actuation was always longer than that obtained using static actuation except for shifted-frequency switching when used in subinterval B_2 where the two switching times were comparable.

We adopted a reduced-order model to characterize the switch response. The model accounts for midplane stretching, electrostatic forcing due to non-overlapping parallel plates, and squeeze-film damping. We developed an identification routine to estimate the thickness and residual stress of the bridge and the capacitor gap. These parameters were used to update the model and arrive at the most accurate representation of the problem.

We found that squeeze-film damping is the dominant damping mechanism in the switch under study even for small motions. Accounting for squeeze-film damping effects using a linear damping model leads to erroneous results for large motions. We found that damping is the dominant factor in reducing the switching time obtained using dynamic actuation except for the subinterval B_2 where the switching time is

already close to the minimum switching time obtained for static actuation.

Finally, we developed a technique to measure the change in the voltage drop across the shunt switch due to charge trapping on the insulation layer in the switch. Our technique uses the FFT of the measured bridge response to estimate the voltage change.

4.1.2 Binary micro gas sensors

We developed a binary mass sensing technique that uses the pull-in instability as a detection mechanism. The sensor indicates when an added mass has exceeded a threshold amount by going into pull-in to switch from non-contact, 0-state, to contact with the substrate, 1-state. This sensing mechanism has two advantages. First, it is simple since it dispenses with the need for readout electronics which reflects upon the overall cost and complexity of the sensor. Second, it enhances the sensitivity of the mass sensor compared to similar-sized sensors using static deflection and frequency-shift detection methods.

We developed static and dynamic versions of this mass sensor. Both versions employ a common structure made of a sense-plate supported by a micro cantilever beam and actuated by an electrode under the sense-plate. The static version uses static pull-in as a detection mechanism. The dynamic version uses dynamic pull-in subsequent to a local, cyclic-fold, bifurcation as a detection mechanism.

We investigated sensors sensitivity analytically and developed formulas describing the dependence of the static and dynamic mass sensors as functions of the sensors parameters. We found that the sensitivity of the static version of the binary mass sensor represents the upper bound on the sensitivity of statically detected electrostatic MEMS mass sensors. The formula indicates that the sensitivity of the static mass sensor is proportional to the strength of the electrostatic field represented by the nondimensional potential difference αV_{DC}^2 and the effective capacitor gap $(1-w)$. Moreover, the sensitivity is proportional the ratio of the sense-plate length L_p to the cantilever beam length L since it increases the moment arm of the sense-plate mass with respect to the cantilever beam end.

For the dynamic mass sensor, the formula for sensitivity indicates that the dynamic sensor is more sensitive to the strength of the electrostatic field and the length of the moment arm of the sense-plate mass than the static sensor. The sensor is also sensitive to increase in the mass ratio of the sense-plate to the cantilever beam. The formula also shows that the sensor is quadratically sensitive to the quality factor. In contrast, frequency-shift mass sensors use the sensor displacement as a detector and, therefore, their sensitivity is linearly proportional the quality factor. Finally, it was found out that the sensitivity of the sensor is proportional to the cube of the surface area of the sense-plate while it is counter proportional to the cube of the stiffness of the cantilever beam.

The sensitivity formula of the static mass sensor was used to create a sensor calibration table. The table shows that the sensor can detect an added mass as small 3 nanograms. A study of the dynamic mass sensor using a reduced-order model found that it can detect an added mass as small as 1 picogram. This is three orders of magnitude better than the static mass sensor.

The static sensor is more susceptible to external disturbances than the dynamic sensor. It is required that the static sensor be excited very close to pull-in. Isolating the sensor from external disturbances helps improve the sensor stability. On the other hand, the stability margin for the dynamic sensor is wider than for the static sensor since it is only required to stabilize the frequency of excitation. The environment noise usually has low frequency which is attenuated by the sensor being driven at much higher frequencies.

We used the binary mass sensors as platforms to realize a formaldehyde vapor sensor by depositing doped polyaniline on a sense-plate. Three generations of the sensor were fabricated and tested in order to optimize the sensor design.

Finally, experimental findings indicate that the static sensor suffers from sensitivity to external disturbances in a manner similar to that seen for inertial sensors that uses static detection. Deploying the static sensor will require a design to decouple the response of the sensor to changes in the mass of the sense-plate from external disturbances. On the other hand, the dynamic sensor does not suffer from

this shortcoming in a manner analogous to inertial sensors that use frequency-shift as detection method.

4.2 Publications

- Khater M., Abdel-Rahman E., and Nayfeh A., "A Mass Sensing Technique for Eletcrostatically-Actuated MEMS", *Proceeding of the ASME 2009 International Design Engineering Technical Conferences & Computers and Information in Engineering Conference - IDETC/CIE*, California, USA, 2009.

- Vummidi K., Khater M., Abdel-Rahman E., Nayfeh A., and Raman s., "Dynamic Pull-in of Shunt Capacitive MEMS Switches", Proceedings of Eurosensors XXIII conference, Lausanne, Switzerland, 2009.

- Khater M., Vummidi K., Abdel-Rahman E., Nayfeh A., and Raman s., "Dynamic switching of MEMS Shunt Switches", Proceeding of the ASME 2010 International Design Engineering Technical Conferences & Computers and Information in Engineering Conference IDETC/CIE 2010, Montreal, Canada, 2010.

- Khater M., Vummidi K., Abdel-Rahman E., Raman S., and Nayfeh A., "Dynamic actuation methods for capacitive MEMS shunt switches", *Journal of Micromechanics and Microengineering*, Vol. 21, pp. 1–12, 2011.

4.3 Future Work

4.3.1 MEMS micro switch

A proposed plan for future work on the micro switch follows:

1. Conduct an experiment on multiple-bridge switches to investigate whether mechanical coupling occurs between the bridges in this case and how much

it affects the performance of the switch. A proposed experimental procedure is to test a three-bridge switch and compare the performance of the middle bridge, which is affected symmetrically by the two bridges on either side, to the bridges either side, which are asymmetrically affected by a single neighboring bridge. If no difference in response are observed, we can then infer that mechanical coupling between the bridges has insignificant effect on switch dynamics.

2. Conduct an experiment to measure the motions in the bridge posts and compare the results across different post designs. Posts can be a significant source of damping in switches. Damping is a crucial factor for the performance of dynamically actuated switches. Higher damping requires higher actuation voltages to drive the switch to pull-in.

3. Study experimentally and analytically post pull-in dynamics of the switch using the models developed by Vyasarayani *et al.* [81]. This effort will offer insight into factors affecting the switching time and switch failure mechanisms.

4. Conducting the experiment under vacuum would have the advantage of eliminating the effects of squeeze-film damping.

4.3.2 Binary micro gas sensors

A proposed plan for future work on the MEMS binary mass sensors follows:

1. Experimentally demonstrate the static version of the mass sensor.

2. Investigate techniques to enhance the robustness and stability of the static version of the mass sensor against external disturbances.

3. Experimentally demonstrate the dynamic version of the mass sensor.

4. Investigate sensor drift in both versions.

5. Design and demonstrate binary mass sensors using paddle structures (fixed-fixed beams supporting a center sense-plate) and compare their performance to the cantilever supported sensors.

References

[1] Hsu T., *MEMS & Microsystems: Design and Manufacture*, McGraw-Hill, New York, 2002.

[2] Maluf N. and Williams K., *An Introduction to Microelectromechanical Systems Engineering*, 2nd edition, Artech House Inc., 2004.

[3] Younis M., "Investigation of the Mechanical Behavior of Microbeam-Based MEMS Devices", *MS. thesis, Virginia Polytechnic Institute and State University*, 2001.

[4] Toshiyoshi H., *Comprehensive Microsystems: Electrostatic Actuation*, Elsevier Ltd., 2008.

[5] Nayfeh A. and Balachandran B., *Applied Nonlinear Dynamics*, John Wiley & Sons, 1995.

[6] Zhang Y. and Zhao Y., "Numerical and Analytical Study on the Pull-in Instability of Micro-Structure under Electrostatic Loading", *Sensors and Actuators A*, Vol. 127, pp. 366-380, 2006.

[7] Senturia S., *Microsystem Design*, Kluwer Academic Publishers, 2001.

[8] Nayfeh A., Younis M., and Abdel-Rahman E., "Dynamic Pull-in Phenomenon in MEMS Resonators", *Nonlinear Dynamics*, Vol. 48, pp. 153-163, 2007.

[9] Ahn Y., Guckel H., and Zook J., "Capacitive Microbeam Resonator Design", *Journal of Micromechanics and Microengineering*, Vol. 11, pp. 70-80, 2001.

[10] Chowdhury S., Ahmadi M., and Miller W., "A Closed-Form Model for the Pull-in Voltage of Electrostatically Actuated Cantilever Beams", *Journal of Micromechanics and Microengineering*, Vol. 11, pp. 720-725, 2005.

[11] Chaterjee S. and Pohit G., "A large Deflection Model for the Pull-in Analysis of Electrostatically Actuated Microcantilever Beams", *Journal of Sound and Vibration*, Vol. 322, pp. 969-986, 2009.

[12] Hung E. and Senturia S., "Extending the Travel Range of Analog-Tuned Electrostatic Actuators", *Journal of Microelectromechanical Systems*, Vol. 8, pp. 497-505, 1999.

[13] Busta H., Amantea R., Furst D., Chen J., Turowski M., and Mueller C., "A MEMS Shield Structure for Controllin Pull-in Forces and Obtaining Increased Pull-in Voltages", *Journal of Micromechanics and Microengineering*, Vol. 15, pp. 756-763, 2005.

[14] Rosa M., Bruyker D., Volkel A., Peeters E., and Dunec J., "A Novel External Electrode Configuration for the Electrostatic Actuation of MEMS Based Devices", *Journal of Micromechanics and Microengineering*, Vol. 14, pp. 446-451, 2004.

[15] Song Y., Lee H., and Esashi M., "Low Actuation Voltage Capacitive Shunt RF-MEMS Switch Having a Corrugated Bridge", *IEICE TRANS. Electronics*, Vol. E89-C, pp. 1880-1887, 2006.

[16] Rebeiz G., "RF MEMS Switches: Status of the Technology", *12th International Conference on Solid State Sensors, Actuators and Microsystems*, Boston, pp. 1726-1729, 2003.

[17] Varadan V., Venoy K., and Jose K., *RF MEMS and their Applications*, John Wiley & Sons, 2003.

[18] Rebeiz G., *RF MEMS: Theory, Design, and Technology*, John Wiley & Sons, 2003.

[19] Wong C., Tan M., and Liew K., "Electrical Characterisation of RF Capacitive Microswitch", *Sensors and Actuators A*, Vol. 102, pp. 296-310, 2003.

[20] De Wolf I. and Van Spengen W., "Techniques to Study the Reliability of Metal RF MEMS Capacitive Switches", *Microelectronics Reliability*, Vol. 42, pp. 1789-1794, 2002.

[21] Song M., Yin J., He X., and Wang Y., "Design and Analysis of a Novel Low Actuation Voltage Capacitive RF MEMS Switches", *Proceedings of the 3rd IEEE International Conference on Nano/Micro Engineered and Molecular Systems*, Sanya, China, 2008.

[22] Cho I., Song T., Baek S., and Yoon E., "A Low-Voltage and Low-Power RF MEMS Series and Shunt Switches Actuated by Combination of Electromagnetic and Electrostatic Forces", *IEEE Transactions on Microwave Theory and Techniques*, Vol. 53, pp. 2450-2457, 2005.

[23] Patton S. and Zabinski J., "Effects of Dielectric Charging on Fundamental Forces and Reliability in Capacitive Microelectromechanical Systems Radio Frequency Switch Contacts", *Journal of Applied Physics* Vol. 99, pp. 094910(1-11), 2006.

[24] Papaioannou G. and Papapolymerou J., "Dielectric Charging Mechanisms in RF-MEMS Capacitive Switches", *Proceedings of the 2nd European Microwave Integrated Circuits Conference*, pp. 359-362 , Munich, Germany, 2007.

[25] Goldsmith C., Ehmke J., Malczewski A., Pillans B., Eshelman S., Yao Z., Brank J., and Eberly M., "Lifetime Characterization of Capacitive RF MEMS Switches", *IEEE MTT-S Int. Microwave Symp. Dig.*, Vol. 1, pp. 227-230, 2001.

[26] Peng Z., Palego C., Halder S., Hwang J., Jahnes C., Etzold K., Cotte J., and Magerlein J., "Dielectric Charging in Electrostatically Actuated MEMS Ohmic Switches", *IEEE Transactions on Device and Materials Reliability*, Vol. 8, pp. 642-646, 2008.

[27] Yuan X., Hwang J., Forehand D., and Goldsmith C., "Modelling and Characterization of Dielectric-Charging Effects in RF MEMS Capacitive Switches", *Microwave Symposium Digest, 2005 IEEE MTT-S International*, Vol. 8, pp. 753-756, 2005.

[28] Peng Z., Yuan X., Hwang J., Forehand D., and Goldsmith C., "Top vs Bottom Charging of the Dielectric in RF MEMS Capacitive Switches", *Proceedings of Asia-Pacific Microwave Conference, APMC*, Vol. 3, pp. 1535-1538, 2006.

[29] Peroulis D., Pacheco S., and Kaheti L., "RF MEMS Switches With Enhanced Power-Handling Capabilities", *IEEE Transactions on Microwave Theory and Techniques*, Vol. 52, pp. 59-68, 2004.

[30] Sadek K., Lueke J., and Moussa W., "A Coupled Field Multiphysics Modeling Approach to Investigate RF MEMS Switch Failure Modes under Various Operational Conditions", *Sensors*, Vol. 9, pp. 7988-8006, 2009.

[31] Chan R., Lesnick R., Becher D., and Feng M., "Low-Actuation Voltage RF MEMS Shunt Switch with Cold Switching Lifetime of Seven Billion Cycles", *Journal of Microelectromechanical Systems*, Vol. 12, pp. 713-719, 2003.

[32] Blondy P., Crunteanu A., Pothier A., Tristant P., Catherinot A., and Champeaux C., "Effects of Atmosphere on the Reliability of RF-MEMS Capacitive Switches", *Proceedings of the 2nd European Microwave Integrated Circuits Conference*, Vol. 9, pp. 548-550, 2007.

[33] Peng Z., Palego C., Hwang J., Forehand D., Goldsmith C., Moody C., Malczewski A., Pillans B., Daigler R., and Papapolymerou J., "Impact of Humidity on Dielectric Charging in RF MEMS Capacitive Switches", *IEEE Microwave and Wireless Components Letters*, Vol. 19, pp. 299-301, 2009.

[34] Seeger J. and Boser B., "Parallel-Plate Driven Oscillations and Resonant Pull-in", *Solid-State Sensors, Actuator and Microsystem Workshop*, Hilton Head Island, 2007.

[35] Nielson G. and Barbastathis G., "Dynamic Pull-In of Parallel-Plate and Torsional Electrostatic MEMS Actuators", *Journal of Microelectromechanical Systems*, Vol. 15, pp. 811-821, 2006.

[36] Nielson G., Olsson R., Bogart G., Resnick P., Spahn O., Tigges C., Grossetete G., and Barbastathis G., "Dynamic Pull-in and Switching for Sub-Pull-in Voltage Electrostatic Actuation", *Solid-State Sensors, Actuators and Microsystems Conference, Tranducers 2007*, 2007.

[37] Fargas-Marques A. and Shkel A., "On Electrostatic Actuation beyond Snapping Condition", *Sensors, IEEE*, pp. 600-603, 2005.

[38] Fargas-Marques A., Casals-Terre J., and Shkel A., "Resonant Pull-in Condition in Parallel-Plate Electrostatic Actuators", *Journal of Microelectromechanical Systems*, Vol. 16, pp. 1044-1053, 2007.

[39] Vummidi K., Hammond J., Costa J., and Raman S., "Resonant Pull-in For a Variable Gap Lateral Contact RF MEMS Switch", *IEEE 23rd International Conference*, Hong Kong, China, 2010.

[40] Khater M., Vummidi K., Abdel-Rahman E., Raman S., and Nayfeh A., "Dynamic actuation methods for capacitive MEMS shunt switches", *Journal of Micromechanics and Microengineering*, Vol. 21, pp. 1–12, 2011.

[41] Ilic B., Yang Y., and Craighead H., "Virus Detection Using Nanoelectromechanical Devices", *Applied Physics Letters*, Vol. 85, pp. 2604-2606, 2004.

[42] Zribi A., A. Knobloch, W. Tian, and S. Goodwin, "Micromachined Resonant Multiple Gas Sensor", *Sensors and Actuators A*, Vol. 122, pp. 31-38, 2005.

[43] Dohn S., Hansen O., and Boisen A., "Cantilever Based Mass Sensor with Hard Contact Readout", *Applied Physics Letters*, Vol. 88, pp. 264104(1-3), 2006.

[44] Waggoner P. and Craighead H., "Micro- and Nanomechanical Sensors for Environmental, Chemical, and Biological Detection", *Lab Chip*, Vol. 7, pp. 1238-1255, 2007.

[45] Nayfeh A., Ouakad H., Najar F., Choura S., and Abdel-Rahman E., "Nonlinear Dynamics of a Resonant Gas Sensor", *Nonlinear Dynamics*, Vol. 59, pp. 607-618, 2010.

[46] Datskos P. and Sauers I., "Detection of 2-Mercaptoethanol Using Gold-Coated Micromachined Cantilevers", *Sensors and Actuators B*, Vol. 61, pp. 75-82, 1999.

[47] Jensenius H., Thaysen J., Rasmussen A., Veje L., Hansen O., and Boisen A., "A Microcantilever-Based Alcohol Vapor Sensor-Application and Response Model", *Applied Physics Letters*, Vol. 76, pp. 2615-2617, 2000.

[48] Zhang W., Baskaran R., and Turner K., "Effect of Cubic Nonlinearity on Auto-Parametrically Amplified Resonant MEMS Mass Sensor", *Sensors and Actuators A*, Vol. 102, pp. 139-150, 2002.

[49] Zhang W. and Turner K., "Application of Parametric Resonance Amplification in a Single-Crystal Silicon Micro-Oscillator Based Mass Sensor", *Sensors and Actuators A*, Vol. 122, pp. 23-30, 2005.

[50] Choi S., Kim S., Yoon Y., and Allen M., "Exploitation of Nonlinear Effects for Enhancement of the Sensing Performance of Resonant Sensors", *Solid-State Sensors, Actuators and Microsystems Conference*, pp. 1745-1748, 2007.

[51] Cleland A., "Thermomechanical Noise Limits on Parametric sensing with Nanomechanical Resonators", *New Journal of Physics*, Vol. 235, pp. 1-16, 2005.

[52] Tseytlin Y., "High Resonant Mass Sensor Evaluation: An Effective Method", *Review of Scientific Instruments*, Vol. 76, pp. 115101(1-6), 2005.

[53] Dohn S., Sandberg R., Svendsen W., and Boisen A., "Enhanced Functionality of Cantilever Based Mass Sensors Using Higher Modes and Functionalized Particles", *The 13th International Conference on Solid-state Sensors, Actuators and Microsystems*, Seoul, pp. 636-639, 2005.

[54] Lobontiu N., Ilic B., Garcia E., Reissman T., and Craighead H., "Modeling of Nanofabricated Paddle Bridges for Resonant Mass Sensing", *Review of Scientific Instruments*, Vol. 77, pp. 073301(1-9), 2006.

[55] Lobontiu N., Lupea I., Ilic R., and Craighead H., "Modeling, Design, and Characterization of Multisegment Cantilevers for Resonant Mass Detection", *Journal of Applied Physics*, Vol. 103, pp. 064306(1-10), 2008.

[56] Xie H., Vitard J., Haliyo S., and Regnier S., "Enhanced Sensitivity of Mass Detection Using the First Torsional Mode of Microcantilevers", *Measurement Science and Technology*, Vol. 19, pp. 1-7, 2008.

[57] Younis M. and Alsaleem F., "Exploration of New Concepts for Mass Detection in Electrostatically-Actuated Structures Based on Nonlinear Phenomena", *Journal of Computational and Nonlinear Dynamics*, Vol. 4, pp. 021010(1-13), 2009.

[58] Luan B. and Robbins M. , "The Breakdown of Continuum Models for Mechanical Contacts", *Nature*, Vol. 435, pp. 929-932, 2005.

[59] Emam S., "A Theoretical and Experimental Study of Nonlinear Dynamics of Buckled Beams", PhD thesis, *Virginia Polytechnic Institute and State University*, 2002.

[60] Younis M., Abdel-Rahman E., and Nayfeh A., "A Reduced-Order Model for Electrostatically Actuated Microbeam-Based MEMS", *Journal of Microelectromechanical Systems*, Vol. 12, pp. 672-680, 2003.

[61] Osterberg P. and Senturia S., "M-TEST: A Test Chip for MEMS Material Property Measurement Using Electrostatically Actuated Test Structures", *Journal of Microelectromechanical Systems*, Vol. 6, pp. 107–118, 1997.

[62] Krylov S., "Lyapunov Exponents as a Criterion for the Dynamic Pull-in Instability of Electrostatically Actuated Microstructures", *International Journal of Non-Linear Mechanics*, Vol. 42, pp. 626-642, 2007.

[63] Shabana A., *Vibration of Discrete and Continuous Systems*, 2nd edition, Springer-Verlag, New York, 1997.

[64] Ploytec Inc., OFV-5000 Vibrometer Controller user manual, `www.polytec.com`.

[65] Vummidi K., Khater M., Abdel-Rahman E., Nayfeh A., and Raman s., "Dynamic Pull-in of Shunt Capacitive MEMS Switches", Proceedings of Eurosensors XXIII conference, Lausanne, Switzerland, pp. 622-625, 2009.

[66] Veeco Inc., Wyko-NT1100 Optical Profiling System datasheet, `www.veeco.com`.

[67] Abdel-Rahman E., Younis M., and Nayfeh A., "Characterization of the Mechanical Behavior of an Electrically Actuated Microbeam", *Journal of Micromechanics and Microengineering*, Vol. 12, pp. 759–766, 2002.

[68] Li G. and Hughes H., "Review of Viscous Damping in Micro-machined Structures", *Proceedings of SPIE*, Vol. 4176, pp. 30-46, 2000.

[69] Najar F., Nayfeh A., Abdel-Rahman E., Choura S., and El-Borgi S., "Dynamics and Global Stability of Beam-Based Electrostatic Microactuators", *Journal of Vibration and Control*, Vol. 1, pp. 1-28, 2010.

[70] De Pasquale G., Veijola T., and Somà A., "Modelling and validation of air damping in perforated gold and silicon MEMS plates", *Journal of Micromechanics and Microengineering*, Vol. 20, pp. 1-12, 2010.

[71] Khater M., Abdel-Rahman E., and Nayfeh A., "A Mass Sensing Technique for Eletcrostatically-Actuated MEMS", *Proceeding of the ASME 2009 International Design Engineering Technical Conferences & Computers and Information in Engineering Conference - IDETC/CIE*, California, USA, 2009.

[72] Koester D., Cowen A., Mahadevan R., and Hardy B., *PolyMUMPs Design Handbook*, Revision 8, MEMSCAP, 2002.

[73] Stewart K., "Doped Polyaniline for Gas Sensors for the Detection of Formaldehyde", MSc thesis, *University of Waterloo*, 2011.

[74] Park S., *private communication.*

[75] Micrel Inc., LM4040/4041 voltage reference data sheet, `www.micrel.com`.

[76] Morita M., Ohmi T., Hasegawa E., Kawakami M., and Ohwada M., "Growth of Native Oxide on a Silicon Surface", *Journal of Applied Physics*, Vol. 68, pp. 1272-1281, 1990.

[77] Karkkainen A., Pesonen N., Suhonen M., Oja A., Manninen A., Tisnek N., and Seppa H., "MEMS-Based AC Voltage Reference", *IEEE Transactions on Instrumentation and Measurement*, Vol. 54, pp. 595-599, 2005.

[78] Karkkainen A., Tisnek N., Manninen A., Pesonen N., Oja A., and Seppa H., "Electrical Stability of a MEMS-Based AC Reference", *Sensors and Actuators A*, Vol. 137, pp. 169-174, 2007.

[79] Nayfeh A. and Mook D., *Nonlinear Oscillations*, Wiley Interscience, New York, 1979.

[80] Thundat T., Oden P., and Warmack R., "Microcantilever Sensors", *Microscale Thermophysical Engineering*, Vol. 1, pp. 185-199, 1997.

[81] Vyasarayani C., Abdel-Rahman E., McPhee J., and Birkett S., "Modelling MEMS Resonators Past Pull-in", *Journal of Computational and Nonlinear Dynamics*, Vol. 6, pp. 031008(1-7), 2011.

Appendices

Appendix A

Sensitivity Analysis for the Static Gas sensor

In this appendix, we analyze the sensitivity of the static binary sensor. We linearize Eqs. (3.12) in terms of A and B and perturb the equations around the static equilibrium values of A and B to obtain a matrix equation in the form

$$\begin{bmatrix} C_{11} & C_{12} \\ C_{21} & C_{22} \end{bmatrix} \begin{bmatrix} \delta A \\ \delta B \end{bmatrix} = \begin{bmatrix} L_c \\ -1 \end{bmatrix} \delta M_p \tag{A.1}$$

where the elements of the linear system matrix $[C]$ are given by

$$\begin{aligned} C_{11} =& 23040AB^2\alpha V_{\mathrm{DC}}^2 \mathrm{L_c}^6 + 23040\mathrm{AB}^2\alpha \mathrm{V}_{\mathrm{DC}}^2 \mathrm{L_c}^5 + \frac{4608}{5}\mathrm{B}^2\alpha \mathrm{V}_{\mathrm{DC}}^2 \mathrm{L_c}^5 \\ &+ \frac{13824}{5}AB\alpha V_{\mathrm{DC}}^2 \mathrm{L_c}^5 + 8880\mathrm{AB}^2\alpha \mathrm{V}_{\mathrm{DC}}^2 \mathrm{L_c}^4 + 768\mathrm{B}^2\alpha \mathrm{V}_{\mathrm{DC}}^2 \mathrm{L_c}^4 \\ &+ 216A\alpha V_{\mathrm{DC}}^2 \mathrm{L_c}^4 + 2016\mathrm{AB}\alpha \mathrm{V}_{\mathrm{DC}}^2 \mathrm{L_c}^4 + 144\mathrm{B}\alpha \mathrm{V}_{\mathrm{DC}}^2 \mathrm{L_c}^4 \\ &+ 1600AB^2\alpha V_{\mathrm{DC}}^2 \mathrm{L_c}^3 + 224\mathrm{B}^2\alpha \mathrm{V}_{\mathrm{DC}}^2 \mathrm{L_c}^3 + 96\mathrm{A}\alpha \mathrm{V}_{\mathrm{DC}}^2 \mathrm{L_c}^3 \\ &+ 512AB\alpha V_{\mathrm{DC}}^2 \mathrm{L_c}^3 + 80\mathrm{B}\alpha \mathrm{V}_{\mathrm{DC}}^2 \mathrm{L_c}^3 + 16\alpha \mathrm{V}_{\mathrm{DC}}^2 \mathrm{L_c}^3 \\ &+ 120AB^2\alpha V_{\mathrm{DC}}^2 \mathrm{L_c}^2 + 24\mathrm{B}^2\alpha \mathrm{V}_{\mathrm{DC}}^2 \mathrm{L_c}^2 + 12\mathrm{A}\alpha \mathrm{V}_{\mathrm{DC}}^2 \mathrm{L_c}^2 \\ &+ 48AB\alpha V_{\mathrm{DC}}^2 \mathrm{L_c}^2 + 12\mathrm{B}\alpha \mathrm{V}_{\mathrm{DC}}^2 \mathrm{L_c}^2 + 4\alpha \mathrm{V}_{\mathrm{DC}}^2 \mathrm{L_c}^2 - 6 \end{aligned} \tag{A.2}$$

$$
\begin{aligned}
C_{12} =& 23040A^2B\alpha V_{\mathrm{DC}}^2 \mathrm{L_c}^6 + \frac{6912}{5}\mathrm{A}^2\alpha\mathrm{V}_{\mathrm{DC}}^2\mathrm{L_c}^5 + 23040\mathrm{A}^2\mathrm{B}\alpha\mathrm{V}_{\mathrm{DC}}^2\mathrm{L_c}^5 \\
&+ \frac{9216}{5}AB\alpha V_{\mathrm{DC}}^2\mathrm{L_c}^5 + 1008\mathrm{A}^2\alpha\mathrm{V}_{\mathrm{DC}}^2\mathrm{L_c}^4 + 144\mathrm{A}\alpha\mathrm{V}_{\mathrm{DC}}^2\mathrm{L_c}^4 \\
&+ 8880A^2B\alpha V_{\mathrm{DC}}^2\mathrm{L_c}^4 + 1536\mathrm{AB}\alpha\mathrm{V}_{\mathrm{DC}}^2\mathrm{L_c}^4 + 96\mathrm{B}\alpha\mathrm{V}_{\mathrm{DC}}^2\mathrm{L_c}^4 \\
&+ 256A^2\alpha V_{\mathrm{DC}}^2\mathrm{L_c}^3 + 80\mathrm{A}\alpha\mathrm{V}_{\mathrm{DC}}^2\mathrm{L_c}^3 + 1600\mathrm{A}^2\mathrm{B}\alpha\mathrm{V}_{\mathrm{DC}}^2\mathrm{L_c}^3 \\
&+ 448AB\alpha V_{\mathrm{DC}}^2\mathrm{L_c}^3 + 64\mathrm{B}\alpha\mathrm{V}_{\mathrm{DC}}^2\mathrm{L_c}^3 + \frac{32}{3}\alpha\mathrm{V}_{\mathrm{DC}}^2\mathrm{L_c}^3 \\
&+ 24A^2\alpha V_{\mathrm{DC}}^2\mathrm{L_c}^2 + 12\mathrm{A}\alpha\mathrm{V}_{\mathrm{DC}}^2\mathrm{L_c}^2 + 120\mathrm{A}^2\mathrm{B}\alpha\mathrm{V}_{\mathrm{DC}}^2\mathrm{L_c}^2 \\
&+ 48AB\alpha V_{\mathrm{DC}}^2\mathrm{L_c}^2 + 12\mathrm{B}\alpha\mathrm{V}_{\mathrm{DC}}^2\mathrm{L_c}^2 + 4\alpha\mathrm{V}_{\mathrm{DC}}^2\mathrm{L_c}^2 - 2
\end{aligned} \tag{A.3}
$$

$$
\begin{aligned}
C_{21} =& -13824AB^2\alpha V_{\mathrm{DC}}^2\mathrm{L_c}^5 - 14400\mathrm{AB}^2\alpha\mathrm{V}_{\mathrm{DC}}^2\mathrm{L_c}^4 - 576\mathrm{B}^2\alpha\mathrm{V}_{\mathrm{DC}}^2\mathrm{L_c}^4 \\
&- 1728AB\alpha V_{\mathrm{DC}}^2\mathrm{L_c}^4 - 5920\mathrm{AB}^2\alpha\mathrm{V}_{\mathrm{DC}}^2\mathrm{L_c}^3 - 512\mathrm{B}^2\alpha\mathrm{V}_{\mathrm{DC}}^2\mathrm{L_c}^3 \\
&- 144A\alpha V_{\mathrm{DC}}^2\mathrm{L_c}^3 - 1344\mathrm{AB}\alpha\mathrm{V}_{\mathrm{DC}}^2\mathrm{L_c}^3 - 96\mathrm{B}\alpha\mathrm{V}_{\mathrm{DC}}^2\mathrm{L_c}^3 \\
&- 1200AB^2\alpha V_{\mathrm{DC}}^2\mathrm{L_c}^2 - 168\mathrm{B}^2\alpha\mathrm{V}_{\mathrm{DC}}^2\mathrm{L_c}^2 - 72\mathrm{A}\alpha\mathrm{V}_{\mathrm{DC}}^2\mathrm{L_c}^2 \\
&- 384AB\alpha V_{\mathrm{DC}}^2\mathrm{L_c}^2 - 60\mathrm{B}\alpha\mathrm{V}_{\mathrm{DC}}^2\mathrm{L_c}^2 - 12\alpha\mathrm{V}_{\mathrm{DC}}^2\mathrm{L_c}^2 \\
&- 120AB^2\alpha V_{\mathrm{DC}}^2\mathrm{L_c} - 24\mathrm{B}^2\alpha\mathrm{V}_{\mathrm{DC}}^2\mathrm{L_c} - 12\mathrm{A}\alpha\mathrm{V}_{\mathrm{DC}}^2\mathrm{L_c} \\
&- 48AB\alpha V_{\mathrm{DC}}^2\mathrm{L_c} - 12\mathrm{B}\alpha\mathrm{V}_{\mathrm{DC}}^2\mathrm{L_c} - 4\alpha\mathrm{V}_{\mathrm{DC}}^2\mathrm{L_c} - 6
\end{aligned} \tag{A.4}
$$

$$
\begin{aligned}
C_{22} =& -13824A^2B\alpha V_{\mathrm{DC}}^2\mathrm{L_c}^5 - 864\mathrm{A}^2\alpha\mathrm{V}_{\mathrm{DC}}^2\mathrm{L_c}^4 - 14400\mathrm{A}^2\mathrm{B}\alpha\mathrm{V}_{\mathrm{DC}}^2\mathrm{L_c}^4 \\
&- 1152AB\alpha V_{\mathrm{DC}}^2\mathrm{L_c}^4 - 672\mathrm{A}^2\alpha\mathrm{V}_{\mathrm{DC}}^2\mathrm{L_c}^3 - 96\mathrm{A}\alpha\mathrm{V}_{\mathrm{DC}}^2\mathrm{L_c}^3 \\
&- 5920A^2B\alpha V_{\mathrm{DC}}^2\mathrm{L_c}^3 - 1024\mathrm{AB}\alpha\mathrm{V}_{\mathrm{DC}}^2\mathrm{L_c}^3 - 64\mathrm{B}\alpha\mathrm{V}_{\mathrm{DC}}^2\mathrm{L_c}^3 \\
&- 192A^2\alpha V_{\mathrm{DC}}^2\mathrm{L_c}^2 - 60\mathrm{A}\alpha\mathrm{V}_{\mathrm{DC}}^2\mathrm{L_c}^2 - 1200\mathrm{A}^2\mathrm{B}\alpha\mathrm{V}_{\mathrm{DC}}^2\mathrm{L_c}^2 \\
&- 336AB\alpha V_{\mathrm{DC}}^2\mathrm{L_c}^2 - 48\mathrm{B}\alpha\mathrm{V}_{\mathrm{DC}}^2\mathrm{L_c}^2 - 8\alpha\mathrm{V}_{\mathrm{DC}}^2\mathrm{L_c}^2 \\
&- 24A^2\alpha V_{\mathrm{DC}}^2\mathrm{L_c} - 12\mathrm{A}\alpha\mathrm{V}_{\mathrm{DC}}^2\mathrm{L_c} - 120\mathrm{A}^2\mathrm{B}\alpha\mathrm{V}_{\mathrm{DC}}^2\mathrm{L_c} \\
&- 48AB\alpha V_{\mathrm{DC}}^2\mathrm{L_c} - 12\mathrm{B}\alpha\mathrm{V}_{\mathrm{DC}}^2\mathrm{L_c} - 4\alpha\mathrm{V}_{\mathrm{DC}}^2\mathrm{L_c}
\end{aligned} \tag{A.5}
$$

The solution of Eq. (A.1) can be written in the form

$$\begin{bmatrix} \delta A \\ \delta B \end{bmatrix} = \frac{C^{\text{adj}}}{|C|} \begin{bmatrix} L_c \\ -1 \end{bmatrix} \delta M_p \tag{A.6}$$

We note that for sensor geometries of interest in this work, L_c is of order $O(10^{-1})$, A and B are of order $O(10^{-2})$, and αV_{DC}^2 is of order $O(1)$. We consider terms of order higher than $O(10^{-2})$ negligible and write the determinant of the system matrix $|C|$ as

$$\begin{aligned} |C| = &- 12 + 16\alpha V_{\text{DC}}^2 \text{L}_\text{c} + 48\alpha \text{V}_\text{DC}^2 \text{L}_\text{c}(\text{L}_\text{c} + \text{A} + \text{B}) \\ &+ 16\alpha V_{\text{DC}}^2 {\text{L}_\text{c}}^2 (4\text{L}_\text{c} + 15\text{A} + 240\text{B}) \end{aligned} \tag{A.7}$$

and the matrix of cofactors C^{adj} as

$$C^{\text{adj}} = \begin{bmatrix} C_{11}^{\text{adj}} & C_{12}^{\text{adj}} \\ C_{21}^{\text{adj}} & C_{22}^{\text{adj}} \end{bmatrix} \tag{A.8}$$

where

$$C_{11}^{\text{adj}} = -8\alpha V_{\text{DC}}^2 {\text{L}_\text{c}}^2 - 12\text{A}\alpha \text{V}_\text{DC}^2 \text{L}_\text{c} - 12\text{B}\alpha \text{V}_\text{DC}^2 \text{L}_\text{c} - 4\alpha \text{V}_\text{DC}^2 \text{L}_\text{c} \tag{A.9}$$

$$C_{12}^{\text{adj}} = 2 - 4\alpha V_{\text{DC}}^2 {\text{L}_\text{c}}^2 \tag{A.10}$$

$$C_{21}^{\text{adj}} = 12\alpha V_{\text{DC}}^2 {\text{L}_\text{c}}^2 + 12\text{A}\alpha \text{V}_\text{DC}^2 \text{L}_\text{c} + 12\text{B}\alpha \text{V}_\text{DC}^2 \text{L}_\text{c} + 4\alpha \text{V}_\text{DC}^2 \text{L}_\text{c} + 6 \tag{A.11}$$

$$C_{22}^{\text{adj}} = -6 + 4\alpha V_{\text{DC}}^2 {\text{L}_\text{c}}^2 \tag{A.12}$$

Therefore, the sensitivity terms in Eq. (3.17) can be written as:

$$\frac{\delta A}{\delta M_p} = \frac{-2 - 12A\alpha V_{\text{DC}}^2 {\text{L}_\text{c}}^2 - 12\text{B}\alpha \text{V}_\text{DC}^2 {\text{L}_\text{c}}^2}{|C|} \tag{A.13}$$

$$\frac{\delta B}{\delta M_p} = \frac{12 + 12A\alpha V_{\text{DC}}^2 \text{L}_\text{c} + 12\text{B}\alpha \text{V}_\text{DC}^2 \text{L}_\text{c}}{|C|} \tag{A.14}$$

where terms of order higher than $O(10^{-2})$ have been neglected.

Appendix B

Sensitivity Analysis for the Dynamic Gas Sensor

In this appendix, we analyze the sensitivity of the dynamic binary sensor. We expand in Taylor series the electrostatic force terms in the one-mode equation of motion Eq. (3.23) and retain terms up to order three in q to obtain

$$
\begin{aligned}
&2\,\ddot{q} + 8.82M\,\ddot{q} + 27.4ML_c\,\ddot{q} + 28.5ML_c^2\ddot{q} + \frac{0.999}{Q}\,\dot{q} \\
&+ 26.3q - 0.405\alpha\left(285.88L_c^3 + 271.5L_c^2 + 85.92L_c\right)\left(V_{\rm AC} + V_{\rm DC}\right)^2\, q \\
&- 0.45\alpha\left(1883.3L_c^4 + 2384.3L_c^3 + 1131.95L_c^2 + 238.85L_c\right)\left(V_{\rm AC} + V_{\rm DC}\right)^2\, q^2 \\
&- 0.48\alpha\left(12406.1L_c^5 + 19633.2L_c^4 + 12428.1L_c^3 + 3933.58L_c^2 + 622.5L_c\right) \\
&\times \left(V_{\rm AC} + V_{\rm DC}\right)^2\, q^3 = 0.3\,\alpha\,\left(43.4L_c^2 + 27.47L_c\right)\left(V_{\rm AC} + V_{\rm DC}\right)^2
\end{aligned}
\tag{B.1}
$$

where Q is the quality factor. Ordering q at $O(\epsilon)$, L_c at $O(\epsilon)$, α at $O(\epsilon^2)$, $V_{\rm DC}$ at $O(1/\epsilon)$, and $V_{\rm AC}$ at $O(\epsilon)$ and retaining terms up to order $O(\epsilon^4)$, we obtain a

consistently expanded equation of motion in the form

$$\begin{aligned}
&2\,\ddot{q} + 8.82M\,\ddot{q} + 27.4ML_c\,\ddot{q} + 28.5ML_c^2\ddot{q} + \frac{0.999}{Q}\,\dot{q} + 26.3\,q \\
&- 115.7\alpha L_c^3 V_{\mathrm{DC}}^2\,q - 109.9\alpha L_c^2 V_{\mathrm{DC}}^2\,q - 34.8\alpha L_c V_{\mathrm{DC}}^2\,q - 69.6\alpha L_c V_{\mathrm{DC}} V_{\mathrm{AC}}\,q \\
&- 515.5\alpha L_c^2 V_{\mathrm{DC}}^2\,q^2 - 108.77\alpha L_c V_{\mathrm{DC}}^2\,q^2 - 302.388\alpha L_c V_{\mathrm{DC}}^2\,q^3 \\
&= 13.2\alpha L_c^2 V_{\mathrm{DC}}^2 + 8.34\alpha L_c V_{\mathrm{DC}}^2 + 26.4\alpha L_c^2 V_{\mathrm{DC}} V_{\mathrm{AC}} + 16.7\alpha L_c V_{\mathrm{DC}} V_{\mathrm{AC}}
\end{aligned} \tag{B.2}$$

where ϵ is a small bookkeeping parameter. We re-write the modal coordinate $q(t)$ as the summation of a static component q_s due to the DC force and a dynamic component $q_d(t)$ due to AC forcing

$$q(t) = q_s + q_d(t) \tag{B.3}$$

Under a DC force, Eq. (B.2) reduces to

$$\begin{aligned}
&26.3\,q_s - 115.7\alpha V_{\mathrm{DC}}^2 L_c^3\,q_s - 109.88\alpha V_{\mathrm{DC}}^2 L_c^2\,q_s - 34.7786\alpha V_{\mathrm{DC}}^2 L_c\,q_s \\
&- 108.77\alpha L_c\,q_s^2 - 515.5 L_c^2\alpha V_{\mathrm{DC}}^2\,q_s^2 - 302.4\alpha L_c V_{\mathrm{DC}}^2\,q_s^3 \\
&= 13.1752\alpha L_c^2\,V_{\mathrm{DC}}^2 + 8.34 L_c\alpha V_{\mathrm{DC}}^2
\end{aligned} \tag{B.4}$$

Substituting for q with Eq. (B.3) and using Eq. (B.4) in Eq. (B.2), to eliminate the static deflection q_s terms, we obtain an equation representing the motion of the sense-plate around the equilibrium position q_s in the form

$$M_e\,\ddot{q}_d + C\,\dot{q}_d - k_1\,q_d - k_2\,q_d^2 - k_3\,q_d^3 = \lambda\,V_{\mathrm{AC}} \tag{B.5}$$

where

$$M_e = 8.82M + 27.4ML_c + 28.5ML_c^2 + 2 \tag{B.6}$$

$$C = \frac{0.999}{Q} \tag{B.7}$$

$$\begin{aligned} k_1 = & -26.3 + 34.8\alpha V_{\mathrm{DC}}^2 L_c + 115.7\alpha V_{\mathrm{DC}}^2 L_c^3 + 109.9\alpha V_{\mathrm{DC}}^2 L_c^2 + 1030.98\alpha q_s V_{\mathrm{DC}}^2 L_c^2 \\ & + 907.16\alpha q_s^2 V_{\mathrm{DC}}^2 L_c + 217.54\alpha q_s V_{\mathrm{DC}}^2 L_c + 69.56\alpha V_{\mathrm{DC}} V_{\mathrm{AC}} L_c \end{aligned} \tag{B.8}$$

$$k_2 = 108.77\alpha L_c V_{\mathrm{DC}}^2 + 515.5\alpha L_c^2 V_{\mathrm{DC}}^2 + 907.2\alpha L_c q_s V_{\mathrm{DC}}^2 \tag{B.9}$$

$$k_3 = 302.4\alpha L_c V_{\mathrm{DC}}^2 \tag{B.10}$$

$$\lambda = 16.68\alpha V_{\mathrm{DC}} L_c + 26.35\alpha V_{\mathrm{DC}} L_c^2 + 69.5572\alpha q_s V_{\mathrm{DC}} L_c \tag{B.11}$$

We note that for a sensor with geometric specification similar to our class of sensors, the first term in each of these expressions is the dominant term of the expression.